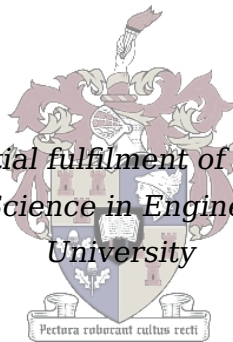


# **Stall Prevention Control of Fixed-Wing Unmanned Aerial Vehicles**

by

Matthys Michaelse Basson

*Thesis presented in partial fulfilment of the requirements for the  
degree of Master of Science in Engineering at Stellenbosch  
University*



Supervisor: Dr. Iain K. Peddle  
Department of Electrical & Electronic Engineering

March 2010

# Declaration

By submitting this thesis electronically, I declare that the entirety of the work contained therein is my own, original work, that I am the owner of the copyright thereof (unless to the extent explicitly otherwise stated) and that I have not previously in its entirety or in part submitted it for obtaining any qualification.

March 2010

Copyright © 2010 Stellenbosch University  
All rights reserved.

# Abstract

This thesis presents the development of a stall prevention flight control subsystem, which can easily be integrated into existing flight control architectures of fixed-wing unmanned aerial vehicles (UAV's). This research forms an important part of fault-tolerant flight control systems and will ensure that the aircraft continues to operate safely within its linear aerodynamic region.

The focus of this thesis was the stall detection and prevention problem. After a thorough literature study on the topic of stall, a model based stall prevention control algorithm with feedback from an angle of attack sensor was developed. This algorithm takes into account the slew rate and saturation limits of the aircraft's servos and is able to predict when the current flight condition will result in stall. The primary concern was stall during wings-level flight and involved the prevention of stall by utilising only the elevator control surface. A model predictive slew rate control algorithm was developed to override and dynamically limit the elevator command to ensure that the angle of attack does not exceed a predefined limit. The stall prevention control system was designed to operate as a switching control scheme, to minimise any restrictions imposed on the existing flight control system.

Finally, software in the loop simulations were conducted using a nonlinear aircraft model and realistic sensor noise, to verify the theoretical results obtained during the development of this stall prevention control strategy. A worst-case performance analysis was also conducted to investigate the robustness of the control algorithms against model uncertainties.

# Uittreksel

Hierdie tesis handel oor die ontwikkeling van 'n staak voorkomings-vlugbeheer sub-stelsel wat maklik geïntegreer kan word in bestaande vlugbeheer argitektuur van onbemande vaste-vlerk lugvaartuie. Hierdie tesis vorm 'n belangrike deel van fout-tolerante vlugbeheertegniese en sal verseker dat die vliegtuig slegs binne sy lineêre aerodinamiese werksgebied bly.

Die fokus van hierdie tesis is die staak opsporing en voorkomings probleem. Na afloop van 'n deeglike literatuurstudie oor die onderwerp van staak, is 'n model gebaseerde staak voorkomings-beheertegniese ontwikkel, wat terugvoer van 'n invalshoek sensor ontvang. Hierdie algoritme neem die sleur tempo en defleksie limiete van die vliegtuig se servos in ag en is in staat om staak te voorspel. Die primêre oorweging was staak tydens simmetriese vlugte en behels slegs die voorkoming van staak deur gebruik te maak van die heil beheer oppervlak. 'n Model voorspellings sleur tempo beheeralgoritme is ontwikkel om die heil-roer dinamies te beperk sodat die invalshoek nie 'n sekere vooraf bepaalde limiet oorskry nie. Die staak voorkomings beheerstelsel is ontwerp om te funksioneer as 'n skakel beheer skema om die beperkings op die bestaande vlugbeheerstelsel te minimaliseer.

Laastens was sagteware-in-die-lus simulasies gebruik om die teoretiese resultate, wat verkry is tydens die ontwikkeling van hierdie staak voorkomings beheer-strategie, te kontroleer. Om die robuustheid van hierdie beheeralgoritmes teen model onsekerhede te ondersoek, is 'n ergste-geval prestasie analise ook uitgevoer.

# Acknowledgements

I would like to extend my most sincere gratitude to the following people/organisations for their contribution towards this thesis,

- Dr. I.K. Peddle, for all your guidance, advice and support through the course of this project. Thank you for providing me with a deeper understanding of aircraft dynamics and control, your knowledge and insight is inspiring.
- Prof. T. Jones and Mr. J.A.A. Engelbrecht, for your valued input during our research meetings. Your experience and insight in the field of unmanned aerial vehicles are invaluable.
- The National Aerospace Centre of Excellence (NACoE), for their financial support and making this research possible.
- My lovely fiancé, Ancolline Wright, your endless unconditional love have carried me throughout this project. Thank you for your support and understanding.
- My family, for your love and understanding throughout this project. You provided me with the necessary environment and support network to reach my full potential. You allowed me to achieve all that I have today!
- AM de Jager and Chris Jaquet, for your friendship, helpful advice and ideas throughout this project. Your technical assistance during the write-up of this thesis is much appreciated.
- Wihan Pieterse and Simon Pauck, for the much needed lunch-time gaming distractions. I highly value your friendship, thank you for making the time in the lab enjoyable!
- Reinhart Fourie, for your invaluable friendship and support throughout this project.
- And all my friends in the Electronic Systems Lab, especially Raun de Hart, Rudi Gaum and Deon Blaauw for your valued inputs, advice and always being there to share ideas.

*I dedicate this thesis to my parents  
and my lovely wife to be.*

---

M.M. Basson

# Contents

|   |              |
|---|--------------|
| <b>Declaration</b>                                    | <b>i</b>     |
| <b>Abstract</b>                                       | <b>ii</b>    |
| <b>Uittreksel</b>                                     | <b>iii</b>   |
| <b>Acknowledgements</b>                               | <b>iv</b>    |
| <b>Contents</b>                                       | <b>vi</b>    |
| <b>Nomenclature</b>                                   | <b>x</b>     |
| <b>List of Figures</b>                                | <b>xiv</b>   |
| <b>List of Tables</b>                                 | <b>xviii</b> |
| <b>1 Introduction</b>                                 | <b>1</b>     |
| 1.1 Brief History . . . . .                           | 1            |
| 1.2 Project Description . . . . .                     | 2            |
| 1.3 Structure and Overview . . . . .                  | 3            |
| <b>2 Fundamentals of Stall</b>                        | <b>5</b>     |
| 2.1 Theory of Stall . . . . .                         | 5            |
| 2.1.1 Formal Definitions . . . . .                    | 6            |
| 2.2 Geometric Definitions . . . . .                   | 7            |
| 2.2.1 Wing and Aerofoil Geometry . . . . .            | 8            |
| 2.2.2 Aerofoil Reference Centres . . . . .            | 10           |
| 2.3 Aerofoil Stall Characteristics . . . . .          | 11           |
| 2.4 Wing Planform Stall Characteristics . . . . .     | 15           |
| 2.5 Types of Stalls . . . . .                         | 16           |
| 2.5.1 Stall Speed . . . . .                           | 18           |
| 2.5.2 Load Factor . . . . .                           | 19           |
| 2.5.3 Ground Effect . . . . .                         | 21           |
| 2.6 Classical Stall Prevention and Recovery . . . . . | 22           |

|          |  |           |
|----------|--|-----------|
| 2.6.1    | Stall Warning and Safety Devices . . . . .               | 23        |
| 2.7      | Summary . . . . .  | 25        |
| <b>3</b> | <b>Mathematical Aircraft Model and Control</b>           | <b>26</b> |
| 3.1      | Axis Systems and Notation . . . . .                      | 26        |
| 3.1.1    | Earth Axes . . . . .                                     | 26        |
| 3.1.2    | Aircraft Axes . . . . .                                  | 27        |
| 3.1.3    | Aircraft Actuation . . . . .                             | 28        |
| 3.2      | Numerical Aerodynamic Analysis . . . . .                 | 29        |
| 3.2.1    | Simulation Results from Analysis . . . . .               | 29        |
| 3.3      | Aircraft Model . . . . .                                 | 30        |
| 3.3.1    | Longitudinal Dynamics . . . . .                          | 31        |
| 3.4      | Aircraft Automatic Flight Control System . . . . .       | 34        |
| 3.4.1    | Linear Decoupled Longitudinal Dynamics . . . . .         | 34        |
| 3.4.2    | Normal Specific Acceleration Controller . . . . .        | 36        |
| 3.5      | Stall Prevention Control Augmentation Strategy . . . . . | 38        |
| 3.5.1    | Angle of Attack State Saturation . . . . .               | 38        |
| 3.5.2    | Switching Strategy . . . . .                             | 39        |
| 3.5.3    | Stall Prevention Control . . . . .                       | 40        |
| 3.6      | Summary . . . . .  | 42        |
| <b>4</b> | <b>Preliminary Methodology</b>                           | <b>43</b> |
| 4.1      | Conceptual Phase Plane Approach . . . . .                | 43        |
| 4.1.1    | Phase Plane State Trajectories . . . . .                 | 45        |
| 4.1.2    | Description of Stall Prevention Control . . . . .        | 46        |
| 4.2      | Forward State Propagation . . . . .                      | 47        |
| 4.2.1    | State Transition Equation . . . . .                      | 47        |
| 4.3      | Zero Input Response . . . . .                            | 49        |
| 4.3.1    | State Transition Matrix . . . . .                        | 50        |
| 4.3.2    | Zero Input State Trajectory . . . . .                    | 52        |
| 4.3.3    | Stall Detection Envelope . . . . .                       | 55        |
| 4.4      | Summary . . . . .  | 57        |
| <b>5</b> | <b>Stall Prevention Control</b>                          | <b>58</b> |
| 5.1      | Active Stall Prevention . . . . .                        | 58        |
| 5.1.1    | Stall Prevention State Trajectory . . . . .              | 59        |
| 5.2      | Zero State Response . . . . .                            | 60        |
| 5.2.1    | Velocity Step Component . . . . .                        | 62        |
| 5.2.2    | Constant Step Component . . . . .                        | 64        |
| 5.3      | Complete State Transition Equation . . . . .             | 66        |
| 5.3.1    | Stall Prevention State Trajectory . . . . .              | 67        |



|          |   |            |
|----------|---|------------|
| 5.4      | AoA Peak Prediction . . . . .   | 70         |
| 5.4.1    | Peak angle of attack as a result of the velocity step input . . . . . | 71         |
| 5.4.2    | Peak angle of attack as a result of the constant step input . . . . . | 73         |
| 5.4.3    | Linear Verification . . . . .   | 75         |
| 5.5      | Recursive Model Predictive Slew Rate Control . . . . .                | 77         |
| 5.5.1    | Modified False Position Method . . . . .                              | 78         |
| 5.5.2    | Algorithm Verification . . . . .                                      | 80         |
| 5.6      | Summary . . . . .   | 82         |
| <b>6</b> | <b>Angle of Attack Regulating Control</b>                             | <b>83</b>  |
| 6.1      | Stall Prevention Control Strategy Description . . . . .               | 83         |
| 6.1.1    | Finite State Machine . . . . .  | 84         |
| 6.2      | AoA Reference Tracking Controller . . . . .                           | 85         |
| 6.2.1    | Controller Design . . . . .   | 86         |
| 6.2.2    | Linear Closed Loop Analysis and Pole Placement . . . . .              | 91         |
| 6.2.3    | System Delays and Anti-Windup . . . . .                               | 93         |
| 6.3      | Summary . . . . .   | 95         |
| <b>7</b> | <b>Simulation and Analysis</b>  | <b>96</b>  |
| 7.1      | Linear Simulation . . . . .   | 96         |
| 7.2      | Nonlinear SIL Simulation . . . . .                                    | 98         |
| 7.2.1    | Slow Speed Flight . . . . .   | 99         |
| 7.2.2    | Steep Pull-up . . . . .   | 101        |
| 7.2.3    | Reactivating the NSA Control System . . . . .                         | 102        |
| 7.3      | Sensitivity Analysis . . . . .  | 104        |
| 7.3.1    | Investigating Parameter Uncertainty . . . . .                         | 104        |
| 7.3.2    | Level of Uncertainty . . . . .  | 105        |
| 7.4      | Worst-Case Performance Simulation . . . . .                           | 106        |
| 7.4.1    | Detection Algorithm . . . . .   | 106        |
| 7.4.2    | Stall Prevention Control System . . . . .                             | 110        |
| 7.5      | Summary . . . . .   | 113        |
| <b>8</b> | <b>Conclusions and Recommendations</b>                                | <b>114</b> |
| 8.1      | Summary . . . . .   | 114        |
| 8.1.1    | Computational Efficiency . . . . .                                    | 116        |
| 8.1.2    | Contributions . . . . .   | 116        |
| 8.2      | Recommendations . . . . .   | 117        |
| 8.2.1    | Further Research . . . . .  | 117        |
|          | <b>List of References</b>   | <b>119</b> |
|          | <b>Appendices</b>   | <b>121</b> |

|          |  |            |
|----------|--|------------|
| <b>A</b> | <b>Mathematical Derivations</b>                            | <b>122</b> |
| A.1      | Aircraft Trim Condition . . . . .                          | 122        |
| A.2      | Longitudinal Stability Characteristics . . . . .           | 123        |
| A.2.1    | Vertical speed stability . . . . .                         | 123        |
| A.2.2    | Angle of attack stability . . . . .                        | 124        |
| A.3      | Static Contribution . . . . .                              | 126        |
| A.4      | Variation of Elevator Trim Angle with Velocity . . . . .   | 129        |
| A.5      | Elevator Effectiveness . . . . .                           | 130        |
| <b>B</b> | <b>Aircraft Data</b>                                       | <b>134</b> |
| B.1      | Geometric, Inertial and Propulsion Properties . . . . .    | 134        |
| B.2      | Trim Condition . . . . .                                   | 135        |
| B.3      | Aerodynamic Modelling . . . . .                            | 135        |
| B.3.1    | Analysis with AVL . . . . .                                | 136        |
| B.4      | Numeric Aerodynamic Investigation . . . . .                | 137        |
| B.4.1    | XFOIL . . . . .  | 138        |
| B.4.2    | XFLR5 . . . . .  | 140        |
| B.5      | Typical AoA Sensors for Practical Implementation . . . . . | 143        |
| B.5.1    | Fixed Differential Pressure Probes . . . . .               | 143        |
| B.5.2    | Pivoted Vane Sensors . . . . .                             | 144        |
| B.5.3    | Null-Seeking Differential Pressure Probes . . . . .        | 145        |

# Nomenclature

## Subscripts and Superscripts

$W, B, I, R$  Denote the wind, body, inertial and reference axis systems respectively.

$ZI, ZS$  Denote the zero input and zero state components of the state transition equation respectively.

## Vectors and Tensors

$A, V, P$  Acceleration, velocity and position vectors.

$F, M$  Force and moment vectors.

$G, I_B$  Gravitational vector and moment of inertia matrix.

## Coordinate Vector

$V_C^{AB}$  Recurring vector notation. Denotes vector  $V$  with data about axis system  $A$  relative to axis system  $B$ , coordinated in axis system  $C$ .

$A, B, C$  Axial, lateral and normal specific acceleration vector coordinates in the subscript axis system. If the subscript is omitted, body axes is implied.

$X, Y, Z$  Axial, lateral and normal force coordinates in the subscript axis system. If the subscript is omitted, body axes is implied.

|                          |   |
|--------------------------|---|
| $L, M, N$                | Roll, pitch and yaw moment coordinates in the subscript axis system. If the subscript is omitted, body axes is implied.                             |
| $P, Q, R$                | Roll, pitch and yaw rate of the subscript axis system with respect to inertial space. If the subscript is omitted, body axes is implied.            |
| $I_{xx}, I_{yy}, I_{zz}$ | Principle moments of inertia about the X, Y and Z axes.   |
| $\bar{V}, \alpha, \beta$ | Velocity magnitude, angle of attack and angle of sideslip.  |
| $e_{(\cdot)}^{(\cdot)}$  | DCM parameter. The subscript indicates its position in the DCM while the superscript indicates the axis systems involved in the DCM transformation. |

### Modelling

|                                |  |
|--------------------------------|--|
| $\bar{V}_a, \rho, q$           | Air speed magnitude, air density and dynamic pressure.                                       |
| $S, \bar{c}, b$                | Wing area, mean aerodynamic chord and wingspan.  |
| $\mathcal{R}, e$               | Aspect ratio and Oswald efficiency factor.   |
| $L, D$                         | Lift and drag force.   |
| $\delta_A, \delta_E, \delta_R$ | Aileron, elevator and rudder control deflection.   |
| $T, T_c, \tau_T$               | Actual thrust variable, thrust command variable and throttle lag time constant respectively. |
| $g, m, I_{(\cdot)}$            | Gravitational force per unit mass, mass and moment of inertia parameter.                     |

### Aerodynamic Coefficients

|                             |   |
|-----------------------------|---|
| $C_{D_0}, C_{L_0}, C_{m_0}$ | Parasitic drag, static lift and static pitch moment coefficients. |
| $C_L, C_D, C_y$             | Aerodynamics lift, drag and side force coefficients.              |
| $C_l, C_m, C_n$             | Aerodynamics roll, pitch and yaw moment coefficients.             |

**Control**

|                             |  |
|-----------------------------|--|
| $t, s$                      | Time and Laplace variable respectively.  |
| $p, z$                      | Poles and zeros.   |
| $\omega_n, \omega_d, \zeta$ | Natural frequency, undamped natural frequency and damping ratio.   |
| $\mathbf{x}, u$             | State vector and input scalar.   |
| <b>A, B, C</b>              | System, input and output continuous time matrices respectively.  |
| $a_{jk}$                    | Recurring matrix notation. Denotes a element in matrix <b>A</b> , with $j$ the row and $k$ the column index value. |
| $K_{(\cdot)}, \bar{N}$      | Feedback and feedforward gain.   |
| $\mu, \dot{\delta}_{sr}$    | Slew rate variable and maximum slew rate limit.  |

**Acronyms**

|      |  |
|------|--|
| 2D   | Two Dimensional                                |
| 3D   | Three Dimensional                              |
| AoA  | Angle of Attack                                |
| AC   | Aerodynamic Centre                             |
| AVL  | Athena Vortex Lattice                          |
| CG   | Centre of Gravity                              |
| CP   | Centre of Pressure                             |
| CSIR | Council for Scientific and Industrial Research |
| DCM  | Direction Cosine Matrix                        |

|      |                                 |
|------|---------------------------------|
| DA   | Detection Algorithm             |
| HIL  | Hardware-in-the-loop            |
| LHP  | Left Half Plane                 |
| LTI  | Linear Time Invariant           |
| MP   | Minimum Phase                   |
| NMP  | Non-Minimum Phase               |
| NSA  | Normal Specific Acceleration    |
| NP   | Neutral Point                   |
| ODE  | Ordinary Differential Equation  |
| RHP  | Right Half Plane                |
| RPV  | Remotely Piloted Vehicles       |
| SDP  | Stall Detection Principle       |
| SIL  | Software-in-the-loop            |
| SISO | Single-Input-Single-Output      |
| SPC  | Stall Prevention Control System |
| SRC  | Slew Rate Control System        |
| SU   | Stellenbosch University         |
| UAS  | Unmanned Air Systems            |
| UAV  | Unmanned Aerial Vehicle         |

# List of Figures

|      |  |    |
|------|--|----|
| 1.1  | The Modular UAV research demonstrator  | 2  |
| 1.2  | Thesis outline   | 4  |
| 2.1  | Typical Lift and Drag polars for a subsonic aircraft   | 6  |
| 2.2  | Geometric properties of a typical subsonic wing  | 8  |
| 2.3  | Effect of aspect ratio on the lift curve of a wing as a function of the absolute angle of attack | 9  |
| 2.4  | Geometric properties of a typical subsonic aerofoil  | 9  |
| 2.5  | The effect of camber on the lift curve of an aerofoil section                                    | 10 |
| 2.6  | Reference centres of a typical subsonic aerofoil section   | 11 |
| 2.7  | Flow around the wing's aerofoil displaying exaggerated boundary layer thickness                  | 12 |
| 2.8  | Pressure distribution over an aerofoil   | 13 |
| 2.9  | The formation of stall on an aerofoil section  | 14 |
| 2.10 | Laminar separation with turbulent re-attachment  | 15 |
| 2.11 | The effect of the wing planform on stall progression across its surface                          | 16 |
| 2.12 | The relationship between angle of attack and air velocity indicating stall speed                 | 19 |
| 2.13 | The relationship between stall speed and load factor during steep turns                          | 20 |
| 2.14 | Typical V-n diagram of an aircraft   | 20 |
| 2.15 | The effect of altitude on the drag due to lift   | 21 |
| 2.16 | Types of configuration used with aerodynamic high-lift devices                                   | 24 |
| 2.17 | The effect of slots on the lift curve of a wing  | 24 |
| 3.1  | Inertial Reference Frame   | 27 |
| 3.2  | Body axis system definition with variable notations and conventions                              | 28 |
| 3.3  | Body axes transformation to wind axes  | 28 |
| 3.4  | Polar plots for lift and drag coefficients simulated with XFLR5 on wing structure                | 29 |
| 3.5  | Six-degrees-of-freedom equations of motion aircraft model  | 30 |
| 3.6  | Autopilot control system architectural layout  | 34 |

|      |   |    |
|------|---|----|
| 3.7  | Normal specific acceleration control system architecture . . . . .  | 37 |
| 3.8  | Switching strategy for angle of attack state saturation . . . . .   | 39 |
| 3.9  | Decision block responsible for the controller switching . . . . .   | 39 |
| 3.10 | Stall prevention control blocks responsible of the elevator command signal . . . . .                        | 41 |
| 4.1  | A 2D visualisation of phase space . . . . .   | 44 |
| 4.2  | Visualisation of the flow in the phase plane . . . . .  | 44 |
| 4.3  | Visualisation of possible state trajectories in the phase plane . . . . .                                   | 45 |
| 4.4  | Visualisation of state trajectories in the phase plane under stall prevention control supervision . . . . . | 46 |
| 4.5  | Sketch of a exponentially modulated sinusiod . . . . .  | 51 |
| 4.6  | Phase plane analysis of the zero input state trajectories . . . . .   | 53 |
| 4.7  | Zero input state trajectories . . . . .   | 54 |
| 4.8  | Stall detection envelope conceptual sketch . . . . .  | 55 |
| 4.9  | Stall detection envelope for the zero input state trajectories . . . . .                                    | 56 |
| 4.10 | Effect of variation in air velocity on the stall detection envelope . . . . .                               | 57 |
| 5.1  | Graphical representation of active stall prevention elevator command . . . . .                              | 59 |
| 5.2  | Stall detection envelope sketch for the stall prevention state trajectories . . . . .                       | 59 |
| 5.3  | Stall prevention elevator input signal . . . . .  | 60 |
| 5.4  | Graphical representation of the piecewise defined stall prevention state trajectory . . . . .               | 62 |
| 5.5  | Zero state trajectory for a velocity step input signal . . . . .  | 63 |
| 5.6  | Zero state trajectory for a constant step input signal . . . . .  | 65 |
| 5.7  | Phase plane analysis of complete state trajectory . . . . .   | 68 |
| 5.8  | Stall detection envelope for the stall prevention state trajectory . . . . .                                | 69 |
| 5.9  | Effect of variation in the initial elevator angle on the stall detection envelope . . . . .                 | 69 |
| 5.10 | Detection algorithm block diagram . . . . .   | 70 |
| 5.11 | AoA state trajectory as a result of the velocity step input . . . . .                                       | 71 |
| 5.12 | Graphical presentation of the Newton Raphson approximation method . . . . .                                 | 72 |
| 5.13 | AoA state trajectory as a result of the constant step input . . . . .                                       | 74 |
| 5.14 | State trajectory calculated for the stall prevention elevator input signal at $t = 0.149 s$ . . . . .       | 75 |
| 5.15 | The elevator input command displaying the simulated recovery excitation signal . . . . .                    | 76 |
| 5.16 | The calculated AoA peak values for every state measurement . . . . .  | 77 |
| 5.17 | The Phase Portrait of the linear simulation displaying the calculated recovery trajectories . . . . .       | 78 |
| 5.18 | Graphical presentation of improvement over original false position method . . . . .                         | 80 |
| 5.19 | Simulated stall prevention state trajectory given the predefined slew rate . . . . .                        | 81 |
| 5.20 | Simulated stall prevention state trajectory given the calculated slew rate . . . . .                        | 81 |



|   |     |
|---|-----|
| 5.21 Adjustment of the stall prevention elevator signal at the current operating condition . . . . .  | 82  |
| 6.1 Stall prevention control overriding the elevator command signal . . . . .   | 84  |
| 6.2 Stall prevention control finite state machine . . . . .   | 85  |
| 6.3 Angle of attack controller for the aircraft's normal dynamics . . . . .   | 86  |
| 6.4 The poles and zeros from elevator to angle of attack for complete model . .   | 86  |
| 6.5 The poles and zeros from elevator to angle of attack for simplified model .   | 87  |
| 6.6 Closed loop angle of attack step response on both the complete and simplified normal dynamics models . . . . .  | 92  |
| 6.7 Effect of feedforward gain on the closed loop AoA step response . . . . .   | 93  |
| 6.8 Closed loop angle of attack step response displaying the effect of a system delay . . . . .   | 94  |
| 7.1 Linear simulation results . . . . .   | 97  |
| 7.2 Virtual aircraft simulation graphical output . . . . .  | 99  |
| 7.3 Nonlinear slow speed flight simulation results . . . . .  | 100 |
| 7.4 Nonlinear steep pull-up simulation results for the pitch rate . . . . .   | 101 |
| 7.5 Nonlinear steep pull-up simulation results . . . . .  | 102 |
| 7.6 Nonlinear SIL simulation result for reconnecting the NSA controller . . . .   | 103 |
| 7.7 State trajectories calculated for stall prevention elevator input signal . . .  | 107 |
| 7.8 AoA stall prevention state trajectory with worst-case parameter variation .   | 107 |
| 7.9 AoA stall prevention state trajectory peak values with worst-case parameter variation . . . . .   | 108 |
| 7.10 AoA stall prevention state trajectory peak values with $C_{L_0}$ , $C_{L_\alpha}$ , $C_{m_\alpha}$ and $C_{m_{\delta_E}}$ worst-case parameter variation . . . . . | 109 |
| 7.11 AoA stall prevention state trajectory for worst-case premature and delayed detection . . . . .   | 110 |
| 7.12 Linear worst-case performance simulation results . . . . .   | 111 |
| 7.13 Linear worst-case performance simulation results . . . . .   | 112 |
| A.1 Forces and moments acting on an aircraft during symmetric level flight . .  | 122 |
| A.2 Simple pitching moment model for a statically stable airframe configuration   | 125 |
| A.3 Effect of flight path angle on angle of attack recovery transient trajectory .  | 127 |
| A.4 Example of variation of elevator angle to trim with speed and $cg$ . . . . .  | 129 |
| A.5 Effect of elevator deflection angle on $C_m-\alpha$ and $C_L-\alpha$ curves . . . . .   | 131 |
| A.6 Control surface effectiveness parameter . . . . .   | 132 |
| A.7 Angle of attack to elevator open loop bode plot . . . . .   | 133 |
| B.1 The aerofoil and fuselage assembly of the aerial vehicle as designed in AVL   | 136 |
| B.2 Aerofoil section of main wing of aerial vehicle . . . . .   | 139 |
| B.3 Polar plots for lift and drag coefficients simulated with XFOIL . . . . .   | 139 |

B.4 The main wing of the aerial vehicle as designed in XFLR5 . . . . . 141

B.5 Polar plots for lift and drag coefficients simulated with XFLR5 on wing structure . . . . . 141

B.6 The main wing, tailplane and fin assembly of the aerial vehicle as designed in XFLR5 . . . . . 142

B.7 Polar plots for lift and drag coefficients simulated with XFLR5 on aircraft assembly . . . . . 142

B.8 Typical pressure difference based angle of attack sensor . . . . . 144

B.9 Typical vane type angle of attack and angle of sideslip sensors . . . . . 144

B.10 Typical null-seeking differential pressure probe type angle of attack sensors 145

# List of Tables

|     |  |     |
|-----|--|-----|
| 5.1 | The coefficients for the zero state transition equation given a velocity step input . . . . .                  | 67  |
| 5.2 | The coefficients for the zero state transition equation given a constant step input . . . . .                  | 67  |
| 7.1 | The accuracy of a typical AoA vane sensor . . . . .  | 98  |
| 7.2 | Certainty ratings for the estimated longitudinal stability and control derivatives . . . . .                   | 106 |
| 7.3 | Certainty ratings for the estimated longitudinal static coefficients as well as the mass and inertia . . . . . | 106 |
| 7.4 | Parameter variation combinations describing the maximum and minimum worst-case performance envelope . . . . .  | 109 |
| B.1 | The non-dimensional longitudinal stability and control derivatives . . . . .                                   | 137 |
| B.2 | The non-dimensional lateral stability and control derivatives . . . . .  | 137 |

# Chapter 1

## Introduction

In 2008, Stellenbosch University (SU) entered into a contract with the Council for Scientific and Industrial Research (CSIR) to jointly develop a *Modular UAV* to act as a national research demonstrator. This would enable various academic research to be applied and tested on this demonstrator platform. This will ultimately be of great benefit to the South African aerospace community in their commitment to building towards a sustainable and internationally recognised aerospace industry sector.

### 1.1 Brief History

To place the research in this thesis in context with the ongoing research at SU, a brief review of the UAV activities at SU is presented.

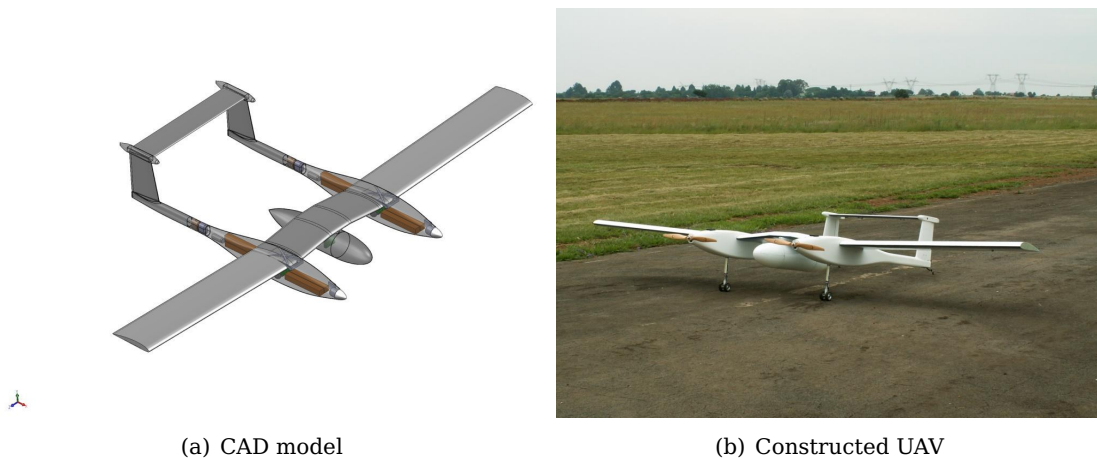
SU's *Centre of Expertise in Autonomous Systems*, was formally established in 2001 as a subdivision of the *Electronic Systems Laboratory (ESL)*. Since its inception, the ESL research group demonstrated its competency in both theoretical modelling and design of control systems as well as designing and developing practical avionics for unmanned air systems (UAS). The following itemised list provides a brief overview of projects completed by the ESL research group.

- Research involved the autonomous flight of rotary-wing and fixed-wing unmanned aircraft. In 2004 a branch of research began into the design of an autopilot system capable of performing aerobatic manoeuvres.
- The automated hovering of a small electrically powered unmanned helicopter and the automated flight of a methanol powered fixed-wing unmanned aircraft was demonstrated in 2005.
- Research continued on fixed-wing and rotary-wing airframes to develop autonomous navigation system for both platforms. In 2006, aerobatic flight of a fixed-wing

UAV was demonstrated and a new branch of research into the control of experimental aircraft such as *Vertical Takeoff and Landing* (VTOL) aircraft and Naval decoy ducted fan concept was pursued.

- The conventional fixed-wing autopilot was successfully extended to handle autonomous takeoff and landing in 2007. Research continued into the development of flight control systems capable of autonomous landing on short runways.
- The autonomous flight and navigation of an unmanned helicopter was demonstrated in 2008. Current research involves autonomous landing of an unmanned helicopter on a movable platform.

The CSIR-SU collaboration to UAV research began in 2007 with a single project aimed at stabilising and controlling a variable stability blended wing-body unmanned aircraft. This stabilisation and control technology was demonstrated practically in late 2008. It was this success that led to further collaboration between the CSIR and SU in the form of the Modular UAV project (presented in Figure 1.1).



(a) CAD model

(b) Constructed UAV

**Figure 1.1:** The Modular UAV research demonstrator

## 1.2 Project Description

The general theme of SU research on the Modular UAV project is *Fault Tolerant Control of UAV's*. This research works towards allowing UAV's to continue to operate in spite of single failures in the system such as structural or mechanical impairment. The UAV should be able to identify that a failure has occurred, diagnose and identify the failure quickly and accurately, reconfigure itself to work around the failure and continue to operate safely though in some cases with a reduction in performance.

This project contributes to the solution of the fault tolerant control problem, by investigating and developing stall detection, prevention and recovery algorithms. Here the fault is considered as some form of disturbance that pushes, or threatens to push the aircraft outside of its desired angle of attack flight envelope. These algorithms form an important part of the fault tolerant control system as they ensure that the aircraft continues to operate safely and remains within its linear aerodynamic region. In turn, this allows the other algorithms in the system to assume simplified aerodynamics models, thus significantly reducing the complexity of the flight control system. The main project outcomes are listed below:

- Develop a stall prevention flight control subsystem that will allow for easy integration into existing flight control architectures.
- The control algorithms should be capable of predicting the occurrence of stall and should apply prompt and effective control inputs to prevent a stall from manifesting.
- These control algorithms should prevent stall without imposing severe restrictions on the operating flight envelope.
- Finally, the performance of these stall prevention control algorithms should be tested through simulation and analysed for robustness.

### 1.3 Structure and Overview

This thesis is structured into three sections. The *Preamble* section gives insight and perspective of the control problem and presents the mathematical aircraft model on which the stall prevention control algorithms will be based. The *Algorithm Development* section forms the main part of this thesis and presents the development of the stall prevention control system. The final section, *Analysis*, will conduct simulations and sensitivity tests on the stall prevention control system developed in this project. The outline of this thesis is presented in Figure 1.2.

In Chapter 2, a literature study is conducted on the topic of aerodynamic stall, investigating various aspects of this phenomenon. This will provide a reference source dedicated to stall, which will contribute to the ESL research group and allow more efficient future research in the field of stall control.

Chapter 3 presents the aircraft model and aircraft dynamics that will be used throughout this thesis. This aircraft model was developed by [1] and accommodates the design of an all attitude flight control system capable of guiding a UAV through the full kinematic flight envelope. The acceleration based manoeuvre flight control system

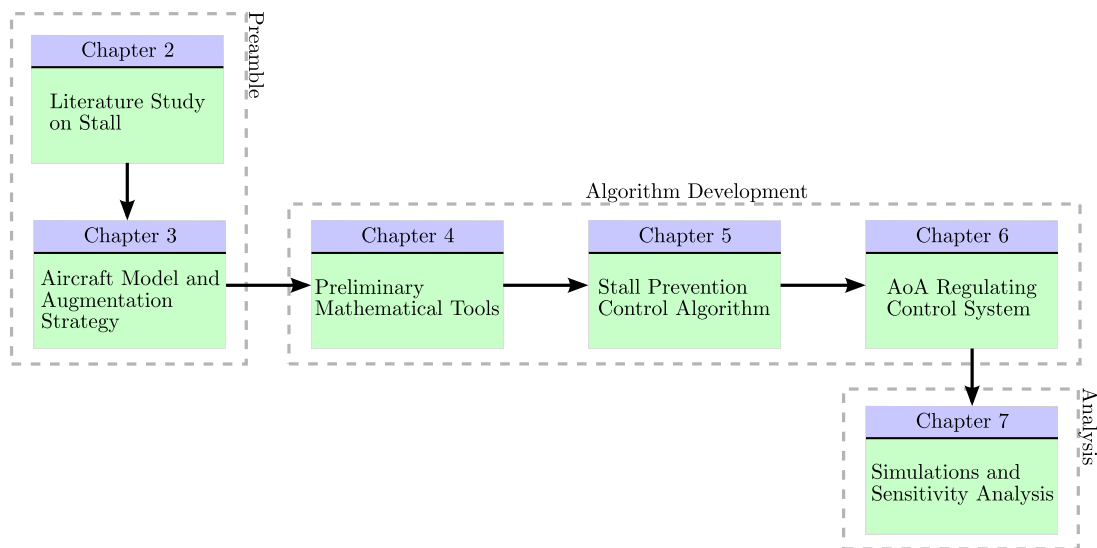


**Figure 1.2:** Thesis outline

developed by [1], will be adopted as the existing flight control system for the development of the stall prevention control algorithms. The chapter also presents the method of how this stall prevention control system will interface with the existing flight control system.

Chapter 4 develops preliminary mathematical concepts and tools that will assist the development of the final stall prevention control system. The tools are based on the concept of forward state propagation and exploits the *Phase Plane* to foresee an approaching stall based on the aircraft's natural dynamics.

Chapter 5 extends the concepts developed in Chapter 4 to account for nonlinearities of a physical control surface. The resulting mathematical tools are directly used to develop an algorithm capable of actively preventing an aircraft from stalling by dynamically limiting the elevator command. The algorithm will ensure that the aircraft will never exceed a predefined angle of attack during its flight envelope.

Chapter 6 follows with the design of a innerloop controller responsible for regulating the angle of attack once stall has been prevented. This will sustain stall prevention control by regulating the aircraft's angle of attack at a predefined limit angle.

Chapter 7 presents the results obtained through *Software-in-the-Loop* (SIL) simulations of the stall prevention control system in a nonlinear simulation environment. The sensitivity of the stall prevention control algorithm to model uncertainties is also investigated through conducting a worst-case performance analysis.

## Chapter 2

# Fundamentals of Stall

This chapter investigates the aerodynamic phenomenon known as *stall* to gain insight into how to prevent it from occurring. Fundamental aircraft geometry and important reference centres are also defined. Practical stall prevention and recovery techniques identified in this chapter, will form the basis to the methodology behind the stall prevention control system.

### 2.1 Theory of Stall

As an aircraft moves through the air, it effectively disturbs the free stream air and deflects the flow over the surfaces of the aircraft. According to *Bernoulli's theorem*<sup>1</sup> this deflected airflow results in a positive difference in total pressure on the top and bottom surfaces of the aircraft's wing due to a complex variation in air velocity and pressure above and below the wing. As a result a net aerodynamic force, normal to the incoming airflow, is generated. This force is known as *lift* and is largely contributed to the aircraft by the wing. For an aircraft to sustain heavier than air flight, the magnitude of this lift force needs to be at least equal to the vehicle's weight. This lift force is accompanied by a force which opposes the movement of the aircraft through the air, known as *drag*. All the structural components of the aircraft contribute to this drag force which mainly consists of two principle types namely, parasitic and induced drag. The former type encapsulates a wide range of different drag forces that does not function to aid flight. The latter type is as a result of the lift produced by the wing aerofoil [3].

The magnitude of the lift generated by the wing is proportional to the angle with which the incoming airflow hits the wing. This angle is known as the *angle of attack*

---

<sup>1</sup>The generation of lift is far more complex than a simple differential pressure between the top and bottom surfaces of an aerofoil section. For more detailed explanations regarding the generation of lift consult [2].



and is measured between the chord line of the wing aerofoil<sup>2</sup> and the incoming air velocity vector. For small angles of attack this proportional relationship is linear, therefore lift increase with increase angle of attack. However for large angles of attack this linear relationship breaks down and becomes nonlinear. Once the angle of attack exceeds the angle coinciding with maximum lift known as the *critical angle*, the lift will decrease with increased angle of attack. This is referred to in aerodynamics as *stall* and the following subsections attempts to investigate this phenomenon by conducting a literature study on the topic of stall.

### 2.1.1 Formal Definitions

A stall occurs when the steady airflow over the wing is disrupted by excessive angle of attack, thus causing the airflow to separate from the wing's surface resulting in a rapid loss of lift. This is caused by the pilot (or autopilot) attempting to fly too slowly, pull up too steeply either in a dive or banked turn resulting in the angle of attack exceeding the critical angle. A stall can therefore occur at any pitch attitude or airspeed [4].

For example an aircraft can be stalled in straight and level flight when flying too slowly. As the airspeed decreases the angle of attack needs to increase to generate sufficient lift to maintain altitude. If the airspeed decreases to such an extent that the angle of attack exceeds the critical angle, the airflow over the wing will be disrupted resulting in insufficient lift to sustain level flight.

Therefore during a stall the wing does not stop producing lift, rather it produces insufficient lift to sustain level flight. Consider the following lift and drag relationship displayed in Figure 2.1 for a typical subsonic aircraft during unaccelerated flight,

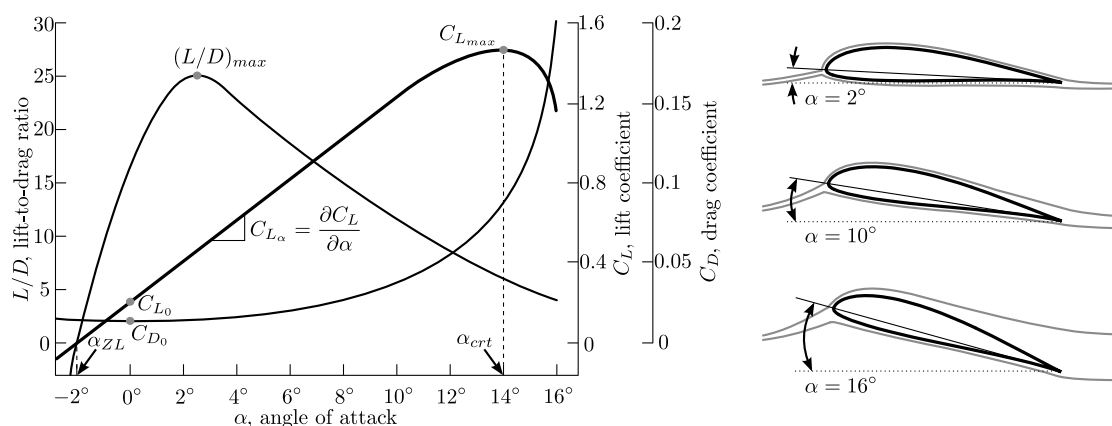


**Figure 2.1:** Typical Lift and Drag polars for a subsonic aircraft

<sup>2</sup>The angle of attack defined here is the general description of the *geometric angle of attack*. The angle of attack measured with regards to the zero lift line (the line parallel with the free stream velocity vector when  $C_L = 0$ ) is known as the *absolute angle of attack*.

where the *critical angle of attack* is denoted by  $\alpha_{crit}$  and the angle of attack at which no lift force is produced is denoted  $\alpha_{ZL}$  and is known as the *zero-lift angle of attack*<sup>3</sup>. For a symmetric aerofoil (zero camber) the latter angle is zero. The lift ( $L$ ) and drag ( $D$ ) characteristics of the aircraft are described by the non-dimensional aerodynamic coefficients  $C_L$  and  $C_D$  respectively where,

$$L = \frac{\rho \bar{V}^2 S C_L}{2} \quad (2.1)$$

$$D = \frac{\rho \bar{V}^2 S C_D}{2} \quad (2.2)$$

with  $\bar{V}$  the air velocity,  $\rho$  the air density and  $S$  the reference area of the wing since it is the main contributor of lift in a conventional subsonic aircraft configuration. Note that the lift curve continues through negative angles of attack and that a negative critical angle of attack also occurs. However, an aircraft will generally operate at positive angles to gain the necessary lift for flight.

Typically at small angles of attack the induced drag is small and changes slightly for a small variation of angle of attack. However at large<sup>4</sup> angles of attack a small variation in angle of attack creates a significant change in induced drag [5].

For small to moderate angles of attack the lift varies *linearly* with  $\alpha$ . The slope of this line is known as the *lift-curve slope* and is denoted by  $C_{L\alpha}$  with the coefficient  $C_{L_0}$  representing the lift force at zero angle of attack. In this region the air flows smoothly over the surface of the wing and is attached over most of the surface which is known as *laminar flow*. However when  $\alpha$  becomes large the flow tends to separate from the top surface creating a large wake of unsteady airflow which is known as *turbulent flow*. Inside this separated region the flow is recirculating causing reversed flow which opposes the freestream airflow due to the viscous properties of air. The consequence of this separated flow at large angles of attack is a decrease in lift with an increase in drag [6].

## 2.2 Geometric Definitions

The aim of this section is to provide the necessary nomenclature used when describing wings and aerofoil properties. Only the name and symbol used will be listed for the respective variables, accompanied by a graphical representation presenting its origin and location. For a more detailed description of the variables consult [7].

This section also investigates the manner in which variations in these geometric variables affect the aerodynamic performance of the wing and thus the aircraft.

---

<sup>3</sup>The zero-lift angle of attack is a geometric property of a given aerofoil section.

<sup>4</sup>Angles of attack is assumed to be large if greater than 10°.

### 2.2.1 Wing and Aerofoil Geometry

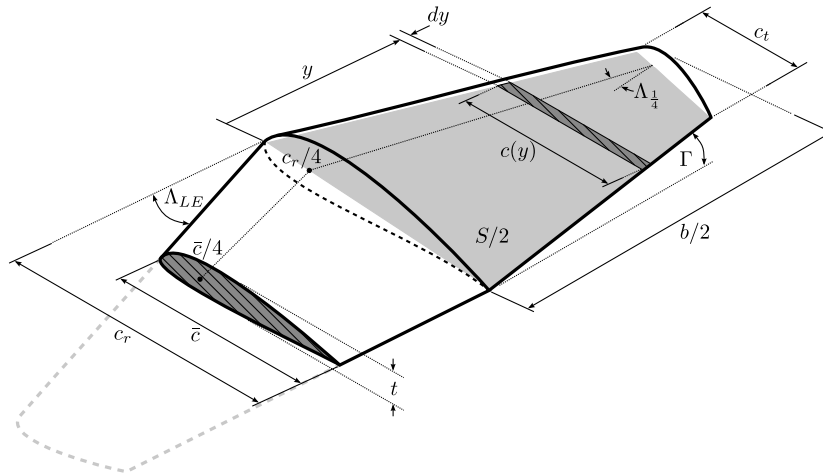


**Figure 2.2:** Geometric properties of a typical subsonic wing

- $c_r$  : Root chord length
- $c_t$  : Tip chord length
- $c(y)$  : Chord length at  $y$ -distance measured from root
- $\bar{c}$  : Mean aerodynamic chord (MAC) length
- $b$  : Span length
- $S$  : Planform area of the wing
- $t$  : Thickness of wing aerofoil
  
- $\Lambda_{LE}$  : Leading edge sweep angle
- $\Lambda_{\frac{1}{4}}$  : Quarter chord sweep angle
- $\Gamma$  : Dihedral angle

There are several parameters that characterise wing geometry of which the *aspect ratio* is the most important. It is a measure of the span length relative to the chord which characterises the wing's slenderness and is given by,

$$AR = \frac{b^2}{S} \quad (2.3)$$

The aspect ratio of a wing affects the slope of its lift curve [8]. High aspect ratio wings have increased lift curve slopes as compared to low aspect ratio wings which have flatter lift slopes. The result is a higher maximum lift coefficient that occurs at a lower critical angle of attack as presented in Figure 2.3. Although low aspect ratio wings have a higher critical angle of attack, the stall on these wings are not properly

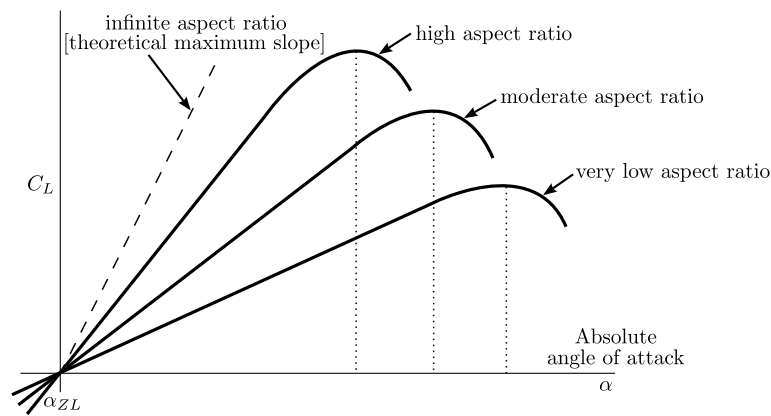


**Figure 2.3:** Effect of aspect ratio on the lift curve of a wing as a function of the absolute angle of attack

defined which could lead to the development of a very high sink rate as opposed to the classic wing stall. Resulting in a loss of altitude without the symptoms of stall.

A two-dimensional cross-section of the wing (parallel to its plane of symmetry) is referred to as an aerofoil section. For a wing that is tapered the chord length of these aerofoil section vary spanwise and is characterised by its *taper ratio* defined as,

$$R_T = \frac{c_t}{c_r} \tag{2.4}$$

Both the taper ratio and the leading edge sweep back angle affect the lift distribution across the wing’s surface making these types of wing planforms prone to *tip stall* which will be discussed later.

Consider the following graphical representation of a two-dimensional aerofoil section presenting the principle geometric properties displayed in Figure 2.4.

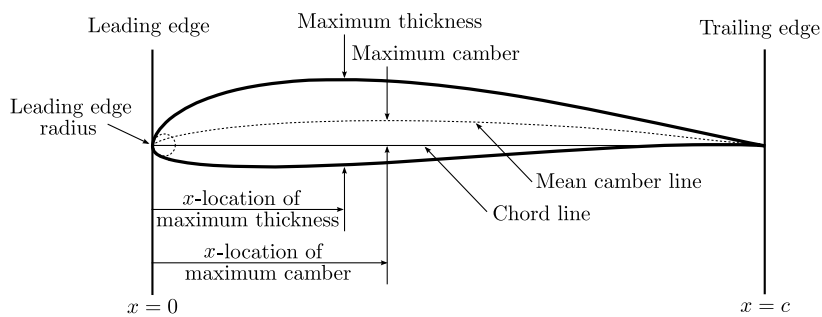


**Figure 2.4:** Geometric properties of a typical subsonic aerofoil

The camber of an aerofoil greatly affects the maximum lift coefficient it can achieve [9]. It defines the zero lift angle of attack and tends to reduce the angle of attack where stall occurs while increasing the maximum lift coefficient. For positive camber

(as indicated in Figure 2.4) the zero lift angle of attack is negative<sup>5</sup>. Similarly, extending trailing edge flaps alters the effective camber of the aerofoil and thus has the same effect on the lift curve by increasing the usable angle of attack range<sup>6</sup> as presented in Figure 2.5. However the thickness has the effect of increasing the maximum lift coefficient and the angle of attack at which it occurs.

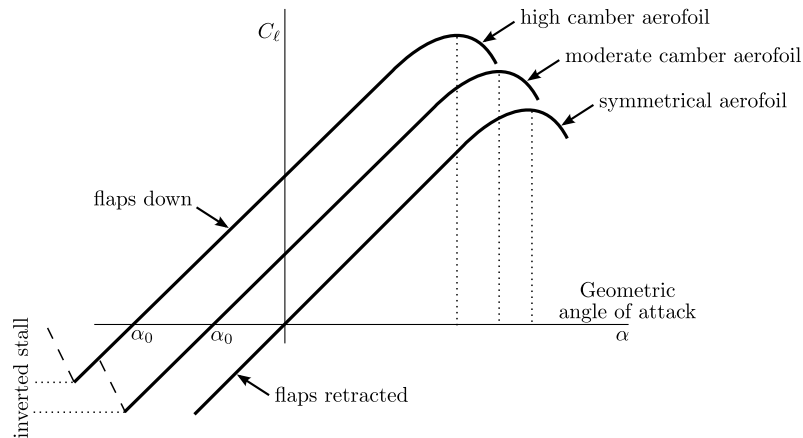


**Figure 2.5:** The effect of camber on the lift curve of an aerofoil section

These two parameters define the shape of an aerofoil which characterises the behaviour of the lift curve at and beyond the critical angle. To allow for safer stall which is easier to recover from, a gentle loss in lift rather than a rapid loss is preferred. Aerofoils with high thickness and camber possess such characteristics but unfortunately also have a lower maximum lift coefficient.

## 2.2.2 Aerofoil Reference Centres

The resultant aerodynamic force generated by an aerofoil, wing or complete aircraft acts at a point known as the *centre of pressure* ( $CP$ ). For an aerofoil section this point is located in the mean camber line extending from the leading to trailing edge as presented in Figure 2.6. This point forms an important aerodynamic reference centre which characterises the pressure distribution across the aerofoil [7].

The resultant aerodynamic force  $F$  is usually comprised of two components namely the aerodynamic force due to the camber of the aerofoil  $F_c$  and the aerodynamic force due to the angle of attack  $F_\alpha$  each of which can be expressed in terms of their respective lift and drag components. The force  $F_c$  is constant for any given camber

<sup>5</sup>An aerofoil with zero camber has a zero lift angle of attack of zero and is referred to as being symmetric.

<sup>6</sup>The usable angle of attack range is measured between the angle of zero lift and the critical angle. Thus increasing the camber delays stall.

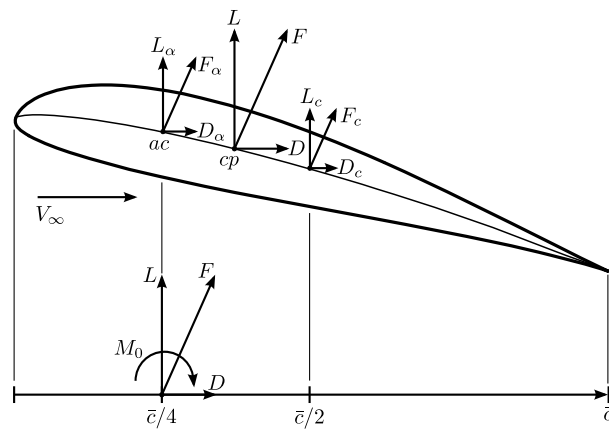


**Figure 2.6:** Reference centres of a typical subsonic aerofoil section

and usually acts at the midpoint on the mean camber line<sup>7</sup>. The force  $F_\alpha$  varies directly with angle of attack and acts at a point known as the *aerodynamic centre* located on the mean camber line. This forms an important aerodynamic reference point and for subsonic aircraft is usually located at the quarter chord point. This explains the reason behind the zero-lift angle of attack which is located at a small negative value for a positively cambered aerofoil. At this angle the lift components of these two forces oppose each other exactly.

During normal flight most of the aerodynamic force is due to the angle of attack dependant contribution. At high angles of attack the *CP* shifts forward and is located close to the quarter chord point. The inverse occurs at low angles of attack when the *CP* shifts towards the mid-chord point. The location of the centre of pressure therefore moves as a function of the angle of attack [10].

From a modelling point of view it is more convenient to reference this aerodynamic force to a fixed point. The most convenient of which is the aerodynamic centre at the quarter chord point. The magnitude of the force is remains unchanged but it is accompanied by a pitching moment. This pitching moment is fixed and defines the aerodynamic force due to camber about the quarter chord point<sup>8</sup>.

### 2.3 Aerofoil Stall Characteristics

Consider the streamline sketch of a section of the wing's aerofoil portraying the change in flow with increased angle of attack displayed on the right of Figure 2.1. Taking a closer look at the disrupted flow over a single aerofoil section yields the following two-dimensional flow representation [11],

<sup>7</sup>This force is zero for a symmetric aerofoil.

<sup>8</sup>The actual aerodynamic centre moves aft as the flight condition Mach number is increased, but remains relatively constant and close to the quarter chord point on the *MAC* during subsonic flight.

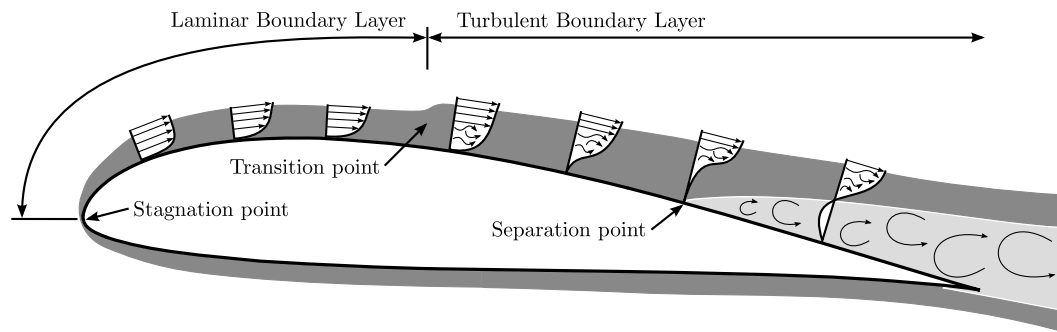


**Figure 2.7:** Flow around the wing's aerofoil displaying exaggerated boundary layer thickness

Air possesses viscosity, since it is not a perfect fluid. According to *Prandtl*, the flow around the aerofoil can be treated as two parts. One part, that is close to the surface of the aerofoil, is the region in which the effects of viscosity are relatively large and is referred to as the *boundary layer*<sup>9</sup>. As a result the flow in the boundary layer experience significant gradients in velocity across it. The second part consists of the flow outside the boundary layer which exhibit negligible viscous effects and hardly any change in velocity gradients across the flow. The flow in this part can be considered as inviscid [6]. The flow velocity in this inviscid region is referred to as the free-stream velocity. The flow velocity at the edge of the boundary layer is 99% of the free-stream velocity and decreases the closer the flow is to the aerofoil surface. The velocity distribution of the flow around the aerofoil is presented by *velocity profiles* indicating the magnitude and direction of the airflow.

The boundary layer may exist in two forms namely *laminar* and *turbulent*. In the laminar boundary layer the flow moves in layers called *laminae* which slide over each other with a regular and smooth behaviour. The closer the layer is to the surface of the aerofoil, the slower they move. In the turbulent boundary layer however, the flow is chaotic and consists of randomly fluctuating eddies. The turbulent boundary layer is considerably thicker than the laminar one. Normally the boundary layer at the front of the aerofoil is in laminar form and very thin and at some point towards the trailing edge, the disturbances on the flow is no longer damped by the viscosity causing a transition into the turbulent form. This is known as *boundary layer transition* which occurs under certain conditions and is located at the transition point [3].

According to *Osborne Reynolds* the behaviour of the flow at this transition can be quantified by the *Reynolds number* which is the dimensionless ratio of inertia to viscous forces and is given by,

$$Re = \frac{\rho V \ell}{\mu} \quad (2.5)$$

where  $\rho$  is the density of the air,  $V$  the free-stream velocity,  $\mu$  the viscosity and  $\ell$  the characteristic length.

<sup>9</sup>The actual boundary layer is hardly a few millimeters thick.

At the transition point (as based on the distance from the leading edge<sup>10</sup>) the Reynolds number reaches a critical value  $\mathcal{R}_{crit}$  and the laminar flow becomes unstable and takes the form of turbulent flow. This critical number is dependant on the roughness and the form of the aerofoil section, and varies with turbulence in the free stream as well as any change in the parameters,  $\rho$ ,  $\mu$ ,  $V$  and  $\ell$ . Therefore at higher Reynolds numbers the airflow in the boundary layer is turbulent and at lower Reynolds numbers the airflow is laminar. Reduced scale aircraft operate at Reynolds numbers in the order of  $10^5$  while full scale aircraft operate at much higher order of Reynolds numbers [9]<sup>11</sup>. As a result the viscous forces of the air at low speed are more dominant for reduced scale aircraft.

The presence of the boundary layer gives rise to two forms of drag namely pressure drag (as a result of the static pressure distribution<sup>12</sup> of the air acting everywhere normal to the surface of the aerofoil) and skin-friction drag (as a result of the shearing stresses between the relative layers of flow) which contributes to the total parasitic drag in the form of *profile drag*.

A typical pressure distribution over a positively cambered aerofoil at positive angle of attack is presented in Figure 2.8. It displays the regions of negative (less than atmospheric pressure) and positive (greater than atmospheric pressure) pressure distributions where the negative distributions are as a result of the camber of the aerofoil [8]. The resultant pressure force acts through the aerofoil's centre of pressure and is mainly contributed to by the negative pressure distribution on the top surface.

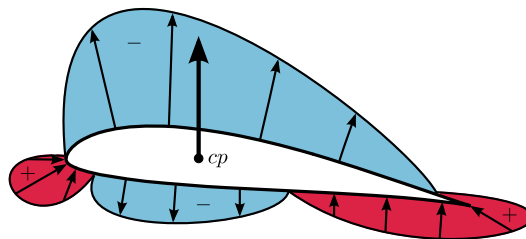


**Figure 2.8:** Pressure distribution over an aerofoil

At the leading edge of the aerofoil the pressure reaches its maximum value. This point is called the *stagnation point* referring to the flow at this point as being at rest. From the stagnation point a pressure gradient is created as a result of the flow accelerating over the top surface leading to laminar and then turbulent flow creating a negative pressure region. As this flow reaches the trailing edge, the increased static pressure

<sup>10</sup>Note that the operating Reynolds number applied to the wing chord is not the same as the Reynolds number in the boundary layer.

<sup>11</sup>For full scale aircraft the transition point occurs relatively close to the leading edge unless special devices are used to remove the turbulent layers.

<sup>12</sup>If this static pressure distribution acting normal to the aerofoil is known, forces on the aerofoil can be determined by integrating this pressure over its surface.



opposes the flow within the boundary layer. This adverse pressure gradient will cause the boundary layer to separate from the surface of the aerofoil resulting in reversed flow which occurs at the *separation point*. This separated flow is referred to as *stalled air* and will eventually close to form a wake [11]. The location of the separation point on the aerofoil greatly affects the amount of lift produced by the aerofoil. For a given  $Re_{crit}$ , if the flow in the boundary layer faces a favourable negative pressure gradient the transition point will occur farther along the surface, however when slower moving air is encountered at an adverse positive gradient the transition point tends to occur earlier along the surface.

As the angle of attack is increased, the pressure distribution around the aerofoil changes causing the centre of pressure to move forward. This causes the separation point (and the subsequent transition point) to move towards the leading edge. For small angles of attack the separation point remains close to the trailing edge, however for angles of attack close to and past the critical angle, the separation point moves rapidly towards the leading edge causing the pressure drag to increase abruptly. Consider the graphical representation of the formation of stall in Figure 2.9.

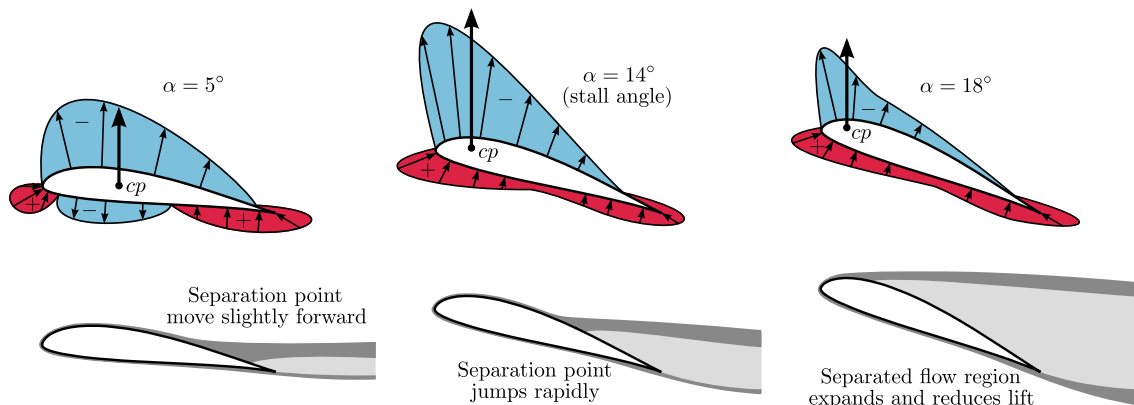


**Figure 2.9:** The formation of stall on an aerofoil section

A direct result of operating at low Reynolds numbers (vehicles of reduced scale flying at low speed) is the occurrence of *laminar separation bubbles* which are almost always present on scale reduced aircraft wings [9]. A separation bubble forms when the lowest lamina becomes stagnant creating a barrier to the upstream airflow. When this barrier grows in size, it forces the laminar boundary layer to separate. If the laminar separation was gradual, it may be followed by turbulent re-attachment since the turbulent layer is thicker considering the Reynolds number is high enough otherwise full separation will result. Consider the graphical representation of this laminar-turbulent transition in Figure 2.10.

The bubble effectively deforms the shape of the aerofoil affecting its aerodynamic performance [12]. As the angle of attack increases the centre of pressure shift forward

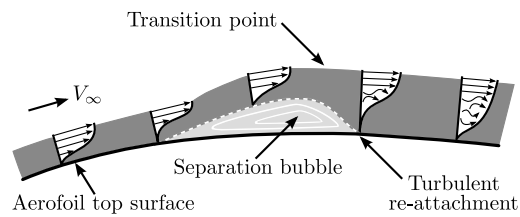


**Figure 2.10:** Laminar separation with turbulent re-attachment

and this separation bubble tends to act in the same way, under certain conditions even becoming shorter in length. The turbulent layer may not have sufficient energy for re-attachment at these high angles of attack. This causes the separation point to move towards the bubble at the leading edge and eventually rupture it. This results in an early stall which is how most wings of scale reduced aircraft stall.

## 2.4 Wing Planform Stall Characteristics

It is advantageous for a wing to possess favourable stall characteristics to ensure the stall is gradual and reduce the tendency to spin after stalling. This is achieved by forcing the wing to initially stall at the root and allowing it to progress towards the wing tips thus preserving the effectiveness of the ailerons at the wing tips during the stall.

The wing planform has a significant effect on the progression of stall over its surface [13]. Figure 2.11 displays the stall patterns for different wing planforms. Notice the rectangular planform is best suited from a favourable stall standpoint which is the reason why it is used on many trainer aircraft [14].

If the wing planform is tapered (assuming a taper of less than 1.0), the tip chord length is smaller than the root chord length which results in a lower operating Reynolds number at the tip than when compared to the root. As mentioned previously, this results in a lower  $C_{L_{max}}$  at the tip and a subsequent lower critical angle of attack for the wing. For a highly tapered planform the wing will stall at the tip first, thus rendering the ailerons inefficient which may lead to roll-off at the stall and ultimately spin.

Similarly, aft swept planforms have a tendency to tip stall due to the spanwise flow across the wing's surface while forward swept planforms tend to stall at the root first. Tip stall on aft swept planforms could lead to serious recovery issues. Since the lift loss is behind the aerodynamic centre of the wing, the lift producing section of the wing is ahead of the aerodynamic centre, thus causing a pitch-up moment threatening to push the aircraft deeper into stall.

The use of wing incidence angle and spanwise twist is often enforced to allow the wing planform to stall at the root first, thus changing the lift distribution across the

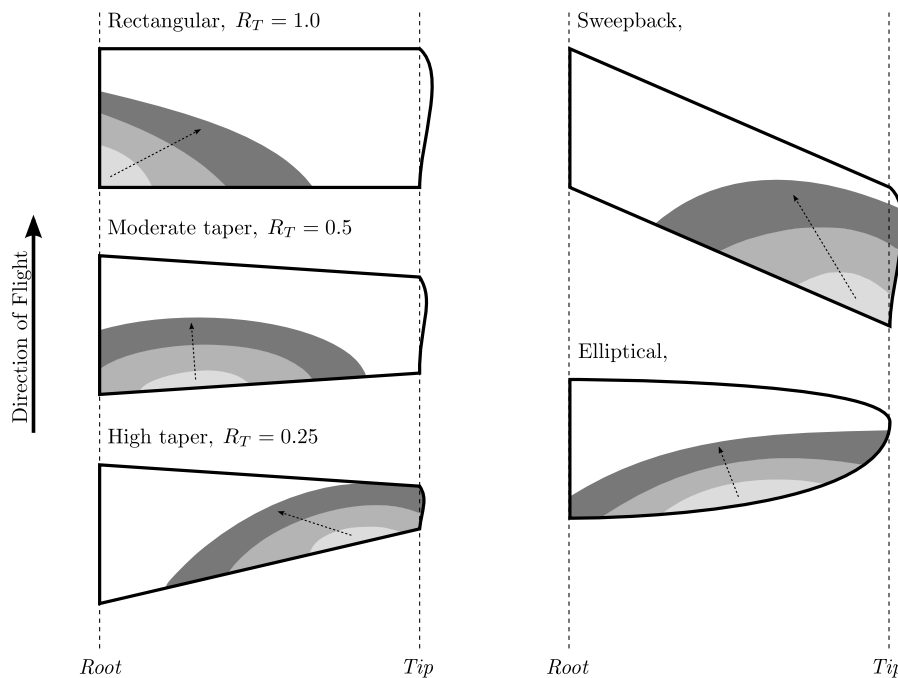


**Figure 2.11:** The effect of the wing planform on stall progression across its surface

wing. Wings are given twist to induce a variation of angle of attack along the span. A decrease in angle of attack at the tip is known as *washout* with the inverse referred to as *washin*. Twist is introduced by two methods namely *geometric* and *aerodynamic*. The former method twist the spanwise local chord lines of the wing. While the latter method varies the camber along the span, thus effectively changing the aerofoil shape from root to tip [6]. By combining these two twist methods, wings of different planforms can be designed to produce desirable lift distributions over a wide range of flight conditions and thus favourable stall characteristics.

## 2.5 Types of Stalls

As mentioned before, a stall can occur at any airspeed or attitude. Note that all stalls result solely from an attempt to fly at excessively high angles of attack. During flight the angle of attack is determined by a number of factors of which the airspeed, gross weight and load factors imposed by manoeuvring are the most important.

Symptoms of an approaching stall include buffeting and shaking as a results of the turbulent flow over the wing. Flight controls become "sloppy" and non-responsive as the air velocity decreases. Different aircraft types exhibit different stall characteristics and it is difficult to specifically describe all of them, however, there exist some similarities which allow stalls to be categorised as follows [15].

**Unaccelerated stalls** can be grouped further into two groups namely *power-off* and *power-on* stalls. The term "unaccelerated" has no reference to the airspeed involved and simply states that the stall occurred during gradual flight conditions.

- Power-off stalls usually occur with normal landing approaches when the power setting of the engine is close to idle and the trim flight condition velocity is reduced to that of a normal approach. When the nose of the aircraft is raised by increasing the pitch attitude, an accidental stall may result.
- Power-on stalls usually occur at takeoff during normal straight climbs or climbing turns with low bank angles (15° to 20°). When the power is set at the desired setting for departure or climb and the aircraft's velocity is close to the normal takeoff speed the nose of the aircraft will raise, accompanied with the climb attitude may result in an accidental stall.

**Secondary stalls** is the term given to a stall that occurs after a successful recovery from a preceding stall. It is usually caused by hastening the stall recovery procedure by attempting to return to normal flight using abrupt control inputs before sufficient airspeed was achieved.

**Accelerated stalls** is the term given to stalls occurring at higher airspeed resulting from excessive manoeuvring during steep turns, hard pull-ups or abrupt changes in the flight path. Again, the term "accelerated" has no reference to the airspeed involved, rather the rate at which the stall is achieved. Accelerated stalls are generally more severe and rapid since they occur at higher speeds and possibly lower pitch attitudes. An aircraft will stall during a coordinated steep turn in much the same manner as during straight flight, however the pitching and rolling motions will be more sudden since the wings stall differentially.

**Deep stalls** usually occur with aircraft that has *T-tail* tailplane configurations. It is the term given when a wake of separated flow produced by the wing approaching a stall, flows over the tailplane thus causing it to lose effectiveness. This makes recovery difficult which, in certain swept wing aircraft, is aggravated by tip-stalling of the wings [3]. When the wings of an aft swept planform tip-stall, the aerodynamic centre shift in front of the aircraft's centre of gravity. This creates a positive pitching moment with the lift produced at the root of the wing, attempting to push the aircraft even deeper into stall.

**Cross-control stalls** is the term given to stalls occurring during *cross-control* conditions when the rudder is applied in one direction and the ailerons is applied in the

opposite direction. When excessive pitch-up-elevator is added to the configuration, an accidental stall may result. This improper control action usually occurs during poorly coordinated base-to-final turns as a result of attempting to align with the runway. Since the aircraft is skidding<sup>13</sup> during the turn, the air velocity over the outside wing speeds up thus causing it to produce more lift. When the aircraft stalls the nose will pitch down and the differential lift will cause the aircraft to roll to an inverted orientation. This is generally the origin of a *spin*.

**Spin** is defined as an aggravated stall which results in *autorotation*. Autorotation occurs as a result of differential angle of attack across the span of the wing at the onset of stall. During autorotation the aircraft follows a downward helix where the outside wing is less stalled than the inside wing causing this rolling, yawing and downward pitching spiral.

### 2.5.1 Stall Speed

As shown by Equation (2.1), the lift generated by an aircraft is proportional to the square of its velocity. Hence there exist a relationship between airspeed and angle of attack. Consider an aircraft travelling at a constant altitude during level-flight. If the velocity is increased, the aircraft would not be able to maintain the same angle of attack, the lift would increase and the aircraft will climb. Thus to maintain the constant altitude, the angle of attack needs to be reduced with the increase in velocity. Conversely with a decrease in velocity the angle of attack would need to increase to generate sufficient lift to maintain altitude<sup>14</sup>. However, the extent to which the angle of attack is allowed to increase is defined by the critical angle of attack as described in this chapter. This velocity when the angle of attack of the aircraft is equal to the critical angle, thus when the maximum lift coefficient occurs, is referred to in aerodynamics as the *stall speed* denoted  $V_S$  [15]. This relationship is presented in Figure 2.12.

Notice that a wide range of angle of attack values near the maximum lift coefficient correspond to velocity values close to the stall speed. The stalling speed is an important parameter since most other criteria is based upon some multiple of the stalling speed, for example, the operating trim velocity ( $V_{trim}$ ) of an aircraft is usually rated as  $1.5 \times (\text{Stall Speed})$  [14].

The stalling speed for a particular aircraft is not fixed for all flight conditions and varies with weight, load factor and density altitude, but a given aircraft always stalls

---

<sup>13</sup>Skidding is defined during a turn when the tailplane of the aircraft steps outward resulting in a positive sideslip angle induced on the vertical stabiliser.

<sup>14</sup>During true equilibrium flight, for every angle of attack there is a corresponding velocity required to maintain constant altitude.

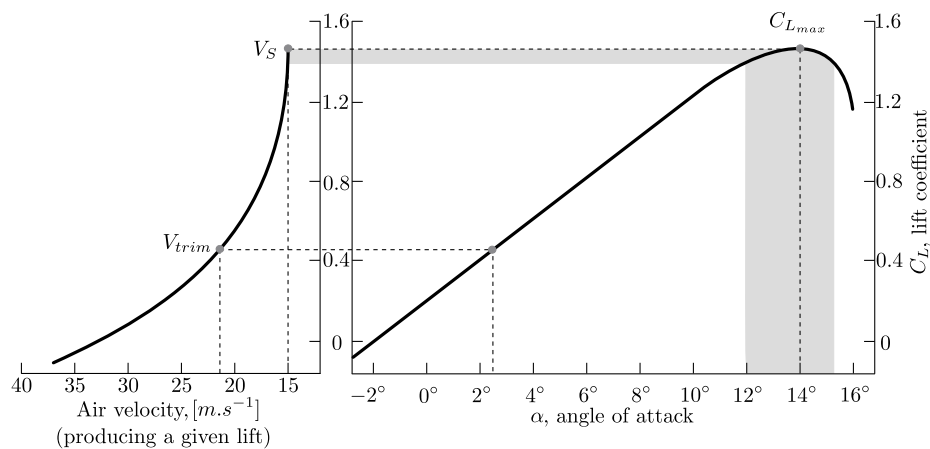


**Figure 2.12:** The relationship between angle of attack and air velocity indicating stall speed

at the same angle of attack regardless. The stall speed will increase as the weight increases since the maximum lift coefficient is a fixed value. As the velocity decrease towards the stalling speed, the aerodynamic control surfaces lose their effectiveness and become less responsive. If the velocity drops below the stall speed, controlled flight becomes impossible since the airflow become too slow to produce any noticeable aerodynamic forces. The following section describes how load factor affects the stall speed.

### 2.5.2 Load Factor

During straight-and-level flight, the forces acting on the aircraft are in equilibrium. When the aircraft is deflected from this flight condition, the force applied produces stress on its structure and is measured as *load factor* [15]. Load factor is the ratio of the maximum load an aircraft can structurally sustain to the gross weight of the actual aircraft. Load factor is calibrated in gravity's (g's) and indicates the force to which the aircraft is subjected when it accelerates<sup>15</sup>.

Load factors are important since an increased load factor increases the stalling speed which in turn makes stall possible at higher velocities. Studies concluded that the stalling speed increases proportional to the square root of the load factor. This is usually apparent during steep turns and hard pull-ups from steep dive manoeuvres.

During a coordinated turn at a constant altitude, the aircraft experiences a load factor dependent on the bank angle as presented in Figure 2.13. If the bank angle is increased, the lift produced by the wing also needs to increase to counterbalance the imposed additional load in order to maintain altitude. This increases the wing's angle

<sup>15</sup>An example of this is when an aircraft pulls out of a dive. If the load factor during the dive measures 3G's, the load on the aircraft becomes three times its normal gross weight. Equivalent to making the aircraft three times heavier.

of attack by applying pitch-up elevator. If at any time during this turn the angle of attack becomes excessive, the aircraft will stall.

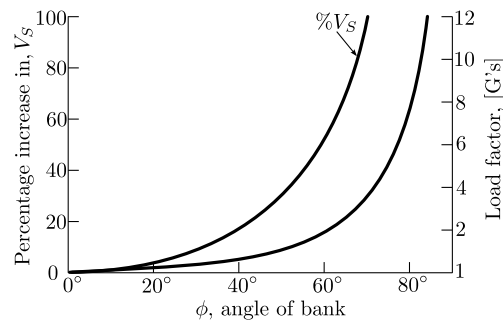


**Figure 2.13:** The relationship between stall speed and load factor during steep turns

Similarly during dives, if the aircraft is forced to pull-up to quickly the imposed load factor will require additional lift to exit the current flight path. This lift can only be produced by increasing the angle of attack. Thus as a result of the relative direction of the oncoming wind, the angle of attack is forced to change abruptly. This sudden change in angle of attack will cause the aircraft to reach the critical angle at much higher speeds.

When an aircraft stalls at high velocities, severe stress is imposed on its structure by the increased load factor. This leads to a constraint on the velocity at which an aircraft can be stall without any inflicted structural damage. This velocity is defined as the *design manoeuvring speed* denoted as  $V_A$ . The effect of this velocity can clearly be seen on a *V-n diagram* which is used to present an aircraft's flight operating strength for a particular gross weight and altitude as displayed in Figure 2.14.

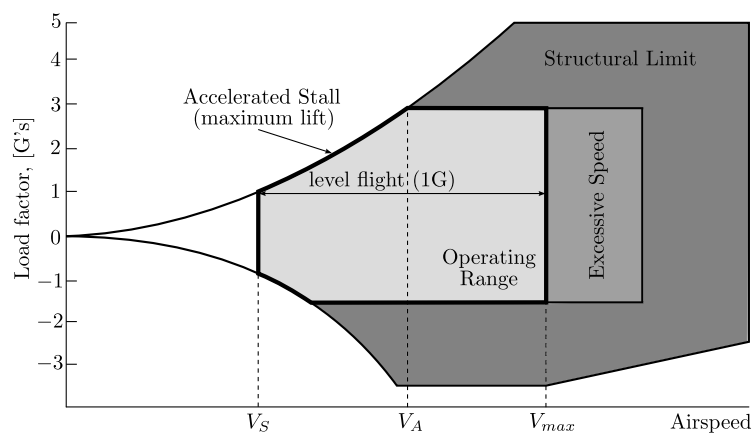


**Figure 2.14:** Typical V-n diagram of an aircraft

The diagram also indicates the maximum lift capability (constrained by the critical angle of attack) of the aircraft which limits the load factor that the aircraft is allowed

to pull to prevent stall [14]. A classic stall entered from straight-and-level flight, or from an unaccelerated straight climb, do not add load factors beyond the 1G of straight-and-level flight. However, during a classic stall the load factor may decrease toward zero.

### 2.5.3 Ground Effect

When an aircraft in flight comes close<sup>16</sup> to the ground (or water) surface, the vertical component of the three-dimensional airflow around the wing is restricted. This interference of the ground is known as the *ground effect* [3].

Ground effect alters the spanwise lift distribution across the wing by reducing the induced angle of attack and thus the induced drag. The result is that the wing will require a lower angle of attack (thus less velocity) to produce the same lift coefficient. A large reduction in induced drag will only become apparent when the wing of the aircraft is very close to the ground as presented in Figure 2.15 with  $K_L$  the ground effect correction factor. Therefore ground effect is usually recognised during takeoff and landing.

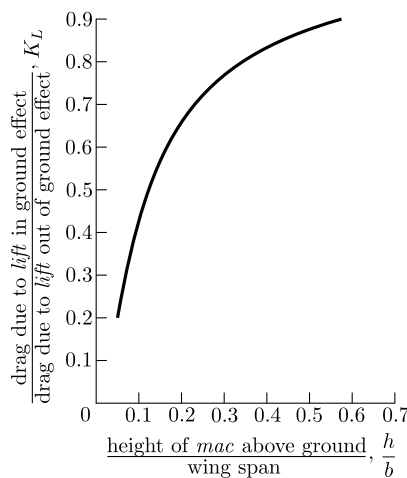


**Figure 2.15:** The effect of altitude on the drag due to lift

During takeoff, the reduction in required takeoff velocity may permit the aircraft to become airborne [15]. Depending on the air density, altitude, temperature and aircraft's weight, it may not be able to sustain lift out of the ground effect. This could lead to poor climb performance and may result in stall after takeoff.

<sup>16</sup>The ground effect only becomes apparent at heights smaller than the aircraft's wingspan.



## 2.6 Classical Stall Prevention and Recovery

The best cure to the problem of stall is to prevent it from occurring in the first place. Several types of stall warning devices and indicators have been developed to alert of an imminent stall. The use of such indicators are desirable to foresee an approaching stall.

In the unfortunate event of an approaching stall, prompt and effective preventative action should be taken to prevent a completely stalled condition from manifesting. Since the fundamental cause of all stalls are excessive angle of attack, the pitch attitude and angle of attack must be decreased immediately at the first indication of stall. This is achieved by applying pitch-down elevator control to lower the nose of the aircraft [15]. The amount of elevator control required to prevent stall depends on the severity of the stall, the altitude above ground and the effectiveness of the elevator of the aircraft. The objective is to lower the angle of attack just enough for the wing to regain lift<sup>17</sup>.

The smooth application of power can also be administered to increase the airspeed and assist in reducing the angle of attack of the wing. Though the application of power during recovery depends on the type of stall and the altitude available, it is not essential for a safe recovery but plays an integral role in minimizing the altitude lost during recovery procedures. However, as the airspeed increases after the stall recovery, the power should be reduced to prevent excessive airspeed. After sufficient lift and airspeed is regained, the aircraft should be coordinated back to level flight applying caution to prevent a secondary stall from occurring.

Depending on the stall characteristics<sup>18</sup> of the aircraft, the ailerons and rudder can be used to maintain wings-level (directional control) during the stall and recovery procedure. This prevents further complications such as spins. Rectangular wing planforms exhibit stable stall characteristics by stalling at the root first thus allowing the ailerons to still be effective during stall recovery. Care should be taken when applying aileron control during stall recovery to avoid aggravating the stall condition. Coordinating the aircraft's yaw with rudder control to maintain straight-flight during recovery will avoid the occurrence of spin.

---

<sup>17</sup>In a well designed aircraft, a strong pitch-down moment will naturally be induced when the wing stalls, thus assisting in the recovery.

<sup>18</sup>The position of the aircraft's CG also play an important role in the stall recovery characteristics of the aircraft. If the CG is located aft the aerodynamic centre of the aircraft, the elevator might not be able to pitch the nose down and the aircraft will plunge deeper into stall.

**In summary:** The correct recovery technique would be to,

- decrease the pitch attitude by applying pitch-down (positive) elevator to break stall,
- increase the power setting to increase airspeed and minimise altitude loss,
- while simultaneously coordinating the ailerons and rudder to maintain directional control,
- smoothly return to level flight after sufficient lift has been regained by the wing.

### 2.6.1 Stall Warning and Safety Devices

Today all modern aircraft have some form of stall warning device to alert the pilot of an impending stall. Usually the first indication of an approaching stall is buffeting. At the wing this results in vibrations and at the propeller this results in an audible change in pitch. In addition, aircraft are also fitted with mechanical or electronic devices, to warn or delay an impending stall. The purpose of stall warning devices is to warn the pilot a few degrees before the critical angle, while the purpose of stall safety devices are to delay the stall from manifesting by altering the airflow across the wing. Typical stall warning and safety devices used are listed below,

- A *stall warning vane* is a movable metal tab mounted below and aft the leading edge of the wing. During low angle of attack flight, the stagnation line is forward of the vane and the airflow forces the vane down. As the angle of attack increases towards the critical angle, the stagnation line moves aft and underneath the wing. When the stagnation line moves past the vane, the airflow will change direction and force the vane upward. This can then be used to activate either a audible warning horn or a mechanical *stick shaker/pusher* device.
- A *stall warning reed opening* is an orifice, sensitive to pressure changes, located just below the leading edge of the wing. During low angle of attack flight, the leading edge of the wing is a low-velocity, high-pressure region. At high angles of attack, the leading edge of the wing becomes a high-velocity, low-pressure region. When this low-pressure region extends far enough along the lower surface of the wing, towards the location of the reed opening, the pressure difference between the inside and outside of the opening will cause air to flow through a harmonic reed, thus producing an audible warning.
- Stall safety devices such as *stall strips*, *winglets* and *stall fences* are designed to force and contain the formation of stall on a wing respectively. *Vortex generators* however, are designed to energise the boundary layer and increasing its inertia

by mixing free stream airflow with boundary layer flow to create vortices. This results in a delayed stall formation.

*High-lift systems* is the term used for aerodynamic devices affixed to a standard wing which has the primary purpose of increasing or decreasing the lift and drag produced by the wing<sup>19</sup>. These aerodynamic devices include leading and trailing edge flaps, slats, slots and spoilers [11]. The main disadvantages of these devices are the added weight, cost and complexity to the wing structure. There exist many different configurations and combinations of these devices, a few of which are indicated in Figure 2.16. Consider the following definitions of a few of these devices.

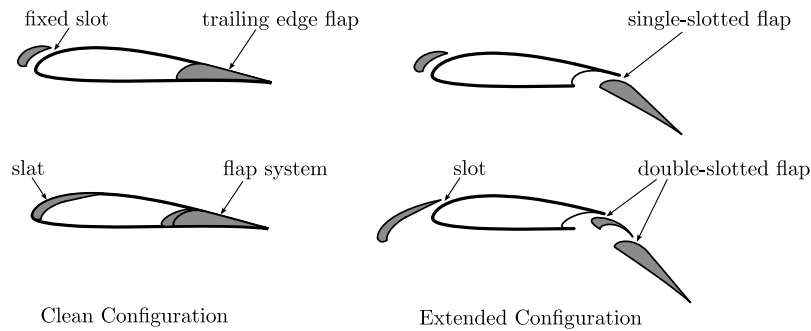


**Figure 2.16:** Types of configuration used with aerodynamic high-lift devices

**Slots** are boundary layer control devices which channels the airflow and delays separation. Slots are carefully designed gaps created by moveable surfaces on the leading edge of the wing extending forward. They serve to permit higher maximum lift coefficient at higher critical angle of attack, as presented in Figure 2.17.

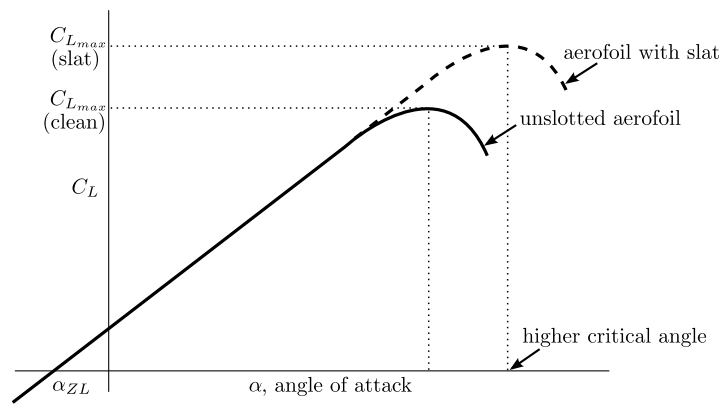


**Figure 2.17:** The effect of slots on the lift curve of a wing

<sup>19</sup>The secondary purpose of the aerodynamic devices is to achieve the highest possible lift-to-drag ratio during the increased lift coefficient at takeoff.

**Slats** are leading edge devices which allows the air underneath the wing to flow over the wing's top surface, ergo delaying airflow separation during high angle of attack flight. Slats can be fixed, movable or pilot operated. Movable slats are flush against the wing at low angles of attack due to the high pressure at the leading edge. As the angle of attack increases, this high pressure area moves aft on the bottom surface of the wing, allowing the slats to move forward.

**Flaps** are moveable surfaces on the trailing edge of the inboard part of the wing which are deflected to increase lift during takeoff and landing. As mentioned before, flaps act to change the shape of the aerofoil by increasing its camber. This increase the lift coefficient over the entire angle of attack range as presented in Figure 2.5 [6]. Flaps can also be located at the leading edge of the wing, hence *leading edge flaps*. Slots within in flaps help to delay separation over the flap aerofoil.

**Spoilers** are high drag devices also known as *speed brakes*. These devices are usually applied during final approach and designed to reduce lift by causing a large separation wake when deployed. This increases the pressure drag thus slowing the aircraft down and controlling the speed of decent<sup>20</sup>.

## 2.7 Summary

This chapter investigated and described the phenomenon of aerodynamic stall, removing any ambiguities that may be encountered in this concept. It provided a clear understanding of how to prevent stall from occurring and the best procedures to safely recover the aircraft in the event of stall. This investigation forms the foundation behind the concepts developed during this project and will assist the design of the control algorithms that will prevent the aircraft from stalling.

The next chapter introduces the mathematical aircraft model that will be used during the development of the stall prevention control system. The existing flight control system with which the stall prevention control system needs to interface, will be presented briefly to give perspective. The focus will be structure of the interface architecture that defines the stall prevention control strategy.

---

<sup>20</sup>It is in the interest of safety for an aircraft to land at the slowest velocity possible, which in turn also reduces the required runway length.

## Chapter 3

# Mathematical Aircraft Model and Control

This chapter presents the mathematical aircraft model developed by [1], that will be used during the project. It starts by introducing the axis systems and notations used during this modelling process. The structure of the existing flight control system is presented with emphasis on the controllers influencing the aircraft's angle of attack. The structure of the stall prevention control system, that will augment the existing flight control system, will be presented.

### 3.1 Axis Systems and Notation

Since aircraft has six degrees of freedom, it is necessary to define the appropriate axis systems in order to effectively model the motion of the aircraft through space. The motion of the aircraft is described by a number of variables that relate to these suitably chosen axis systems. At least two axis systems need to be defined for a complete description of aircraft motion. An earth fixed axis system and an aircraft fixed axis system. The former captures the gross movement and attitude of the vehicle while the latter captures the translation and rotation of the vehicle itself. By describing the relative motion between these axis systems, the dynamics of the aircraft can be derived and modelled. Consider the definitions following axis systems.

#### 3.1.1 Earth Axes

This axis system defines a horizontal plane, tangential to the Earth's surface, with right handed orthogonal axes about a conveniently chosen fixed reference point. Assuming the flight path of the aerial vehicle is in the vicinity of the reference point<sup>1</sup>

---

<sup>1</sup>This assumption is adequate given typical flight paths of unmanned aerial vehicles.

allows the Earth's surface to be considered *flat* and *non-rotating*. This defines an inertial reference frame to which Newton's laws of motion can be applied. This allows the framework in which the absolute position, velocity and attitude of the aerial vehicle can be described. A graphical representation of this inertial reference frame is presented in Figure 3.1.

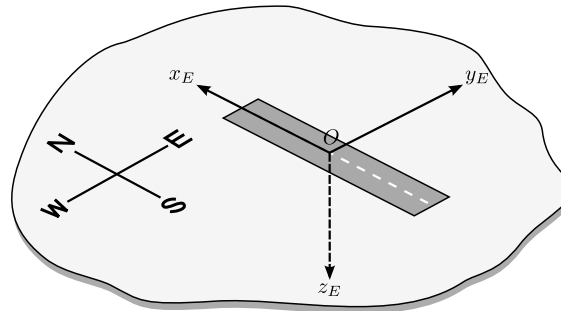


Figure 3.1: Inertial Reference Frame

### 3.1.2 Aircraft Axes

The aircraft axes is a right handed orthogonal axis system fixed to the aerial vehicle and hence rotates and translates with it. Since Newton's equations only apply to an inertial reference frame, the motion of the aircraft axes needs to be defined relative to the inertial frame through transformation. The general form of the aircraft axes is the *body axis system* with the origin coinciding with the vehicle's centre of gravity (*cg*). The aircraft's plane of symmetry is defined by the  $(O, x_B, z_B)$  plane. The  $(O, x_B)$  axis extends directly forward, parallel to the geometrical *horizontal fuselage datum*, perpendicular to the  $(O, y_B)$  axis directed to starboard<sup>2</sup>. The  $(O, z_B)$  axis is directed downwards, perpendicular to the  $(O, x_B, y_B)$  plane. Figure 3.2 presents the body axis system with the notations and conventions for the forces, moments, velocities, angular rates and actuator deflections used throughout this research project. All arrows indicate the positive sense.

A set of aircraft axes more suitable for defining the aerodynamic forces and moments acting on the aerial vehicle, is known as the *wind axis system*. The wind axes has the same origin as the body axes but instead of aligning with the horizontal fuselage datum, the wind axes aligns with the oncoming free-stream airflow. Therefore the wind axes are related to the body axes through the longitudinal rotation of *angle of attack* ( $\alpha$ ) and the lateral rotation of *angle of sideslip* ( $\beta$ ). These two steps of transformation is presented in Figure 3.3.

<sup>2</sup>Starboard implies the right wing of the aerial vehicle from the perspective of a pilot on board the aircraft.

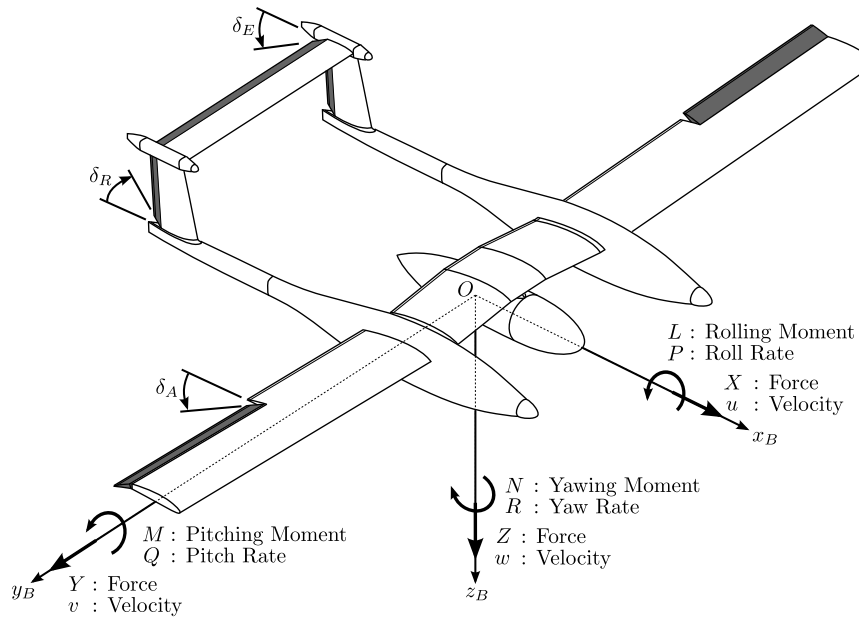


**Figure 3.2:** Body axis system definition with variable notations and conventions

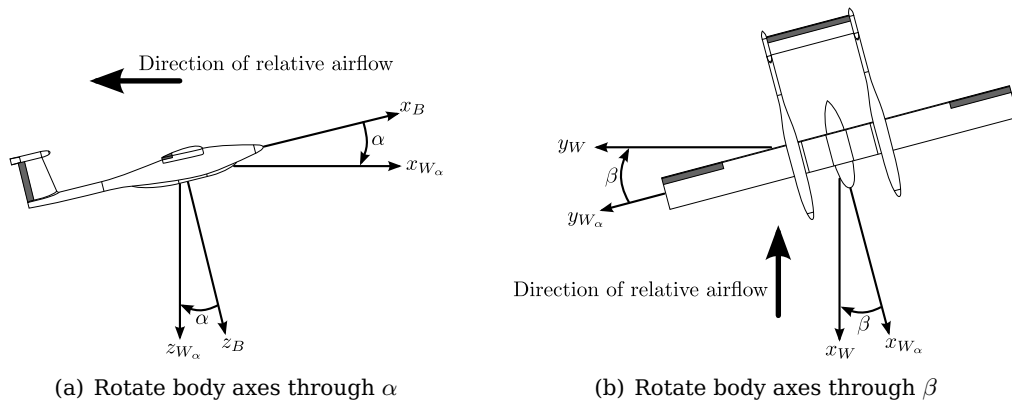


**Figure 3.3:** Body axes transformation to wind axes

### 3.1.3 Aircraft Actuation

The sign conventions presented in Figure 3.2 to define the positive deflection angles of the various control surfaces are adopted from [7]. For conventional aircraft a positive control surface displacement gives rise to a negative aircraft response. Therefore:

- Elevator displaced downward (positive elevator deflection)  $\Rightarrow$  nose down pitch response (negative pitching moment).
- Port aileron displaced up, starboard aileron displaced down (positive aileron deflection)  $\Rightarrow$  starboard wing up roll response (negative rolling moment).
- Rudder trailing edge displaced towards port side (positive rudder deflection)  $\Rightarrow$  nose to port side yaw response (negative yawing moment).

## 3.2 Numerical Aerodynamic Analysis

This analysis attempts to numerically identify the critical angle of attack at the maximum lift coefficient as well as the maximum angle of attack that defines the limit of the linear lift region, by utilising aerodynamic software. The software applications that were used for this analysis are freeware, since that is what was available. These applications are *XFOIL v6.96* and *XFLR5 v4.16*. Analysis with these applications will result in a rough estimate of the angle of attack limits for this aerial vehicle. For the purpose of this research project, the level of accuracy will be sufficient, since the angle of attack values determined from this analysis do not impose any restrictions on the development of the stall prevention control algorithms. The algorithms will allow for any maximum angle of attack to be defined by the designer. For a more detailed analysis, consult Appendix B.4.

### 3.2.1 Simulation Results from Analysis

Conducting a polar analysis by sweeping through a range of angle of attack values in viscous airflow and accumulating the results will yield the lift and drag polars as a function of the angle of attack. These results are presented in Figure 3.4 displaying the nonlinear nature of the lift and drag produced.

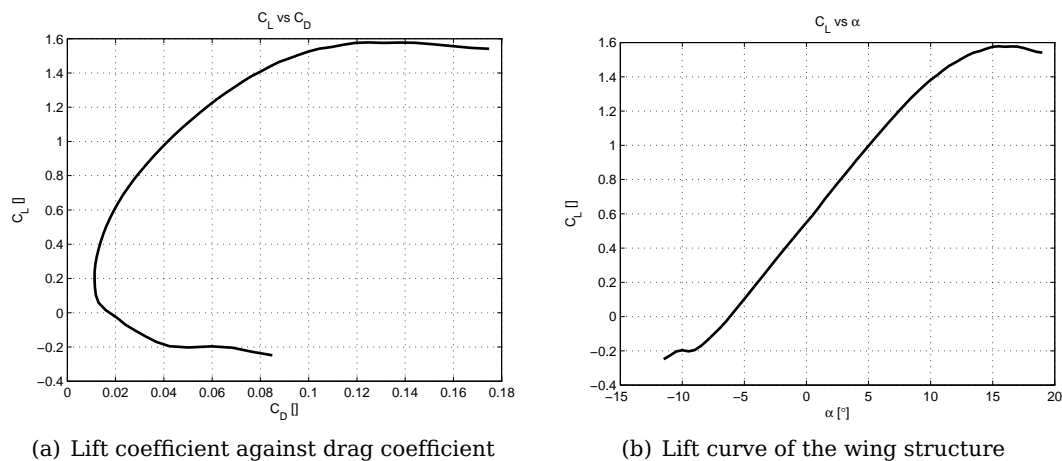


**Figure 3.4:** Polar plots for lift and drag coefficients simulated with XFLR5 on wing structure

Because the wing planform is rectangular, it displays desirable gradual stall characteristics. Notice that the angle of attack value of  $10^\circ$  lies at the edge of the linear lift region. Exceeding this angle results in a nonlinear relationship between lift and angle of attack. The drag curve is the superposition of the friction drag ( $C_{D_f}$ ) and the pressure drag ( $C_{D_p}$ ) as a result of the skin friction and the surface pressure respectively. With the friction drag being dominant at low angle of attack values and the



pressure drag dominant at large angle of attack values. The negative angle of attack limit seems to lie close to  $-10^\circ$ . Since the lift curve becomes irregular for negative values, this angle of attack limit is merely an approximation and a more conservative value needs to be chosen as the negative limit of the linear lift region.

### 3.3 Aircraft Model

During this research project the aircraft model developed in [1] is assumed throughout. It describes the aircraft as a point mass with a steerable acceleration vector by conveniently separating the six-degrees-of-freedom vehicle dynamics into point mass kinematics and rigid body rotational dynamics. The point mass kinematics describe the relative motion of the wind axis system with respect to the inertial reference frame. While the rigid body dynamics describe the relative motion between the wind axis systems and the body axis system. These two sets of dynamics are coupled and interface with each other at an acceleration level. Consider the graphical representation of this decoupled aircraft model presented in Figure 3.5.

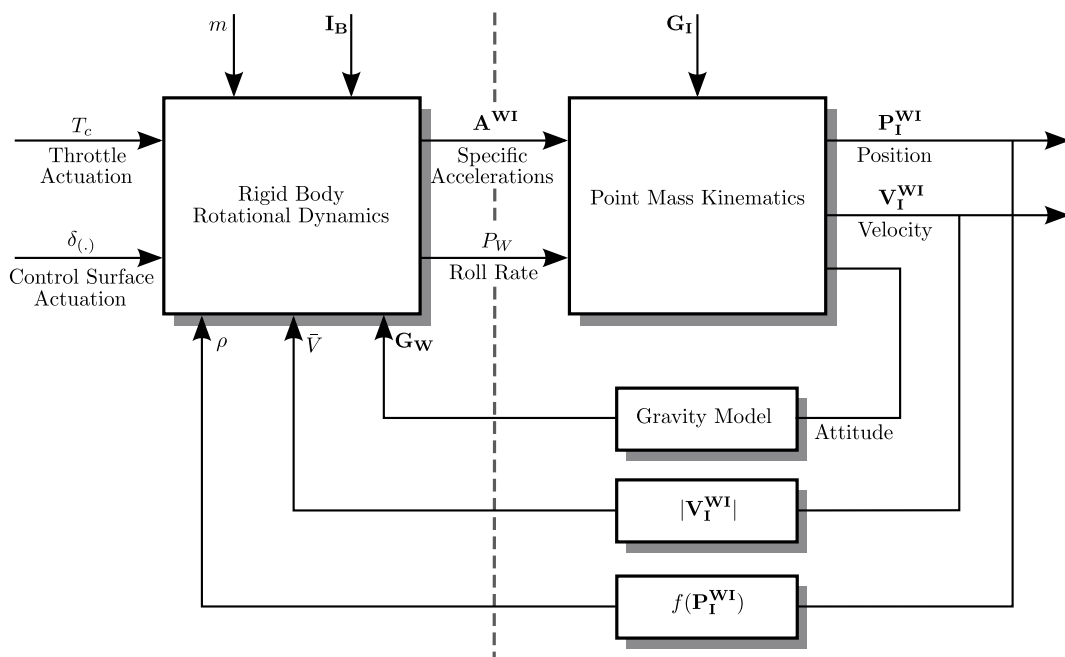


Figure 3.5: Six-degrees-of-freedom equations of motion aircraft model

With this split the specific acceleration coordinates in the wind and body axes will remain independent of the attitude of the wind-axis system. This allows the specific acceleration vector to be regulated independently of the aircraft's gross attitude. In addition, all aircraft specific uncertainty is contained within the rigid body rotational

dynamics and the point mass kinematics only couple back into the rigid body rotational dynamics through the velocity magnitude  $\bar{V}$ , air density  $\rho$  and flight path angle  $\theta_W$  through gravitational coupling.

As was discovered in Chapter 2, the problem of stall is constrained to the longitudinal motion of the aircraft. Therefore only the longitudinal dynamics will be considered during the development of the control algorithms in this project. The dynamic equations that describe the longitudinal motion of this aircraft model will now be presented.

### 3.3.1 Longitudinal Dynamics

When only the longitudinal motion of the aircraft is considered, it is assumed that all the lateral terms reduce to zero and that the aircraft only operates in its plane of symmetry.

The point mass kinematics governs the motion of the aircraft's centre of mass through inertial space. This includes the kinematics (attitude, acceleration, velocity and position) of the CG in the wind axes with respect to the inertial reference frame. The specific accelerations and roll rate of the wind axes are provided as inputs by the rigid body rotational dynamics. These kinematic relationships are expressed as,

$$\left. \frac{d}{dt} \mathbf{P}^{WI} \right|_I = \mathbf{V}^{WI} \quad (3.1)$$

$$\left. \frac{d}{dt} \mathbf{V}^{WI} \right|_I = \mathbf{A}^{WI} \quad (3.2)$$

where  $\mathbf{P}^{WI}$ ,  $\mathbf{V}^{WI}$  and  $\mathbf{A}^{WI}$  are the position, velocity and acceleration vectors of the wind axes with respect to the inertial axes respectively as shown in Figure 3.5. It is more desirable to describe the velocity vector in terms of the velocity magnitude and attitude of the wind axis system, since the autopilot requires the specific accelerations to be coordinated in the wind axes. Considering only longitudinal motion, from [16] these dynamic relationships reduce to the following set of equations,

$$\dot{\theta}_W = -\frac{(C_W + g \cos \theta_W)}{\bar{V}} \quad (3.3)$$

$$\dot{\bar{V}} = A_W - g \sin \theta_W \quad (3.4)$$

$$\dot{N} = \bar{V} \cos \theta_W \quad (3.5)$$

$$\dot{D} = -\bar{V} \sin \theta_W \quad (3.6)$$

where  $N$  and  $D$  are the north and down positions,  $g$  the gravitational acceleration,  $\bar{V}$  the velocity magnitude,  $\theta_W$  the flight path angle with  $A_W$  and  $C_W$  the axial and normal specific accelerations in wind axes respectively.

The rigid body rotational dynamics governs the relative rotational motion of the aircraft's body axis system relative to the wind axis system. This rotational motion is as a result of the point of application of the total force vector, thus the moment about the aircraft's centre of mass. By assuming the aircraft's body is rigid, Newton's equations of motion for a single arbitrary mass element can be used to develop these kinetic relationships for the entire aircraft body. Considering only longitudinal motion, from [16] these dynamic relationships reduce to the following set of equations,

$$\dot{Q} = \frac{M}{I_{yy}} \quad (3.7)$$

$$\dot{\alpha} = \frac{Q + (C_W + g \cos \theta_W)}{\bar{V}} \quad (3.8)$$

where  $Q$  is the pitch rate,  $M$  the pitching moment,  $I_{yy}$  the pitching moment of inertia and  $\alpha$  the angle of attack.

Through the use of a commonly used aircraft force and moment model, these specific acceleration terms can be expanded into the following form as shown by [16],

$$A_W = \frac{(T \cos \alpha - D)}{m} \quad (3.9)$$

$$C_W = -\frac{(T \sin \alpha + L)}{m} \quad (3.10)$$

where  $T$  is the achieved thrust,  $m$  the aircraft's mass,  $L$  and  $D$  the lift and drag respectively. A reduced form of this force and moment model, with all lateral terms reduced to zero, is described as follows.

**Aerodynamic Forces** The aerodynamic forces are typically a function of the dynamic pressure, attitude of body axes with respect to the wind axes, angular velocity of body axes with respect to inertial space and the control surface actuator inputs. They are commonly modelled in the wind axis system since the lift and drag forces are defined as perpendicular and parallel to the free stream velocity vector respectively. An aerodynamic model derived in [17] valid for small incidence angles and coordinated in wind axes is presented below,

$$\begin{bmatrix} D \\ L \end{bmatrix} = \mathbf{q}S \begin{bmatrix} C_D \\ C_L \end{bmatrix} \quad (3.11)$$

$$M = \mathbf{q}S\bar{c}C_m \quad (3.12)$$

with,

$$\mathbf{q} = \frac{1}{2}\rho\bar{V}_a^2$$

where  $q$  is the dynamic pressure,  $\rho$  the air density,  $\bar{V}_a$  the relative air velocity,  $S$  the wing area,  $\bar{c}$  the mean aerodynamic chord and  $b$  the span of the wing respectively.

The dimensionless aerodynamic coefficients capture the specific aerodynamic properties of the aircraft's airframe. These include  $C_D$  and  $C_L$  which are the drag and lift force coefficients respectively and also  $C_m$  which is the pitching moment coefficient. These coefficients can be expressed in terms of their stability and control derivatives as follows [17],

$$C_D = C_{D_0} + \frac{C_L^2}{\pi \mathcal{R} e} \quad (3.13)$$

$$C_L = C_{L_0} + C_{L_\alpha} \alpha + \frac{\bar{c}}{2\bar{V}_a} C_{L_Q} Q + C_{L_{\delta_E}} \delta_E \quad (3.14)$$

$$C_m = C_{m_0} + C_{m_\alpha} \alpha + \frac{\bar{c}}{2\bar{V}_a} C_{m_Q} Q + C_{m_{\delta_E}} \delta_E \quad (3.15)$$

In Equation (3.13) the first term ( $C_{D_0}$ ) indicates the parasitic drag (independent of lift) and the second term the induced drag with  $\mathcal{R}$  the aspect ratio of the wing and  $e$  the *Oswald efficiency factor*. The parasitic drag varying with lift is accounted for by the efficiency factor. The static lift ( $C_{L_0}$ ) and pitching moment ( $C_{m_0}$ ) coefficients are presented in Equation (3.14) and (3.15) respectively.

It is assumed that the stability and control derivatives are not a function of the rigid body rotational dynamic states and therefore do not change over time. This however is only valid for the angle of attack range where the airflow over the wing's surface remains laminar. This is valid for aircraft operating in the small incidence angle range and greatly simplifies the aerodynamic model. Note that the effects due to added mass and downwash lag have been ignored since their effect on a scale aircraft is negligible. Thus the stability derivatives for the first time derivative states are assumed as zero.

**Propulsion Forces** For a typical propulsion source, the propulsion force vector is a function of the velocity magnitude, air density and thrust command ( $T_c$ ). The velocity and air density coupling adds a negligible dynamic effect to the thrust model and can thus be ignored [1]. Due to the band-limited response of the propulsion source to a thrust command, it can be modelled as a low pass filtered thrust vector with an approximated *throttle lag* parameter  $\tau_T$  as follows,

$$\dot{T} = -\frac{1}{\tau_T} T + \frac{1}{\tau_T} T_c \quad (3.16)$$

### 3.4 Aircraft Automatic Flight Control System

Upon analysis of the dynamics equations, it was proven by [1] that the two sets of dynamics can be considered in series. The argument states that the relative motion between the wind and body axes operate at a much higher frequency than the relative motion between the wind and inertial axes. Therefore the coupling between these two sets of dynamics can be removed through the principle of *time scale separation*. The controlled velocity and air density operate at a much longer timescale compared to the rigid body rotational dynamics, allowing the velocity and air density to be considered as parameters. The gravitational coupling through the flight path angle in Equation (3.8) can be removed by designing a dynamic inversion control law.

This allows the design of dynamically invariant controllers, which regulates the specific accelerations within what is known as the *inner loop*. This in turn allows the design of attitude independent guidance controllers, which operate via the inner loop controller within what is known as the *outer loop*. A high-level overview of the flight control structure is presented in Figure 3.6 below.

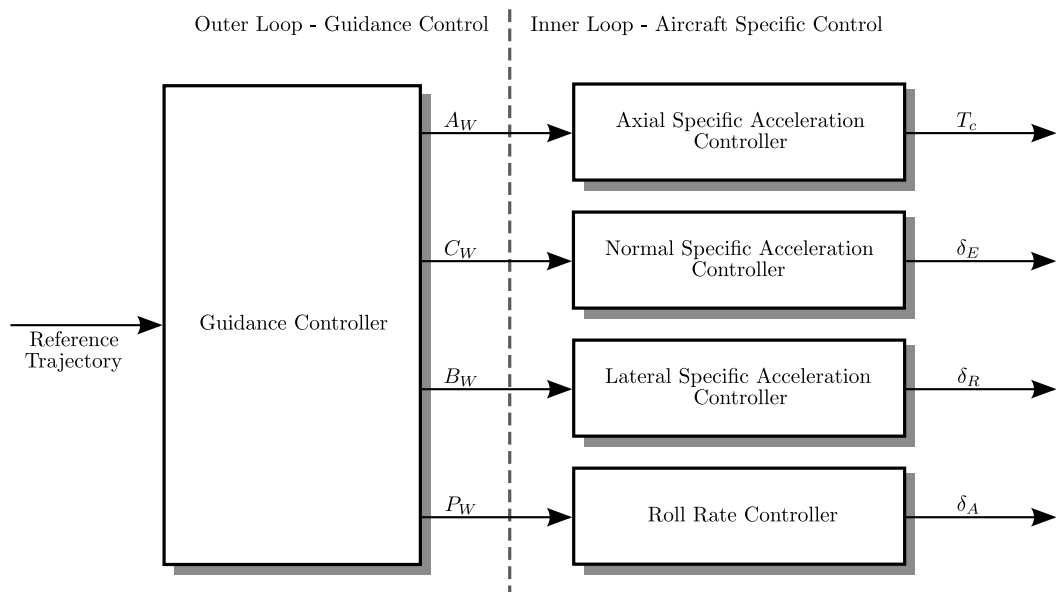


**Figure 3.6:** Autopilot control system architectural layout

#### 3.4.1 Linear Decoupled Longitudinal Dynamics

The nonlinear rigid body rotational dynamics of the innerloop are linearised and decoupled to yield three separated models. These linear decoupled dynamic models include the *axial*, *normal* and *lateral* dynamic equations. These individual models are well suited for designing innerloop controllers to regulate the specific accelerations

and roll rate signals using simple closed form pole placement type control laws. For the longitudinal model these linear decoupled rigid body rotational dynamics are,

Axial:

$$\dot{T} = -\frac{1}{\tau_T}T + \frac{1}{\tau_T}T_c \quad (3.17)$$

$$A_W = \frac{1}{m}T - \frac{\mathbf{q}S}{m}C_D \quad (3.18)$$

Normal:

$$\begin{bmatrix} \dot{\alpha} \\ \dot{Q} \end{bmatrix} = \begin{bmatrix} -\frac{L_\alpha}{mV} & 1 - \frac{L_Q}{mV} \\ \frac{M_\alpha}{I_{yy}} & \frac{M_Q}{I_{yy}} \end{bmatrix} \begin{bmatrix} \alpha \\ Q \end{bmatrix} + \begin{bmatrix} -\frac{L_{\delta_E}}{mV} \\ \frac{M_{\delta_E}}{I_{yy}} \end{bmatrix} \delta_E + \begin{bmatrix} -\frac{L_0}{mV} \\ \frac{M_0}{I_{yy}} \end{bmatrix} + \begin{bmatrix} \frac{g}{V} \\ 0 \end{bmatrix} e_{33}^{WI} \quad (3.19)$$

$$C_W = \begin{bmatrix} -\frac{L_\alpha}{m} & -\frac{L_Q}{m} \end{bmatrix} \begin{bmatrix} \alpha \\ Q \end{bmatrix} - \frac{L_{\delta_E}}{m} \delta_E - \frac{L_0}{m} \quad (3.20)$$

where all the terms in the system matrices are considered parameters to the respective models, as argued by the *time scale separation* principle. In addition, the decoupling of the gravitational acceleration through the flight path angle ( $e_{33}^{WI}$ )<sup>3</sup>, is achieved by the design of a dynamic inversion control law. The dimensional notation used to simplify the expressions of the non-dimensional stability and control derivatives are as follows,

for the force derivatives,

$$\mathcal{F}_x = \mathbf{q}S n C_{\mathcal{F}_x}$$

for the moment derivatives,

$$\mathcal{M}_x = \mathbf{q}S \ell n C_{\mathcal{M}_x}$$

where  $\ell$  is the reference length of the associated moment, which for the pitching moment is the *mean aerodynamic chord* ( $\bar{c}$ ). The parameter  $n$  is the appropriate normalising coefficient of  $x$ , which for the incidence angles and control deflections is unity while for the pitch rate it is  $\bar{c}/2\bar{V}_a$ .

The focus of this project is to prevent stall from occurring without severely influencing the operating flight envelope of the aircraft. As discussed in Chapter 2, the first step in the procedure of preventing an approaching stall from fully manifesting, is to lower the pitch attitude of the aircraft. Therefore, for this research project, the focus will be to prevent stall by interfacing with the aircraft's normal dynamics, ergo controlling the elevator actuator command signal.

<sup>3</sup>The term  $e_{33}^{WI}$  describes an element in the direction cosine matrix, which transforms the inertial axis system to the wind axis system. For longitudinal motion, this term reduces to  $\cos \theta_W$ .

The stall prevention control system will therefore be required to interface with the existing normal specific acceleration controller, without disrupting the flight control system during normal operating flight.

### 3.4.2 Normal Specific Acceleration Controller

The normal dynamics model presented here can be considered as an approximation of the aircraft's standard *short period* mode of motion [17]. Thus, the normal dynamics can be thought of as the short period mode dynamics. Deriving the aircraft's normal dynamics in this manner (as developed in [1]), illustrates the gross attitude independence of this mode of motion. The gravitational coupling term simply acts as a bias input to the normal dynamics. Therefore during level, inverted or steep climbing flight conditions, the short period mode motion of the aircraft with respect to the wind axes remains unchanged and biased only through the gravitational term.

The output feedback control law makes use of pitch rate feedback and an additional integrator state to yield enough degrees of freedom to allow for full pole placement design. The added integrator state will ensure that the normal specific acceleration is tracked with zero steady state error and will eliminate any model uncertainties. In order for the controller to be able to track the commanded reference normal specific acceleration ( $C_{WR}$ ), a feed-forward term has been added to the control law. The feedback control law is defined as,

$$\delta_E = -K_Q Q - K_C C_W - K_E E_C + \bar{N}_C C_{WR} + \delta_{E_{di}} \quad (3.21)$$

where,

$$\dot{E}_C = C_W - C_{WR} \quad (3.22)$$

with the dynamic inversion term, that will cancel the effect of the gravity coupling, denoted by  $\delta_{E_{di}}$ . The feed-forward gain  $\bar{N}_C$  places a finite LHP zero in the system and is defined as,

$$\bar{N}_C = -\frac{K_E}{z_N} \quad (3.23)$$

where  $z_N$  is the location of the zero in the *s-plane*.

The block diagram representation of the normal specific acceleration control system are as follows,

The control gains can thus be solved by comparing coefficients which yields the fol-

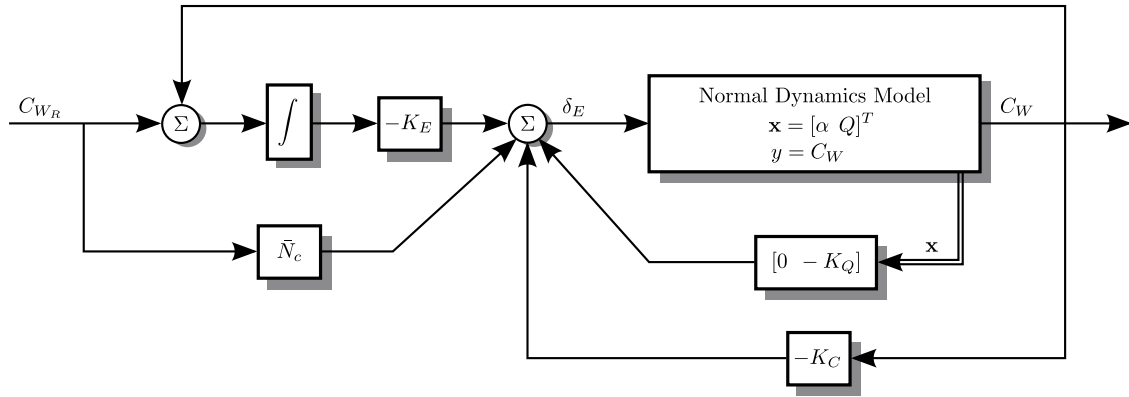


**Figure 3.7:** Normal specific acceleration control system architecture

lowing expressions for the control gains as derived by [1],

$$K_Q = \frac{I_{yy}}{M_{\delta_E}} \left( \gamma_2 + \frac{M_Q}{I_{yy}} - \frac{L_\alpha}{m\bar{V}} \right) \quad (3.24)$$

$$K_C = -\frac{mI_{yy}}{L_\alpha M_{\delta_E}} \left( \gamma_1 + \frac{M_\alpha}{I_{yy}} - \frac{L_\alpha}{m\bar{V}} \left( \gamma_2 - \frac{L_\alpha}{m\bar{V}} \right) \right) \quad (3.25)$$

$$K_E = -\frac{mI_{yy}}{L_\alpha M_{\delta_E}} \gamma_0 \quad (3.26)$$

which leads to the dynamic inversion control law to be defined as,

$$\delta_{E_{di}} = \frac{gI_{yy}}{M_{\delta_E}\bar{V}} \left( \left( \frac{L_\alpha}{m\bar{V}} - \gamma_2 \right) e_{33}^{WI} + \left( \frac{C_W + e_{33}^{WI}g}{\bar{V}} \right) e_{13}^{WI} + P_W e_{23}^{WI} \right) \quad (3.27)$$

The normal specific acceleration controller utilises the aircraft's elevator control surface in order to induce a commanded normal specific acceleration requested by the outerloop guidance controller. The design is based on the method of *pole placement* to ensure stability, performance and invariant dynamic response of the closed loop system. The control design also attempts to eliminate the effect of the gravitational bias through dynamic inversion.



## 3.5 Stall Prevention Control Augmentation Strategy

The purpose of the stall prevention control system will be to limit and prevent the angle of attack from exceeding the critical angle  $\alpha_{crt}$ . Since the angle of attack forms part of the state vector in the decoupled linear normal dynamics model, this control problem involves *state saturation* [18]. By saturating the angle of attack at a predefined limit, the achievable angle of attack range will be constrained. An appropriate choice for this limit angle  $\alpha_{lim}$  is the maximum angle of attack<sup>4</sup> within the linear lift region on the lift-curve, which is assumed to be  $10^\circ$  based on the numerical analysis in §3.2. This will ensure two desirable outcomes namely, the aerial vehicle is prevented from entering the nonlinear lift region and the small incidence angle assumptions made during the development of the aircraft model are kept valid. This simplifies the development of any additional flight control systems significantly.

### 3.5.1 Angle of Attack State Saturation

To constrain the angle of attack state, the elevator control input signal needs to be dynamically limited to ensure the correct response at the angle of attack limit angle. By doing so the elevator actuator will effectively be saturated prematurely, as viewed by the normal specific acceleration control system. If not addressed, this could lead to *windup* issues within the flight control system. Windup occurs when the integrator in the control law continues to integrate due to the error signal between the desired and achievable signal. The integrator state can therefore reach unacceptably high values which will result in a unwanted transient response when this accumulated energy is released. Control systems usually handle this important problem by adding *anti-windup* mechanisms to the compensator design.

Assuming that the angle of attack signal can be measured, the control strategy developed to constrain the angle of attack state is based on the switching between two controllers. One of the controllers is the standard normal specific acceleration controller (prime controller) aimed at providing the reference normal specific acceleration requested by the guidance controller. The secondary controller's task is to keep the angle of attack within the predefined bounds. This is achieved by the secondary feedback loop aimed at regulating the angle of attack using a fixed set-point, which is described by the predefined limit angle. The conceptual architectural layout of the augmented normal dynamics controller is presented as a block diagram in Figure 3.8.

The block denoted by  $W_{stall}$  is the *decision* block, which is responsible for the switching strategy that determines when each of the two respective control laws should

---

<sup>4</sup>It is assumed here that the aircraft will stall at a positive angle of attack. However, the augmentation strategy also accommodates for negative stall, ergo a minimum angle of attack.

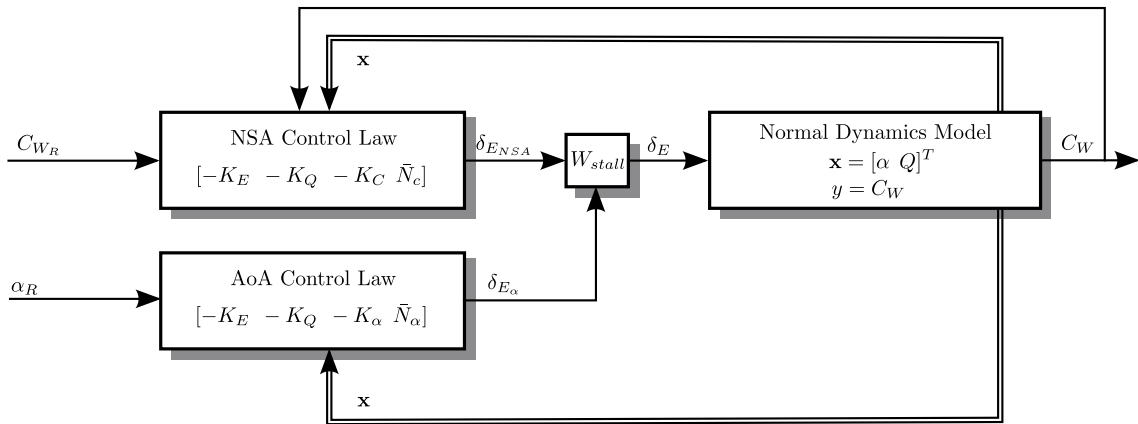


**Figure 3.8:** Switching strategy for angle of attack state saturation

command the elevator input signal. The additional angle of attack control law is based on the same pole placement design methodology used for the normal specific acceleration controller presented previously. However, instead of regulating the normal specific acceleration towards the reference  $C_{WR}$ , the AoA control law regulates the angle of attack state towards the predefined limit.

Since at any given time one of the controllers will be working in open loop and the other in closed loop, there is a strong potential for windup. Therefore both control laws will require some form of anti windup protection.

### 3.5.2 Switching Strategy

The switching operates according to a *stall detection principle* (SDP). This SDP is incorporated into an algorithm that continuously monitors the normal dynamics states and predicts when the angle of attack will exceed its predefined limit, by using model based forward propagation.

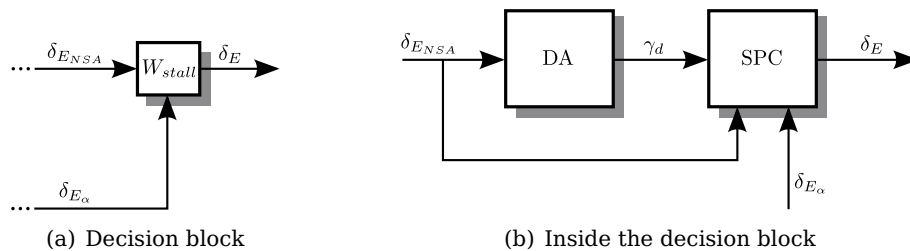


**Figure 3.9:** Decision block responsible for the controller switching

This creates a *detection buffer* (DB), providing the *stall prevention control system* (SPC) with enough time to respond and effectively limit the angle of attack. Taking

a closer look at the inner architecture of the decision block, displayed in Figure 3.9, this *detection algorithm* (DA) forms the first level in the stall prevention control strategy. It is responsible for activating the stall prevention control system through the enabling signal denoted by  $\gamma_d$ , which is defined as,

$$\gamma_d \triangleq \begin{cases} +1 & \text{positive stall detected, activate SPC} \\ 0 & \text{no stall detected, continue normal operation (SPC off)} \\ -1 & \text{negative stall detected, activate SPC} \end{cases} \quad (3.28)$$

During normal operation ( $\gamma_d = 0$ ), the prime controller is connected in closed loop and the secondary controller is completely turned off, whilst the DA continues to monitor the normal dynamics states.

Once the DA has triggered ( $\gamma_d = \pm 1$ ), the stall prevention controller is immediately initialised and connected in closed loop, thus overriding the elevator command provided by the prime controller. A flag is then triggered which enables the anti-windup mechanism of the prime controller, allowing it to remain active whilst operating in open loop. The prime controller is required to remain active to allow the DA to determine when it is safe to deactivate the stall prevention control system. This will be determined from the elevator command signal calculated by the NSA control law.

By constraining the angle of attack, the achievable normal specific acceleration will also be limited. This will cause windup in the climb rate controller within the outer-loop guidance control system. Therefore a flag should also be triggered within the outerloop, which enables the anti-windup mechanisms of controllers dependant on the commanded normal specific acceleration.

### 3.5.3 Stall Prevention Control

The stall prevention control system forms the second level of the stall prevention control strategy and is responsible for applying the correct command to the elevator input signal, to ensure that the angle of attack is never allowed to exceed the predefined limit angle.

Based on the value of  $\gamma_d$  provided by the DA, the SPC determines which control law will drive the aircraft's normal dynamics. In addition to having all the available elevator control laws provided as input, the SPC internally contains two stages of control, which operate in series and function as a finite state machine. These two control stages are,

- Recursive model predictive slew rate control

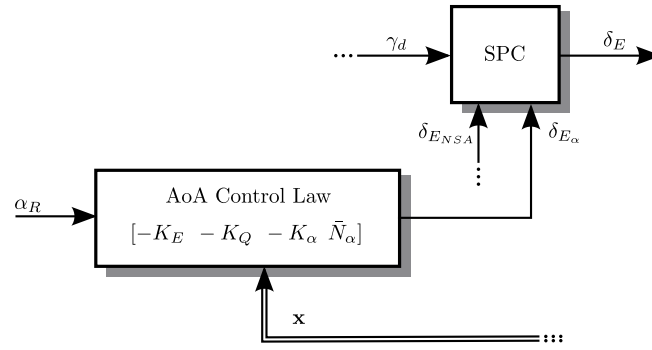


**Figure 3.10:** Stall prevention control blocks responsible of the elevator command signal

- Angle of attack regulating control (described by the AoA control law)

At the onset of detection ( $\gamma_d = \pm 1$ ), the slew rate control stage is the first to act within the SPC. Its purpose is to optimally guide the angle of attack towards the limit angle. This will ensure that operating flight is not abruptly altered or severely restricted. Once the angle of attack reaches a certain threshold value  $\alpha_h$ , which is defined as,

$$\alpha_h < \alpha_{lim} < \alpha_{crt} \quad (3.29)$$

the next control stage is triggered. In addition, the slew rate control stage provides the next control stage (AoA regulating control) with desirable initial state values. The sole purpose of the AoA regulating control stage is to regulate the angle of attack towards the predefined limit angle. As previously mentioned, this second stage of the SPC is based on the same pole placement control design method used for the NSA controller.

At any point during the operation of the SPC, if the detection enabling signal returns to zero ( $\gamma_d = 0$ ), the SPC will be deactivated. At this moment the NSA controller will be reinitialised and reconnected in closed loop, all anti-windup flags will be reset and normal operating flight will resume.

This two stage method of control allows for the design of simpler control system, thus avoiding the complexity of a full model predictive control approach. The reason behind this method of constraining the angle of attack will become clear during the development of the stall prevention control strategy in the following chapters.

### 3.6 Summary

In this chapter the aircraft model and existing flight control system has been presented, with the emphasis on the longitudinal dynamics equations. Within the longitudinal dynamics, the aircraft's normal dynamics is the prime focus of the stall prevention control strategy.

The stall prevention control system will operate at the innerloop control level and is required to interface with the existing normal specific acceleration controller. The following chapters will develop the different components of this stall prevention control strategy as categorised below.

- Chapter 4 will introduce and develop preliminary concepts and mathematical methodology that will define the stall detection principle.
- Chapter 5 will apply these preliminary methodology to actively prevent stall from occurring by designing the first SPC control stage, therefore recursive model predictive slew rate control.
- Chapter 6 will develop and design the second SPC control stage, the AoA regulating controller, which will regulate the angle of attack to the predefined limit angle.
- Chapter 7 will conduct simulations of the fully assembled stall prevention control strategy and analyse its sensitivity to model uncertainties.

## Chapter 4

# Preliminary Methodology

This chapter presents the concepts and mathematical tools which lead to the reasoning behind the principle that defines stall detection. The stall detection principle is based on the linear decoupled normal dynamics described in the previous chapter. However, the concepts behind the stall detection principle are not limited to linear dynamics, since the analysis methodology also accommodates nonlinear dynamics. By incorporating this stall detection principle into the stall prevention control strategy, an algorithm can be developed to determine when the SPC should override the elevator signal of the NSA controller.

### 4.1 Conceptual Phase Plane Approach

The second order model of the linear decoupled normal dynamics, has a state vector containing the angle of attack  $\alpha$  and the pitch rate of the body axes  $Q$ . The input to this SISO (single input single output) system is the elevator deflection variable. Therefore, the elevator can be considered as the force that drives the states through *state space*. For a two-dimensional model, such as the normal dynamics system, the evolution of the state vector  $[\alpha, Q]^T$  can be visualised in what is known as a *phase plane*. At any given time  $t_0$ , the state vector can be represented by a point in this phase plane, as depicted in Figure 4.1.

From a starting point  $(\alpha(t_0), Q(t_0))$ , the system will move in a time  $\Delta t$  to a new state  $(\alpha(t_0 + \Delta t), Q(t_0 + \Delta t))$ , which can only be determined by integrating the ODE (ordinary differential equations) that govern the normal dynamics. A sequence of state points through which the system passes as it evolves, will form a continuous curve known as a *trajectory* or *orbit*.

The ODE also gives the magnitude and direction of change of the state variables at any point in the phase plane. By applying this *velocity vector*  $\mathbf{v} = [\dot{\alpha}, \dot{Q}]^T$  to every point in the phase plane, a *vector field* is created, which indicates all possible

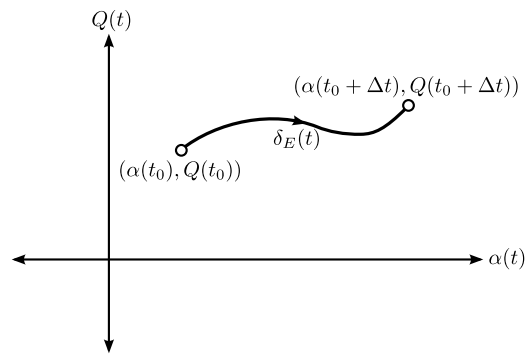


**Figure 4.1:** A 2D visualisation of phase space

state trajectories corresponding to the normal dynamics, known as the *flow* of the dynamical system. If the normal dynamics are stable, thus short period mode poles in the LHP, this vector field will have an *equilibrium point*. At this point the velocity vector  $\mathbf{v}$  will vanish and the system can be described as being at rest. This equilibrium point coincides with the aircraft's trimmed flight condition. For straight and level flight this is defined for a certain velocity and altitude at a particular angle of attack and elevator deflection at zero pitch rate. Consider the visual representation in Figure 4.2.

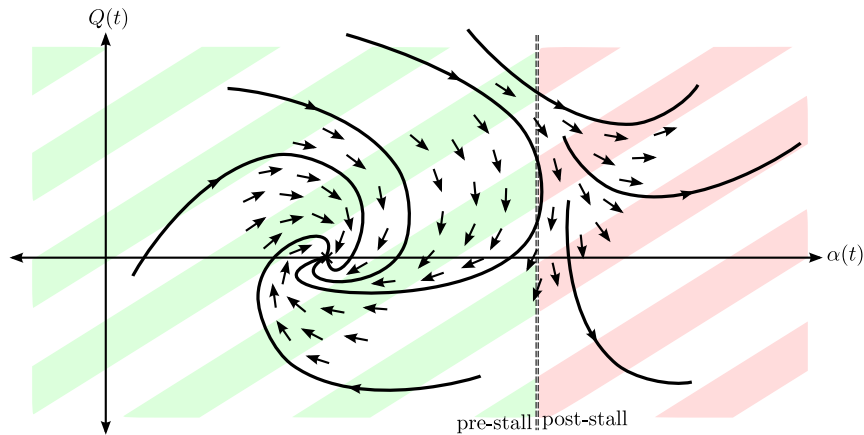


**Figure 4.2:** Visualisation of the flow in the phase plane

The angle of attack at which the maximum lift coefficient is achieved, creates a vertical separation in the phase plane. During pre-stall flight the normal dynamics are stable and the vector field exhibits the behaviour of a *stable focus*. After stall has occurred, the linear decoupled normal dynamics model is no longer valid and a non-linear model of the normal dynamics needs to be considered<sup>1</sup>. As a result of the

<sup>1</sup>This nonlinear model will contain all the nonlinear stability and control derivatives in order to model true aircraft behaviour after stall has occurred.

aerodynamic derivative becoming nonlinear at the stall angle of attack  $\alpha_{crt}$ , the vector field diverges and becomes unstable in this post-stall region. Therefore, it may or may not be possible for a particular aircraft to regain stability and recover from stall. Depending on the aerodynamic properties of the particular aircraft, this post-stall region could be identified at many different locations in the phase plane. The focus of the SPC will therefore still be to constrain the dynamics to the linear pre-stall region to allow the linear dynamics to remain valid.

#### 4.1.1 Phase Plane State Trajectories

In the existing flight control system, the NSA controller is responsible for providing the elevator input command based on the reference normal specific acceleration required by the guidance system. Consider the following visualisation of possible state trajectories,

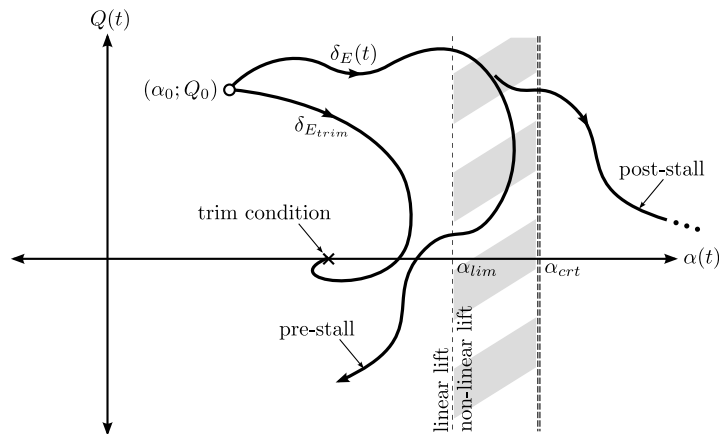


**Figure 4.3:** Visualisation of possible state trajectories in the phase plane

For a given starting point in the pre-stall region of the phase plane, there are two types of possible forced trajectories that could occur. These include trajectories which never exceed the critical angle of attack  $\alpha_{crt}$  and trajectories that do. For the latter state trajectory, without any proper intervention, the aircraft would certainly stall. This will render the linear mathematical aircraft model inaccurate and therefore the flight control system will be unable to respond in a desirable manner.

A special form of these trajectories occur when the elevator is held constant at its trim deflection angle, as depicted in Figure 4.3. This unforced state trajectory will naturally return to the equilibrium point, assuming the trajectory does not exceed the critical angle of attack. This state trajectory is of particular interest and will be the primary focus in this chapter to introduce the concepts of predicting the behaviour of a state trajectory.



### 4.1.2 Description of Stall Prevention Control

With the equilibrium point known, the aim now is to evaluate the dynamics from any point in the phase plane. The focus of the stall detection algorithm is to be able to predict, given any current point, where in the phase plane the state vector will move next. The stall detection algorithm therefore utilises the ODE from the linear normal dynamics model, to propagate the state vector forward in time, thus predicting the behaviour of a state trajectory from a particular point in the phase plane. Then, by analysing the maximum angle of attack achieved during this trajectory, the stall detection principle determines if the stall prevention control system should be activated.

**Definition.** *The stall detection principle states that, if the peak angle of attack of a predicted state trajectory  $\alpha_P$  is greater than the predefined angle of attack limit  $\alpha_{lim}$ , then the SPC should dynamically limit the elevator input signal. If  $\alpha_P$  is not greater than  $\alpha_{lim}$ , normal flight operation will not be interfered with and the stall detection algorithm will continue to monitor the state vector.*

Therefore, with the proper intervention provided to the elevator command by the SPC, the state trajectories in the phase plane will be constrained to the stable flow region, as displayed in Figure 4.4.

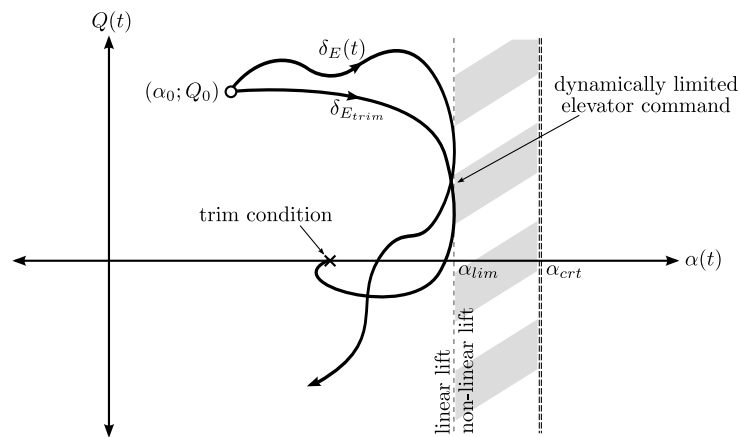


**Figure 4.4:** Visualisation of state trajectories in the phase plane under stall prevention control supervision

As discussed earlier, this will prevent the aircraft from flying in the nonlinear lift region on the lift-curve and in so doing will prevent the aircraft from stalling. In addition, all small angle assumption and simplifications made within the linear aircraft model will remain valid, hence simplifying the design of the flight control system.

The state trajectory forward prediction concept will now be mathematically derived to yield the algebraic expressions required to propagate the state vector forward in time.

## 4.2 Forward State Propagation

This forward propagation is accomplished by solving the *state transition equation* for the normal dynamics. The state transition equation derives algebraic expressions for each of the state variables which describes their movement through state space as a function of time, or equivalently for this second order system, through the phase plane.

The linear normal dynamics model presented in Equation (3.19), are restated below for convenience.

$$\begin{bmatrix} \dot{\alpha} \\ \dot{Q} \end{bmatrix} = \begin{bmatrix} -\frac{L_{\alpha}}{mV} & 1 - \frac{L_Q}{mV} \\ \frac{M_{\alpha}}{I_{yy}} & \frac{M_Q}{I_{yy}} \end{bmatrix} \begin{bmatrix} \alpha \\ Q \end{bmatrix} + \begin{bmatrix} -\frac{L_{\delta_E}}{mV} \\ \frac{M_{\delta_E}}{I_{yy}} \end{bmatrix} \delta_E + \begin{bmatrix} -\frac{L_0}{mV} \\ \frac{M_0}{I_{yy}} \end{bmatrix} + \begin{bmatrix} \frac{g \cos \theta_W}{V} \\ 0 \end{bmatrix} \quad (4.1)$$

where the state vector and input scalar are defined as follows,

$$\mathbf{x}(t) = \begin{bmatrix} \alpha(t) & Q(t) \end{bmatrix}^T \quad u(t) = \delta_E(t)$$

which yields the following simplified state space representation of the dynamics,

$$\dot{\mathbf{x}}(t) = \mathbf{A}\mathbf{x}(t) + \mathbf{B}u(t) + \mathbf{b} \quad (4.2)$$

In essence, this forward state propagation is an initial value problem for a system with linear first order differential equations, with the initial values chosen as the starting point in the phase plane.

Note that the flight path angle couples into the normal dynamics through the gravitational term in Equation (4.1). It has been shown in Appendix A.3 that during forward state propagation this term can be considered a static offset due to its slower time scale, without influencing the part of the trajectory of interest.

### 4.2.1 State Transition Equation

The state transition equation can easily be solved by introducing the Laplace transform [19]. Therefore first solving the state vector in the frequency domain by taking the Laplace transform of the state dynamics in Equation (4.2) and then transforming back to the time domain by taking the inverse Laplace transform of the resulting state

equations. This is shown below,

$$\begin{aligned}
\mathcal{L}[\dot{\mathbf{x}}(t)] &= \mathcal{L}[\mathbf{A}\mathbf{x}(t) + \mathbf{B}u(t) + \mathbf{b}] \\
\therefore s\mathbf{X}(s) - \mathbf{x}^0 &= \mathbf{A}\mathbf{X}(s) + \mathbf{B}U(s) + \frac{\mathbf{b}}{s} \\
\therefore (s\mathbf{I} - \mathbf{A})\mathbf{X}(s) &= \mathbf{x}^0 + \mathbf{B}U(s) + \frac{\mathbf{b}}{s} \\
\therefore \mathbf{X}(s) &= (s\mathbf{I} - \mathbf{A})^{-1}\mathbf{x}^0 + (s\mathbf{I} - \mathbf{A})^{-1}\mathbf{B}U(s) + (s\mathbf{I} - \mathbf{A})^{-1}\frac{\mathbf{b}}{s} \\
\therefore \mathbf{X}(s) &= \underbrace{\Phi(s)\mathbf{x}^0}_{\text{Zero Input Response}} + \underbrace{\Phi(s)\mathbf{B}U(s)}_{\text{Zero State Response}} + \underbrace{\Phi(s)\mathbf{b}s^{-1}}_{\text{Static Contribution}} \quad (4.3)
\end{aligned}$$

with  $\mathbf{I}$  an  $n \times n$  identity matrix<sup>2</sup>,  $s$  the frequency domain operator and  $\Phi(s)$  the resolvent of  $\mathbf{A}$  defined as,

$$\Phi(s) = (s\mathbf{I} - \mathbf{A})^{-1} \quad (4.4)$$

Taking the inverse Laplace transform of Equation (4.3) gives,

$$\mathcal{L}^{-1}[\mathbf{X}(s)] = \mathbf{x}(t) \quad (4.5)$$

where  $\mathbf{x}^0$  should reflect the static offset introduced by the nonzero trim condition of the aircraft, therefore the initial state vector is defined by  $\mathbf{x}(t_0)$ , where  $\mathbf{x}^0$  is expressed as follows,

$$\mathbf{x}(t_0) \triangleq \mathbf{x}^0 + \mathbf{x}_{trim}; \quad \mathbf{x}^0 = \Delta\mathbf{x} \quad (4.6)$$

with  $\Delta\mathbf{x}$  the offset from the equilibrium point (trim condition) and  $\mathbf{x}_{trim}$  the trim values of the states at a particular trim velocity when the vehicle is flying straight and level. Note that during straight and level flight  $\Delta\mathbf{x} = 0$  and the dynamic system is at rest. The same analogy therefore applies to the input  $U(s)$ . When the elevator is deflected from its trim angle  $\delta_{E_{trim}}$ , in the time domain the input is the offset angle  $\Delta\delta_E(t)$  defined as,

$$\delta_E(t) = \Delta\delta_E(t) + \delta_{E_{trim}} \quad (4.7)$$

therefore when the elevator is at its trim deflection angle, the input  $U(s)$  is zero. This interpretation of the state transition equation will calculate the state trajectories of the linear normal dynamics model exactly, as will be shown through simulation.

By solving the algebraic expressions for the state variables from Equation (4.3), the state trajectory at any point in the phase plane can be calculated.

<sup>2</sup>The integer  $n$  is the order of the state space system, thus  $n = 2$  for this system.

Recall the special trajectory from the previous section, where the elevator was held constant at its trim deflection angle. From Equation (4.3), this state trajectory describes the *zero input response* of the normal dynamics and will now be investigated further.

### 4.3 Zero Input Response

The simplest form of the general differential equation presented in Equation (4.2) is called the *homogeneous state equation*. It describes the unforced response of the system and has the following form,

$$\dot{\mathbf{x}}(t) = \mathbf{A}\mathbf{x}(t) + \mathbf{b}; \quad \mathbf{x}(t_0) \triangleq \Delta\mathbf{x} + \mathbf{x}_{trim}$$

If the initial time  $t_0 = 0$  and the initial state values are known at  $t = 0$ , the solution to the homogeneous state equation can be derived from Equation (4.3) by setting  $U(s) = 0$  and taking the inverse Laplace transform to give<sup>3</sup>,

$$\mathbf{x}(t) = \phi(t)\Delta\mathbf{x} + \mathbf{x}_{trim} \quad (4.8)$$

with the *state transition matrix* defined as,

$$\phi(t) = e^{\mathbf{A}t} \quad (4.9)$$

The state transition matrix of the system can be derived from the frequency domain by inverse Laplace transforming the resolvent of  $\mathbf{A}$ ,

$$\phi(t) = \mathcal{L}^{-1}[\Phi(s)] = e^{\mathbf{A}t} \quad (4.10)$$

Therefore to solve the state transition equation for the homogeneous case, it is required to know the trim values of the states and also the state transition matrix of the system. It will then be possible to calculate the zero input state trajectory from any point in the phase plane.

During symmetric level flight, the lateral forces and moments are in equilibrium and the trim condition is therefore defined by the angle of attack, elevator angle, thrust, pitch attitude and flight path angle. In Appendix A.1 it is shown how the trim angle of attack and elevator deflection can be derived using a simplified force and moment

---

<sup>3</sup>The static contribution from the gravitational term has been ignored in Equation (4.8) for the purpose of clarity and will be addressed in the following chapter.

model to yield the following expression,

$$\begin{bmatrix} \alpha_{trim} \\ \delta_{E_{trim}} \end{bmatrix} = \begin{bmatrix} C_{m\alpha} & C_{m\delta_E} \\ C_{L\alpha} & C_{L\delta_E} \end{bmatrix}^{-1} \begin{bmatrix} -C_{m_0} \\ \frac{mg}{qS} - C_{L_0} \end{bmatrix} \quad (4.11)$$

### 4.3.1 State Transition Matrix

The state transition matrix defines the transition in state as a rational function of time carried out by the matrix exponential  $e^{\mathbf{A}t}$  and denoted  $\phi(t)$ . Recalling that the inverse Laplace transform of the resolvent of  $\mathbf{A}$  is equal to the matrix exponential, consider the following derivations.

$$\Phi(s) = \frac{\text{Adj}(s\mathbf{I} - \mathbf{A})}{\det(s\mathbf{I} - \mathbf{A})} = \frac{1}{\lambda(s)} \text{Adj}(s\mathbf{I} - \mathbf{A}) \quad (4.12)$$

Where the determinant is a second order polynomial in  $s$  denoted  $\lambda(s)$  known as the *characteristic equation* of  $\mathbf{A}$ . The roots of this polynomial gives the *eigenvalues* of the  $\mathbf{A}$  matrix which are equivalent to the pole location of the system. The poles will be located in the *s-plane* at,

$$\lambda_{1,2} = -\sigma \pm j\omega_d \quad (4.13)$$

with  $\sigma^{-1}$  the time constant and  $\omega_d$  the undamped natural frequency. This complex conjugate pole pair describes the short period mode motion of the vehicle. For a stable system, these poles need to be located in the LHP.

To solve for the state transition matrix in a general symbolic approach, the adjoint of the matrix  $(s\mathbf{I} - \mathbf{A})$  becomes,

$$\text{Adj}(s\mathbf{I} - \mathbf{A}) = \begin{bmatrix} s - a_{22} & a_{12} \\ a_{21} & s - a_{11} \end{bmatrix}$$

with the resolvent of  $\mathbf{A}$  described as,

$$\Phi(s) = \frac{1}{\lambda(s)} \begin{bmatrix} s - a_{22} & a_{12} \\ a_{21} & s - a_{11} \end{bmatrix} \quad (4.14)$$

where  $a_{jk}$  represents a element in the  $\mathbf{A}$  matrix, with  $j$  the row and  $k$  the column index value respectively.

By taking the inverse Laplace transform of Equation (4.14), the following expression for the state transition matrix is obtained.

$$e^{\mathbf{A}t} = \begin{bmatrix} e^{-\sigma t} \cos \omega_d t + \frac{(-a_{22}-\sigma)}{\omega_d} e^{-\sigma t} \sin \omega_d t & \frac{(a_{12})}{\omega_d} e^{-\sigma t} \sin \omega_d t \\ \frac{(a_{21})}{\omega_d} e^{-\sigma t} \sin \omega_d t & e^{-\sigma t} \cos \omega_d t + \frac{(-a_{11}-\sigma)}{\omega_d} e^{-\sigma t} \sin \omega_d t \end{bmatrix} \quad (4.15)$$

The expressions inside the state transition matrix describe a particular type of function known as an exponentially modulated sinusoid, which in general form is expressed as,

$$a_1 e^{-\sigma t} \cos(\omega_d t) + a_2 e^{-\sigma t} \sin(\omega_d t) = A e^{-\sigma t} \sin(\omega_d t + \varphi) \quad (4.16)$$

with,

$$A = \pm \sqrt{(a_1)^2 + (a_2)^2} \quad (4.17)$$

$$\varphi = \tan^{-1} \left( \frac{a_1}{a_2} \right) \quad (4.18)$$

where the sign of the magnitude  $A$  is dependant on the sign of the magnitude of the sine term  $a_2$  in the following relationship,

$$a_2 \geq 0 \leftrightarrow A \geq 0 \quad (4.19)$$

$$a_2 < 0 \leftrightarrow A < 0 \quad (4.20)$$

This type of function is periodic and consists of a sine wave with frequency  $\omega_d$  and amplitude  $A e^{-\sigma t}$ . The behaviour of this function is therefore closely related to the location of the short period mode poles in the  $s$ -plane. When the system is stable (LHP poles) the function would exponentially decay towards zero over time, as presented in Figure 4.5 displaying important properties related to this type of function. If the system is unstable (RHP poles) this function will grow exponentially.

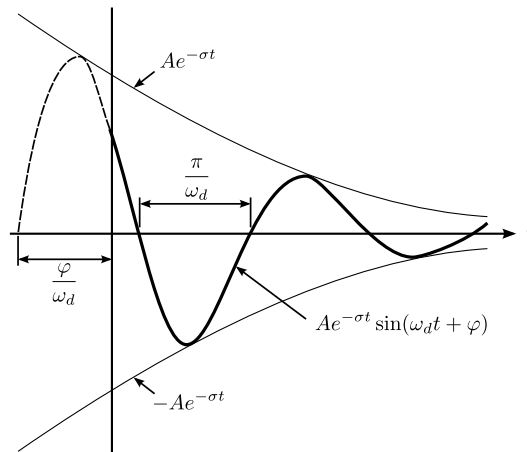


**Figure 4.5:** Sketch of an exponentially modulated sinusoid

The state trim values will simply provide an offset to the function, therefore shifting it vertically along the magnitude axis.

With the trim expressions and state transition matrix derived, the zero input state trajectory can be calculated for any point in the phase plane, through the homogeneous state equation described by Equation (4.8).

### 4.3.2 Zero Input State Trajectory

The state equations for the angle of attack and pitch rate are derived by substituting Equation (4.15) into the homogeneous state equation (4.8) to give the following expressions for the zero input response of the system states.

$$\begin{bmatrix} \alpha(t) \\ Q(t) \end{bmatrix}_{ZI} = \begin{bmatrix} \Delta\alpha \\ \Delta Q \end{bmatrix} \begin{bmatrix} \frac{\Delta\alpha(-a_{22}-\sigma)+\Delta Q(a_{12})}{\omega_d} \\ \frac{\Delta\alpha(a_{21})+\Delta Q(-a_{11}-\sigma)}{\omega_d} \end{bmatrix} \begin{bmatrix} e^{-\sigma t} \cos \omega_d t \\ e^{-\sigma t} \sin \omega_d t \end{bmatrix} + \begin{bmatrix} \alpha_{trim} \\ 0 \end{bmatrix} \quad (4.21)$$

Consider the following analysis of the state equations in the phase plane. Given the trim condition defined in Appendix B.2, a number of initial values were chosen to simulate the trajectories of the system states in the homogeneous case. At this trim velocity and air density the calculated state trim values are,

**Trimmed Flight:** ( $\bar{V} = 22$  m/s,  $\rho = 1.0588$  kg/m<sup>3</sup>)

$\alpha = 2.2458^\circ$ : The angle of attack during straight and level flight

$\delta_E = -3.7108^\circ$ : The elevator deflection angle during straight and level flight

The results of the state trajectories simulated with the linear normal dynamics model are presented in Figure 4.6.

From Figure 4.6 it is clear that the system is stable and that all state trajectories converge to the equilibrium point. To verify the zero input state transition equations derived here, the initial point ( $8^\circ$ ,  $50^\circ/\text{s}$ ) was substituted into Equation (4.21). The calculated state trajectory tracks the simulated trajectory exactly, as shown superimposed in Figure 4.6.

This analysis can be viewed as the simulation of straight and level flight with vertical airflow disturbances (turbulence). The disturbance perturbs the AoA and pitch rate from its trim position. If the elevator is held fixed at its trim deflection angle, the response trajectories describe the natural behaviour of the aircraft to return to its trim condition.

Taking the angle of attack limit ( $\alpha_{lim} = 10^\circ$ ) into consideration, it is important to be able to predict whether or not the resulting natural behaviour of the aircraft will cause it to stall. With reference to the stall detection principle, this could only be determined by predicting the peak angle of attack for the given state trajectory. By

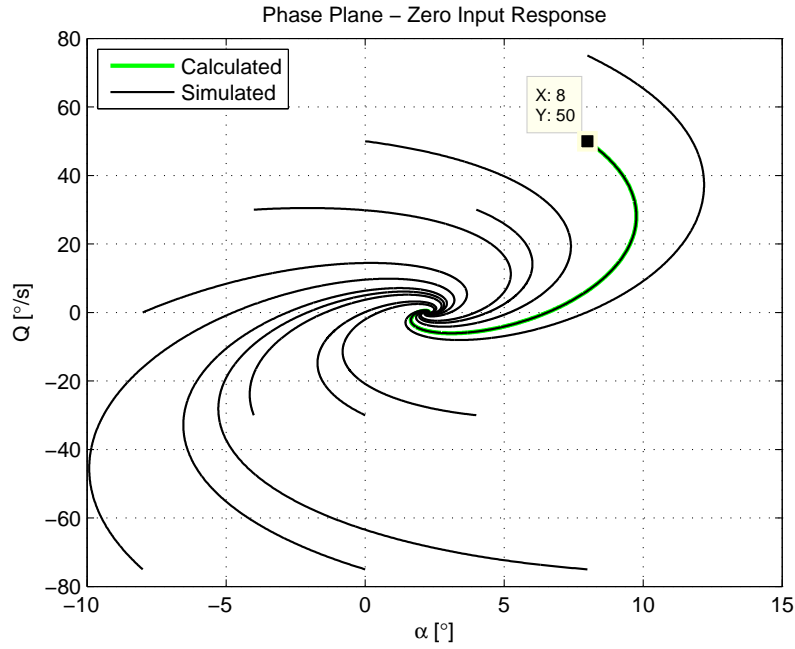


**Figure 4.6:** Phase plane analysis of the zero input state trajectories

mathematically manipulating (4.21), a closed form expression can easily be derived to calculate the peaks of all zero input state trajectories.

Consider the following derivations of this closed form peak angle of attack solution. To simplify the expressions, the angle of attack state transition equation is expressed in a more general form as shown below.

$$\begin{aligned}\alpha_{ZI}(t) &= (\Delta\alpha)e^{-\sigma t} \cos \omega_d t + \left( \frac{\Delta\alpha(-a_{22} - \sigma) + \Delta Q(a_{12})}{\omega_d} \right) e^{-\sigma t} \sin \omega_d t + \alpha_{trim} \\ &= k_c e^{-\sigma t} \cos \omega_d t + k_s e^{-\sigma t} \sin \omega_d t + k\end{aligned}\quad (4.22)$$

Where the subscripts  $c$  and  $s$  represent the cosine and sine constant coefficients respectively. The first time derivative is then given by,

$$\dot{\alpha}_{ZI}(t) = \dot{k}_c e^{-\sigma t} \cos \omega_d t + \dot{k}_s e^{-\sigma t} \sin \omega_d t \quad (4.23)$$

with the constant coefficients defined as,

$$\begin{aligned}\dot{k}_c &= -k_c \sigma + k_s \omega_d \\ \dot{k}_s &= -k_c \omega_d - k_s \sigma\end{aligned}$$

When the angle of attack state trajectory reaches a peak (positive or negative) the time rate of change is equal to zero, thus  $\dot{\alpha}_{ZI}(t) = 0$ . Substituting this into Equation (4.23) and solving for  $t$ , yields the time instances coinciding with the peak occurrences. Since the expression for  $\dot{\alpha}_{ZI}(t)$  describes a exponentially modulated sinusoid



(without a constant offset), these peak time instances will occur periodically. Therefore, Equation (4.23) can be expressed as,

$$\dot{\alpha}_{ZI}(t) = K_s e^{-\sigma t} \sin(\omega_d t + \hat{\phi}) \quad (4.24)$$

where,

$$K_s = \pm \sqrt{(\hat{k}_c)^2 + (\hat{k}_s)^2}$$

$$\hat{\phi} = \tan^{-1} \left( \frac{\hat{k}_c}{\hat{k}_s} \right)$$

Substituting  $\dot{\alpha}_{ZI}(t) = 0$  into Equation (4.24) yields,

$$0 = K_s e^{-\sigma t} \sin(\omega_d t + \hat{\phi})$$

$$\therefore \sin(\omega_d t + \hat{\phi}) = 0$$

$$\therefore t = -\frac{\hat{\phi}}{\omega_d} + \frac{n\pi}{\omega_d} \quad n \in 0, 1, 2, 3, \dots \quad (4.25)$$

By substituting the calculated time instances into Equation (4.22), the magnitudes for all the angle of attack peaks of a given state trajectory can be calculated, provided an initial angle of attack and pitch rate state at a given air speed and altitude.

To verify Equation (4.25), consider the calculated state trajectory displayed in Figure 4.6. The individual angle of attack and pitch rate state trajectories are displayed in Figure 4.7.

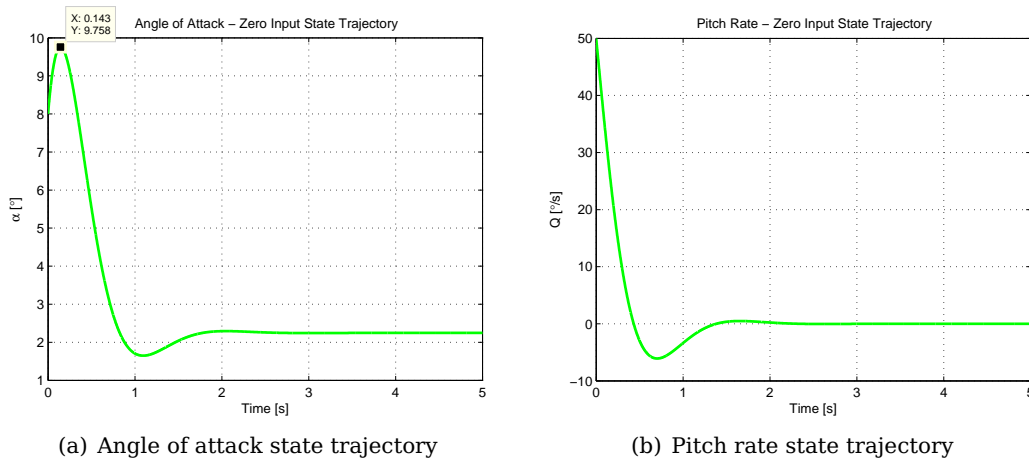


**Figure 4.7:** Zero input state trajectories

The maximum angle of attack peak for this trajectory is calculated to occur at  $t = 0.1433$  s. Substituting this time value into Equation (4.22) yields a maximum angle of

attack peak of  $9.7581^\circ$ , which concurs with the simulated results.

Up until now little has been said about negative stall, with the primary focus involving positive stall. The minimum angle of attack peak can just as easily be calculated using Equation (4.25) and compared to a negative limit angle, to predict negative stall. With this in mind, it is possible to determine all the points in the phase plane that, given a predefined positive and negative angle of attack limit, will result in a state trajectory exceeding either one of the angle of attack limits.

### 4.3.3 Stall Detection Envelope

When the maximum and minimum angle of attack peaks are predicted for the zero input state trajectory at every point in the phase plane, a region is created that represents safe operating flight without the possibility of stall. In this region the natural behaviour of the aircraft would prevent it from exceeding the predefined limit angles. This can be visualised in Figure 4.8.

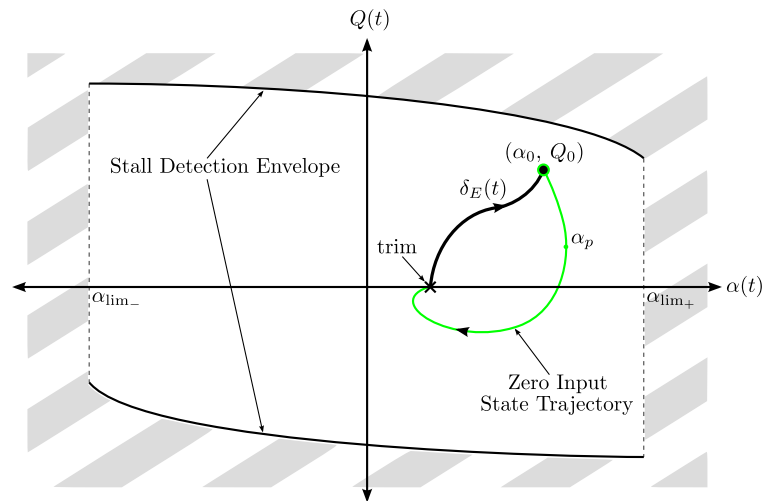


**Figure 4.8:** Stall detection envelope conceptual sketch

Extending the previous simulation to predict the angle of attack peak values for the zero input state trajectories over a sufficiently large region in the phase plane, yields the results presented in Figure 4.9.

For this simulation the negative angle of attack limit was chosen to be  $-10^\circ$ , however either of these limit angles could be chosen as different values. Notice that the chosen initial point of the previous simulation is located inside this region as expected, since the predicted angle of attack peak at this state was  $9.7581^\circ$ .

Notice that for state values with high pitch rates, the resulting zero input state trajectory will cause angle of attack to peak at a value greater than the limit, even if

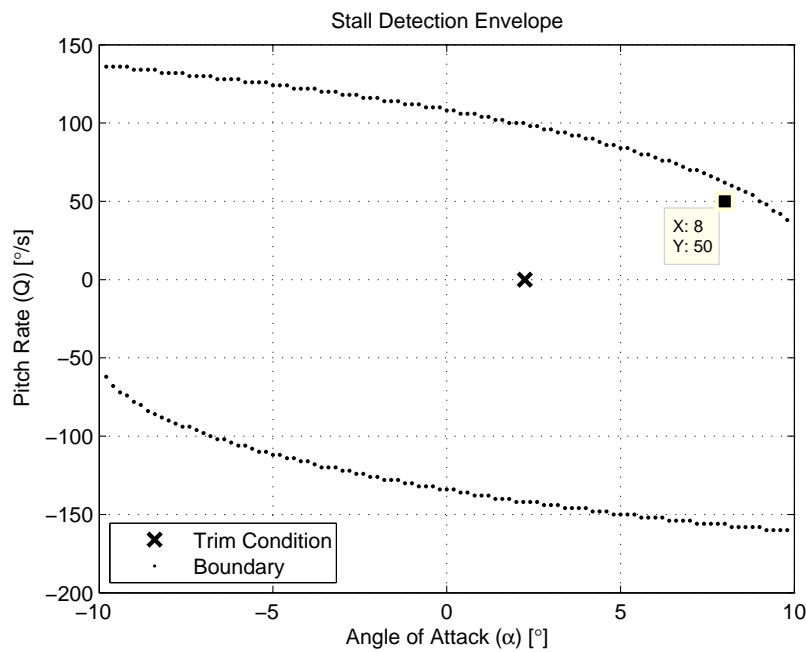


**Figure 4.9:** Stall detection envelope for the zero input state trajectories

the initial angle of attack state value was much less than the limit. This makes sense, since high pitch rate manoeuvres can easily cause the aircraft to stall. In contrast, lower pitch rate manoeuvres could allow the angle of attack to progressively increase towards the limit angle, as presented in Figure 4.9. Therefore there exist state values at low pitch rate where the natural behaviour of the aircraft would return the state to its equilibrium point only once the state reaches the limit angle. This substantiates the choice of the angle of attack limit angle as coinciding with the linear lift region, rather than the actual stall angle of attack.

All the state values located on this envelope, will have zero input state trajectories that peak at the angle of attack limit angles. Where the top and bottom envelope represents the boundary for positive stall detection and negative stall detection respectively<sup>4</sup>.

Furthermore, this stall detection envelope varies with the operating trim condition. Therefore, if the velocity changes, so does the trim angle of attack and elevator deflection to ensure enough lift for straight and level flight. The resulting effect on the stall detection envelope can easily be shown through simulation. The results for the maximum velocity of 30 m/s and the minimum velocity of 17 m/s are presented in Figure 4.10.

From Figure 4.10 it is clear that positive stall can occur more readily during low speed flight, as discussed in Chapter 2.

<sup>4</sup>Note that, what refers to here as stall detection, implies that the peak angle of attack is greater (or in the negative case less) than the predefined limit angle.

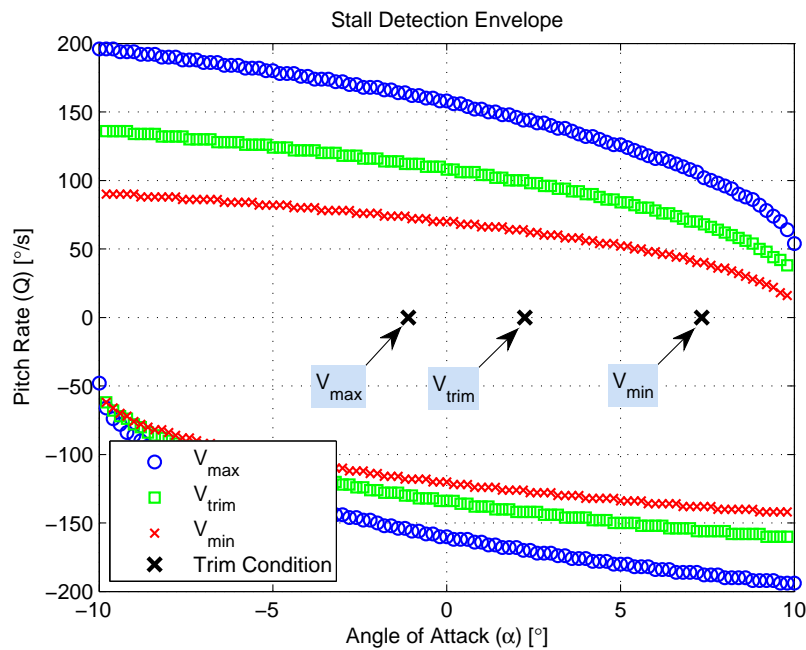


**Figure 4.10:** Effect of variation in air velocity on the stall detection envelope

## 4.4 Summary

This chapter introduced the concept of the phase plane and developed the necessary mathematical tools required to analyse the normal dynamics and predict stall. These concepts and tool are not restricted to linear dynamics model and can be extended to incorporate the aircraft's nonlinear dynamics.

Furthermore, the natural tendency of the aircraft to prevent stall on its own account was investigated. This led to the concept of a bounded region in the phase plane where the aircraft's natural behaviour will prevent it from stalling. This pre-stall region assumes that, if the aircraft is driven to the edge of the stall detection envelope, the elevator actuator can change its current deflection angle to the trim angle at an infinite slew rate in order for the natural behaviour of the aircraft to prevent state trajectory to exceed  $\alpha_{lim}$ . This, however, is not possible for a physical actuator which has slew rate limitations.

Instead of relying on the aircraft's natural behaviour to prevent stall, an appropriate elevator input signal can be designed to actively prevent stall from occurring. This signal can be injected into the state transition equation and used to propagate forward in time, to predict the angle of attack peak as a result of this forced input. By doing this, the SPC will only be activated at the very last possible moment, thus giving maximum freedom of operation to the existing NSA controller. This will be investigated in the following chapter.

## Chapter 5

# Stall Prevention Control

This chapter investigates and designs an elevator command that will allow the aircraft to actively prevent a stall from occurring. Based on the concepts developed in the previous chapter, this input signal can in turn be used to predict an approaching stall through forward state propagation, thus enabling the SPC to respond without influencing normal flight operation.

### 5.1 Active Stall Prevention

With reference to the traditional stall prevention and recovery procedures discussed in Chapter 2, it is clear that the first step to prevent a stall (positive stall in this case) from occurring is to immediately reduce the aircraft's pitch attitude at the first indication of stall. This effectively reduces the angle of attack, allowing the aircraft to regain sufficient lift. This can only be achieved by commanding positive elevator<sup>1</sup> to lower the aircraft's nose.

Therefore a signal that commands positive elevator deflection needs to be designed. By including the nonlinearities of the physical elevator actuator in this design, the resulting stall prevention control system will be able to effectively prevent stall by anticipating these physical actuator limitations. For unmanned aerial vehicles, actuation is achieved through the use of *servo motors*, with typical control surface limitations being fixed maximum slew rate and finite deflection range (saturation constraint).

The elevator signal can therefore be designed to have a form as presented in Figure 5.1, which describes a deflection (in the positive sense) from its current angle  $\delta_{E_0}$  to its maximum limit  $\delta_{E_{max}}$  at a slew rate denoted by  $\mu$ . This elevator command will incorporate all of the above mentioned requirements<sup>2</sup>.

---

<sup>1</sup>For the correct control surface deflection sign conventions, consult Figure 3.2.

<sup>2</sup>To actively prevent negative stall, the elevator will be slewed at a rate  $-\mu$  towards its negative limit  $\delta_{E_{min}}$ .

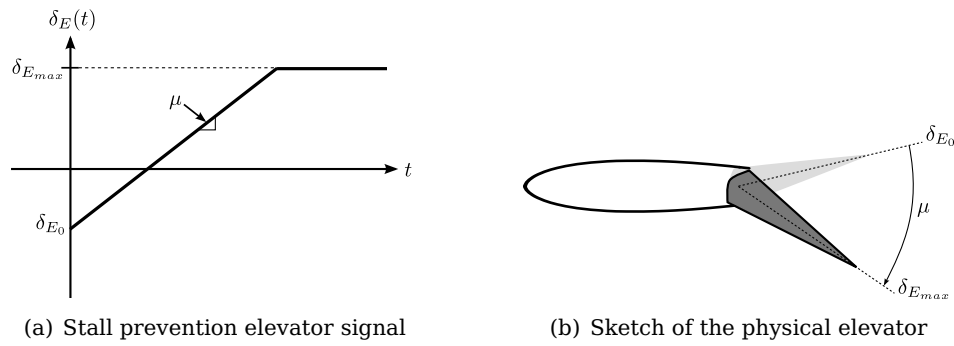


**Figure 5.1:** Graphical representation of active stall prevention elevator command

### 5.1.1 Stall Prevention State Trajectory

By mathematically describing this elevator signal in the frequency domain and injecting it as  $U(s)$  into the state transition equation expressed in Equation (4.3), the state trajectory resulting from this elevator input can be calculated. The calculated state trajectory would therefore represent the evolution of the angle of attack and pitch rate states during a stall prevention manoeuvre. It is therefore possible to predict the peak angles of attack during this manoeuvre, thus enabling the SPC to determine (with regards to the stall detection principle) the very last possible moment at which the elevator would be able to actively prevent the aircraft from stalling.

By propagating forward in time with this elevator input signal for a sufficiently large number of state values in the phase plane and subjecting the predicted angle of attack peak values to the concept of the stall detection envelope, a similar bounded region is created as displayed in Figure 5.2.

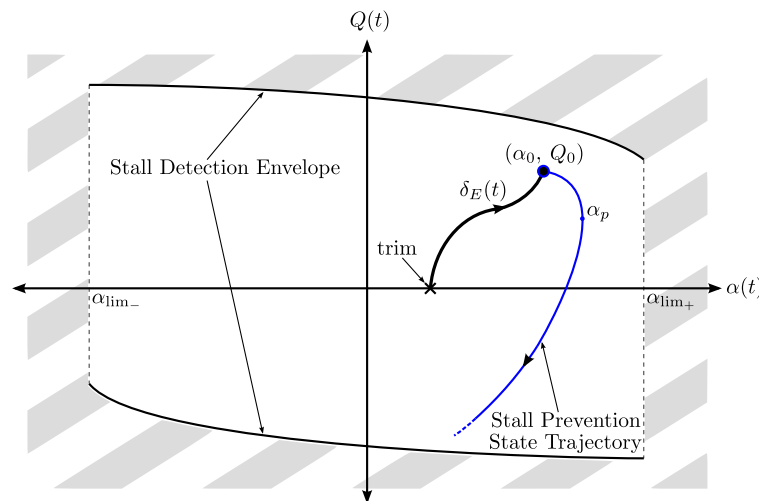


**Figure 5.2:** Stall detection envelope sketch for the stall prevention state trajectories

The envelopes (top and bottom) of this region describes the state values that, when active stall prevention is applied, will create trajectories with peaks on the predefined (maximum and minimum) angle of attack limits. Therefore these envelopes indicate the last possible moment for the SPC to prevent the aircraft from exceeding the predefined angle of attack limits.

In order to predict the peak angle of attack values of these stall prevention state trajectories, the elevator signal in Figure 5.1(a) first needs to be expressed mathematically and substituted into the zero state response term of the state transition equation. These derivations will now follow.

## 5.2 Zero State Response

With reference to Equation (4.7), which defines the manner in which the input signal is injected into the state transition equation, the stall prevention elevator command can be graphically expressed as presented in Figure 5.3,

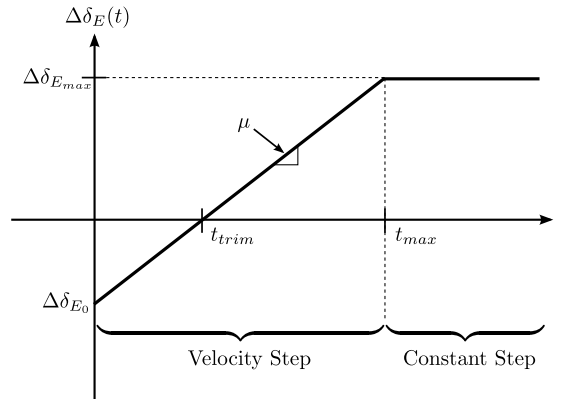


**Figure 5.3:** Stall prevention elevator input signal

where  $\Delta\delta_{E_0}$  and  $\Delta\delta_{E_{max}}$  denotes the initial and maximum elevator deflection offset from the trim angle respectively. These values are therefore defined as,

$$\Delta\delta_{E_0} = \delta_{E_0} - \delta_{E_{trim}} \quad (5.1)$$

$$\Delta\delta_{E_{max}} = \delta_{E_{max}} - \delta_{E_{trim}} \quad (5.2)$$

with the time instances  $t_{trim}$  and  $t_{max}$  coinciding with the trim and maximum elevator deflection angles respectively.

This elevator command can be described with a piecewise mathematical expression, to account for both the velocity step component (caused by the slew transition) and

the constant step component (caused by the saturation limit). This can be expressed in the time domain as follows,

$$\Delta\delta_E(t) = \begin{cases} \mu t + \Delta\delta_{E_0} & \text{if } 0 \leq t < t_{max} \\ \Delta\delta_{E_{max}} & \text{if } t \geq t_{max} \end{cases} \quad (5.3)$$

with the maximum time instance defined as,

$$t_{max} = \frac{\delta_{E_{max}} - \delta_{E_0}}{\mu}$$

Therefore, the zero state response term in the state transition equation, will calculate the convolution of Equation (5.3) with the state transition matrix of Equation (4.15).

$$\Phi(s)\mathbf{B}U(s) \Leftrightarrow \int_0^t e^{\mathbf{A}(t-\tau)}\mathbf{B}\Delta\delta_E(\tau)d\tau \quad (5.4)$$

To avoid solving the convolution integral, Equation (5.3) is transformed to the frequency domain to give,

$$U(s) = \begin{cases} \frac{\mu+s\Delta\delta_{E_0}}{s^2} & \text{for the velocity step component} \\ \frac{\Delta\delta_{E_{max}}}{s} & \text{for the constant step component} \end{cases} \quad (5.5)$$

With the elevator command defined in the frequency domain, the zero state response time expressions for the individual states can be derived from Equation (5.4). These state transition time functions will be derived for each of the input signal components, to yield the piecewise stall prevention state trajectory as presented graphically in Figure 5.4.

From a control perspective, by choosing the slew rate of the elevator input signal to be less than the maximum slew rate of the physical actuator, an additional buffer of protection against stall is created. This will effectively reduce the area of the pre-stall region by pulling the stall detection envelopes closer together, ensuring that the physical elevator will be more than capable of preventing stall. However, by choosing a very conservative slew rate, the normal flight envelope will be severely impeded. This results in a trade-off between stall safety margin and aircraft performance.

The zero state response transition equations for the velocity- and constant step input components will now be derived individually.



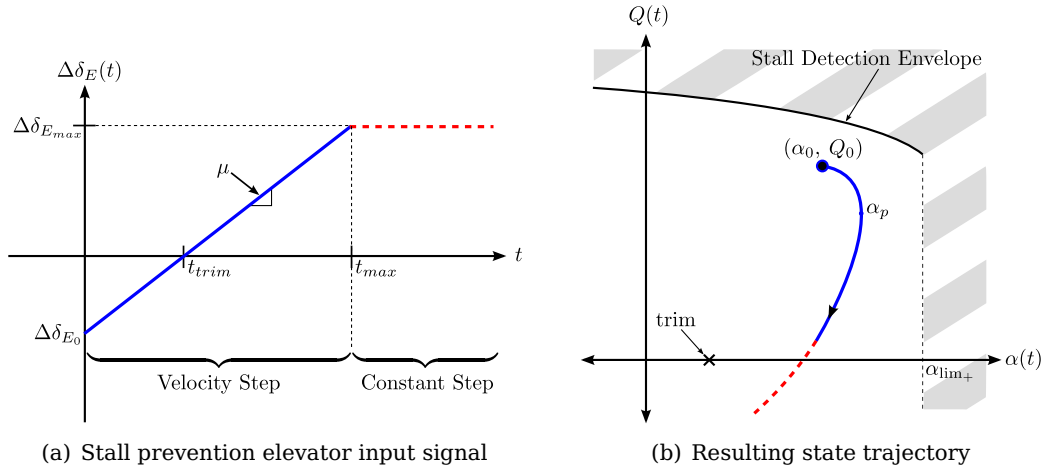


**Figure 5.4:** Graphical representation of the piecewise defined stall prevention state trajectory

### 5.2.1 Velocity Step Component

Substituting the expression for the velocity step input component into the left hand side of Equation (5.4) and maintaining the same symbolic notation implemented in Equation (4.14), gives the following,

$$\Phi(s)\mathbf{B}U(s) = \frac{1}{\lambda(s)} \begin{bmatrix} s - a_{22} & a_{12} \\ a_{21} & s - a_{11} \end{bmatrix} \begin{bmatrix} b_{11} \\ b_{21} \end{bmatrix} \left( \frac{\mu + s\Delta\delta_{E_0}}{s^2} \right) = \begin{bmatrix} \mathcal{F}_\alpha(s) \\ \mathcal{F}_Q(s) \end{bmatrix} \quad (5.6)$$

with  $\mathcal{F}_\alpha(s)$  and  $\mathcal{F}_Q(s)$  both having the symbolic form expressed in Equation (5.7).

$$\mathcal{F}(s) = \frac{a_2 s^2 + a_1 s + a_0}{s^2 \left( (s + \sigma)^2 + \omega_d^2 \right)} \quad (5.7)$$

The coefficients  $a_2$ ,  $a_1$  and  $a_0$  in Equation (5.7) are defined as follows for the angle of attack and pitch rate zero state response equations as follows:

$$\mathcal{F}_\alpha(s) \begin{cases} a_2 = b_{11}\Delta\delta_{E_0} \\ a_1 = \mu b_{11} + \Delta\delta_{E_0} (b_{21}a_{12} - b_{11}a_{22}) \\ a_0 = \mu (b_{21}a_{12} - b_{11}a_{22}) \end{cases} ; \quad \mathcal{F}_Q(s) \begin{cases} a_2 = b_{21}\Delta\delta_{E_0} \\ a_1 = \mu b_{21} + \Delta\delta_{E_0} (b_{11}a_{21} - b_{21}a_{11}) \\ a_0 = \mu (b_{11}a_{21} - b_{21}a_{11}) \end{cases}$$

Conducting a partial fraction expansion on the expression in Equation (5.7), yields the following equation,

$$\frac{a_2 s^2 + a_1 s + a_0}{s^2 \left( (s + \sigma)^2 + \omega_d^2 \right)} = \frac{A_1}{s} + \frac{A_2}{s^2} + \frac{A_3 \omega_d + A_4 (s + \sigma)}{(s + \sigma)^2 + \omega_d^2} \quad (5.8)$$

which can easily be inverse Laplace transformed to give the time expressions of the zero state response for a velocity step input. The resulting time functions are derived to have the following form for both the angle of attack and pitch rate states.

$$\mathcal{L}^{-1} [\mathcal{F}(s)] = f(t) = A_1 + A_2t + A_3e^{-\sigma t} \sin(\omega_d t) + A_4e^{-\sigma t} \cos(\omega_d t) \quad (5.9)$$

The coefficients  $A_1, A_2, A_3$  and  $A_4$  in Equation (5.9) are defined for both the angle of attack and pitch rate zero state response equations as follows,

$$\alpha_{ZS}(t); Q_{ZS}(t) \begin{cases} A_1 = a_1\kappa^{-1} - 2a_0\sigma\kappa^{-2} \\ A_2 = a_0\kappa^{-1} \\ A_3 = (a_2\sigma^2 - a_1\sigma + a_0 + \omega_d^2 A_1\sigma - \omega_d^2 A_2) (\omega_d\sigma^2)^{-1} \\ A_4 = (a_2 + a_1\sigma^{-1} + a_0\sigma^{-2} - 4A_1\sigma - A_1\omega_d^2\sigma^{-1} - 4A_2 - A_2\omega_d^2\sigma^{-2} - A_3\omega_d) (2\sigma)^{-1} \end{cases}$$

with  $\kappa = \sigma^2 + \omega_d^2$ .

Therefore by substituting these coefficients for the two state variables into Equation (5.9), yields the zero state response equations in the time domain for the angle of attack and pitch rate states respectively.

To verify the accuracy of the derived state transition equations for the zero state response with a velocity step input signal, consider the simulation results presented in Figure 5.5,

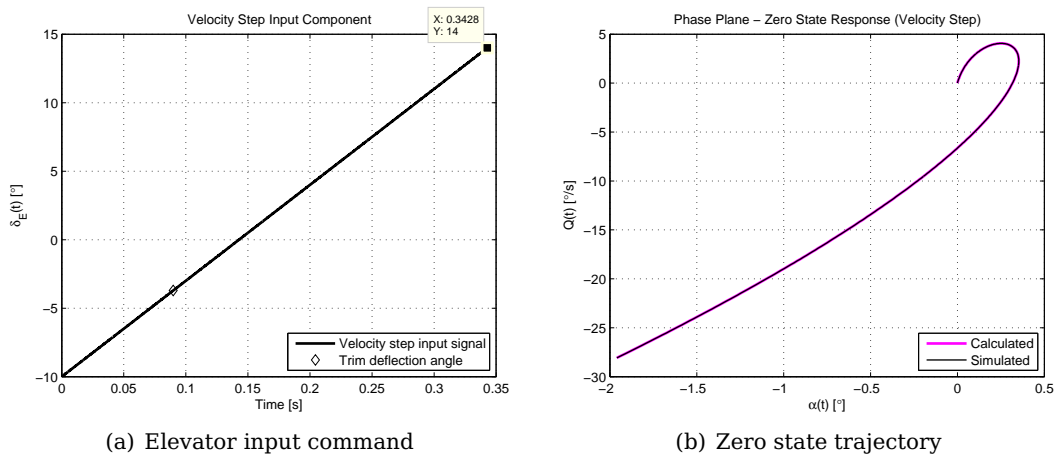


**Figure 5.5:** Zero state trajectory for a velocity step input signal

A conservative slew rate of  $70^\circ/\text{s}$  was chosen for this simulation [20], with the starting elevator deflection angle at  $-10^\circ$  (if this was held constant the aircraft would pitch up and eventually stall). The physical elevator control surface on the aircraft used for this research project, has a deflection range of  $\pm 14^\circ$ , therefore  $\delta_{E_{max}} = 14^\circ$ . The trimmed flight condition during this simulation was assumed the same as before.

The results in Figure 5.5 show how the initial elevator deflection angle attempts to increase the angle of attack and pitch as the aircraft pitches up. As the elevator is slewed to the positive maximum, the initial direction of the trajectory changes, resulting in the aircraft pitching down. This is the desired result the elevator command in Figure 5.1 intended for.

Figure 5.5 confirms that the initial state values are zero for this trajectory and that the only initial value required for this forward propagation, is the current (or mathematically the initial) elevator deflection angle. The time instances  $t_{trim}$  and  $t_{max}$  were calculated to have the values 0.0898 s and 0.3429 s respectively, which concurs with the simulated results.

### 5.2.2 Constant Step Component

The constant step input component is the simpler of the two excitation signals. By simply setting the slew rate parameter  $\mu$  equal to zero and choosing the initial deflection angle  $\Delta\delta_{E_0}$  as the maximum saturation limit  $\Delta\delta_{E_{max}}$ , the zero state transition equations for a constant step input can easily be derived from the expressions for the velocity step component. Substituting these simplifications into the coefficients  $a_2$ ,  $a_1$  and  $a_0$  of Equation (5.7), yields the following,

$$\mathcal{F}_\alpha(s) \begin{cases} a_2 = b_{11}\Delta\delta_{E_{max}} \\ a_1 = \Delta\delta_{E_{max}}(b_{21}a_{12} - b_{11}a_{22}) \\ a_0 = 0 \end{cases} \quad ; \quad \mathcal{F}_Q(s) \begin{cases} a_2 = b_{21}\Delta\delta_{E_{max}} \\ a_1 = \Delta\delta_{E_{max}}(b_{11}a_{21} - b_{21}a_{11}) \\ a_0 = 0 \end{cases}$$

Thus  $\mathcal{F}_\alpha(s)$  and  $\mathcal{F}_Q(s)$  both have the following symbolic form for the zero state response equation with a constant step input in the frequency domain.

$$\mathcal{F}(s) = \frac{a_2s + a_1}{s((s + \sigma)^2 + \omega_d^2)} \quad (5.10)$$

Conducting a partial fraction expansion on the expression in Equation (5.10) and as-

suming the same coefficient notation as before, yields the following equation,

$$\frac{a_2 s + a_1}{s \left( (s + \sigma)^2 + \omega_d^2 \right)} = \frac{A_1}{s} + \frac{A_3 \omega_d + A_4 (s + \sigma)}{(s + \sigma)^2 + \omega_d^2} \quad (5.11)$$

which again can easily be inverse Laplace transformed to give the time expressions of the zero state response for a constant step input. The resulting time functions are derived to have the following form for both the angle of attack and pitch rate states.

$$\mathcal{L}^{-1}[\mathcal{F}(s)] = f(t) = A_1 + A_3 e^{-\sigma t} \sin(\omega_d t) + A_4 e^{-\sigma t} \cos(\omega_d t) \quad (5.12)$$

The coefficients  $A_1$ ,  $A_3$  and  $A_4$  in Equation (5.12) are defined for both the angle of attack and pitch rate zero state response equations as follows,

$$\alpha_{ZS}(t); Q_{ZS}(t) \begin{cases} A_1 = a_1 \kappa^{-1} \\ A_3 = (a_2 \sigma - a_1 + \omega_d^2 A_1) (\omega_d \sigma)^{-1} \\ A_4 = -A_1 \end{cases}$$

with  $\kappa = \sigma^2 + \omega_d^2$  and the coefficient  $A_2$  zero.

Therefore substitution of these coefficients for the two state variables into Equation (5.12), yields the zero state response equation in the time domain for the angle of attack and pitch rate respectively.

To verify the accuracy of the derived state transition equations for the zero state response with a constant step input signal, consider the simulation results presented in Figure 5.6,

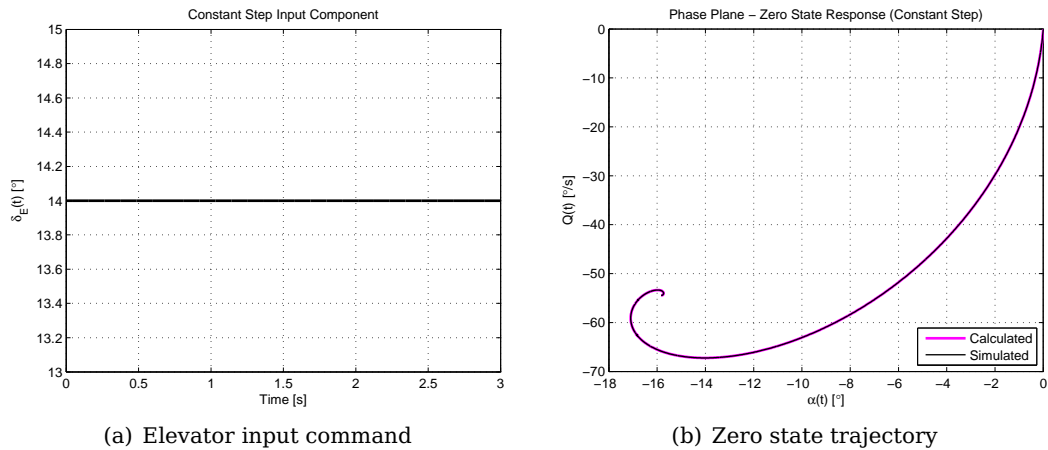


**Figure 5.6:** Zero state trajectory for a constant step input signal

This simulation was conducted independently from the velocity step simulation, hence the reason for the initial state values being zero. In general, to yield the zero state trajectory for the entire elevator input signal, the final state values (at  $t_{max}$ ) of the velocity step component, will be provided as initial state values for the constant step component. This will be shown in the next section, when the complete state transition equation will be considered to calculate the stall prevention state trajectory.

### 5.3 Complete State Transition Equation

The linear nature of the state transition equation allows the zero state response and the zero input response to be superimposed, by simply adding the coefficients of the corresponding terms together. This is true for both the velocity step component and the constant step component. Consider the following general form of the complete state transition equation,

$$f(t) = k + k_t t + k_s e^{-\sigma t} \sin(\omega_d t) + k_c e^{-\sigma t} \cos(\omega_d t) \quad (5.13)$$

with the coefficients for each the angle of attack and pitch rate states derived as follows.

$$\alpha(t) \begin{cases} k = \alpha_{trim} + A_1 \\ k_t = A_2 \\ k_s = \left( \frac{\Delta\alpha(-a_{22}-\sigma) + \Delta Q(a_{12})}{\omega_d} \right) + A_3 \\ k_c = \Delta\alpha + A_4 \end{cases} ; \quad Q(t) \begin{cases} k = A_1 \\ k_t = A_2 \\ k_s = \left( \frac{\Delta Q(-a_{11}-\sigma) + \Delta\alpha(a_{21})}{\omega_d} \right) + A_3 \\ k_c = \Delta Q + A_4 \end{cases}$$

By simply substituting the coefficients for either the velocity step or constant step component, the associated complete state trajectory can be calculated. Recall that the initial state values  $\Delta\alpha$  and  $\Delta Q$  for the constant step state trajectory, will be the final state values of the velocity step state trajectory at  $t_{max}$ , to yield the complete piecewise defined state trajectory for the input signal defined in Equation (5.3).

The following tables reiterate the coefficients ( $A_1$ ,  $A_2$ ,  $A_3$  and  $A_4$ ) of the velocity- and constant step zero state response components for the angle of attack and pitch rate states, where  $\kappa = \sigma^2 + \omega_d^2$ .

Only the contribution from the static terms  $L_0$  and  $M_0$  (the state trim values) has been included in the coefficient definitions of Equation (5.13), with the gravitational contribution omitted from this derivation for the sake of clarity. The contribution from the gravitational term (at a constant flight path angle) can easily be calculated from

| Velocity Step Input Coefficients  |  |
|---|--|
| Angle of Attack   | Pitch Rate   |
| $a_2 = b_{11}\Delta\delta_{E_0}$  | $a_2 = b_{21}\Delta\delta_{E_0}$                                     |
| $a_1 = \mu b_{11} + \Delta\delta_{E_0}(b_{21}a_{12} - b_{11}a_{22})$  | $a_1 = \mu b_{21} + \Delta\delta_{E_0}(b_{11}a_{21} - b_{21}a_{11})$ |
| $a_0 = \mu(b_{21}a_{12} - b_{11}a_{22})$  | $a_0 = \mu(b_{11}a_{21} - b_{21}a_{11})$                             |
| $A_1 = a_1\kappa^{-1} - 2a_0\sigma\kappa^{-2}$  |  |
| $A_2 = a_0\kappa^{-1}$  |  |
| $A_3 = (a_2\sigma^2 - a_1\sigma + a_0 + \omega_d^2 A_1\sigma - \omega_d^2 A_2)(\omega_d\sigma^2)^{-1}$  |  |
| $A_4 = (a_2 + a_1\sigma^{-1} + a_0\sigma^{-2} - 4A_1\sigma - A_1\omega_d^2\sigma^{-1} - 4A_2 - A_2\omega_d^2\sigma^{-2} - A_3\omega_d)(2\sigma)^{-1}$ |  |

**Table 5.1:** The coefficients for the zero state transition equation given a velocity step input

| Constant Step Input Coefficients                                |   |
|---|---|
| Angle of Attack   | Pitch Rate  |
| $a_2 = b_{11}\Delta\delta_{E_{max}}$                            | $a_2 = b_{21}\Delta\delta_{E_{max}}$                        |
| $a_1 = \Delta\delta_{E_{max}}(b_{21}a_{12} - b_{11}a_{22})$     | $a_1 = \Delta\delta_{E_{max}}(b_{11}a_{21} - b_{21}a_{11})$ |
| $a_0 = 0$   | $a_0 = 0$   |
| $A_1 = a_1\kappa^{-1}$  |   |
| $A_2 = 0$   |   |
| $A_3 = (a_2\sigma - a_1 + \omega_d^2 A_1)(\omega_d\sigma)^{-1}$ |   |
| $A_4 = -A_1$  |   |

**Table 5.2:** The coefficients for the zero state transition equation given a constant step input

the expressions derived to calculate the constant step contribution. The results can simply be superimposed onto the associated coefficients of Equation (5.13). This is shown in Appendix A.

### 5.3.1 Stall Prevention State Trajectory

Assuming the same trimmed flight condition that was used during the previous simulations, consider the following analysis of the complete state transition equations for the active stall prevention elevator command. Given a conservative slew rate of  $70^\circ/\text{s}$  and initial elevator deflection angle of  $-10^\circ$ , the calculated state trajectory from the initial point in the phase plane ( $8^\circ$ ,  $50^\circ/\text{s}$ ) is presented in Figure 5.7.

For the chosen slew rate, initial state and initial elevator values, the resulting state trajectory would exceed the predefined maximum angle of attack limit. Notice that this peak occurs during the slew transition in the elevator signal. However, in general this will not always be the case, since certain combinations of the variables will result in the peak angle of attack coinciding with the constant step component of the elevator signal. Therefore, since the state trajectory is piecewise defined, the angle of attack peak value for the individual components needs to be calculated, to determine the maximum peak (or minimum peak for negative stall) over the entire trajectory.

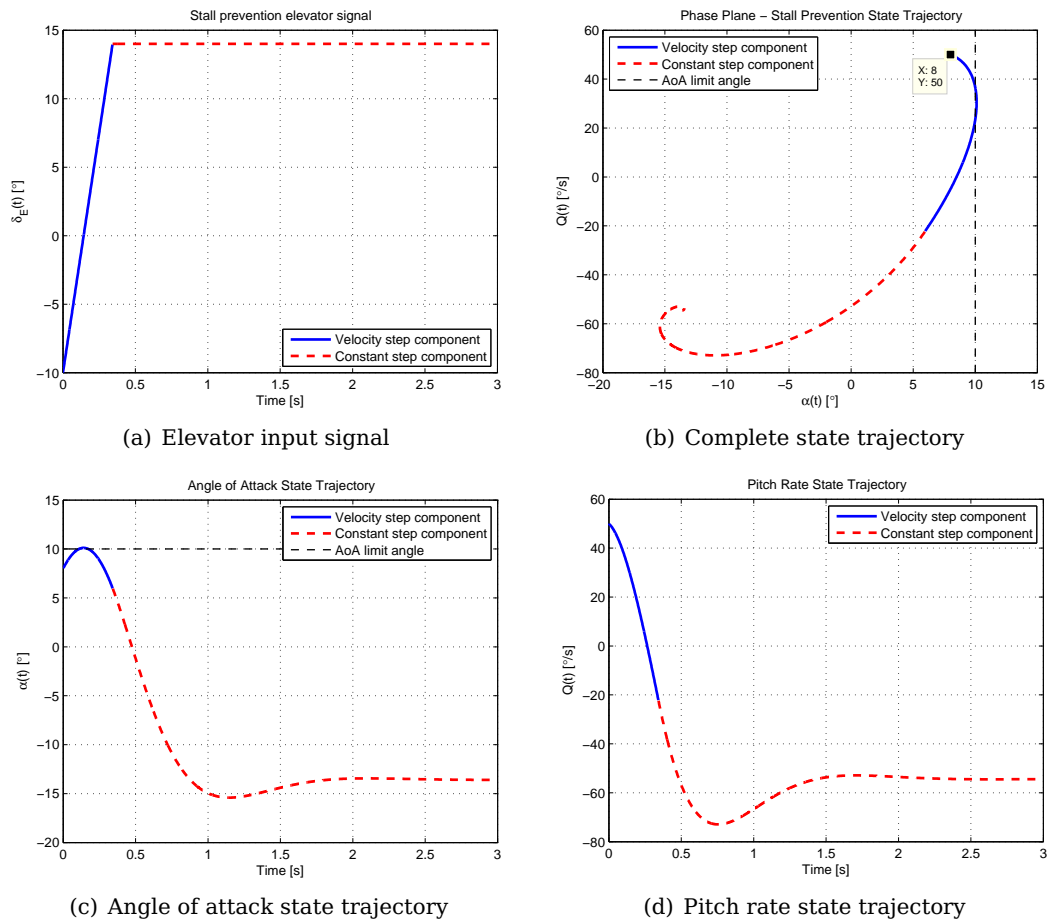


**Figure 5.7:** Phase plane analysis of complete state trajectory

Expanding this simulation to determine the stall detection envelope for state trajectories resulting for this active stall prevention elevator signal, yields the results presented in Figure 5.8. Notice that the initial point is located on the positive stall detection envelope, as would be expected from the results presented in Figure 5.7.

In addition to the velocity magnitude affecting the pre-stall region, this state trajectory introduces two additional variables ( $\mu$  and  $\Delta\delta_{E_0}$ ) that affect the proximity of the stall detection envelope. Consider the simulation results presented in Figure 5.9, which display the effect of the initial elevator deflection angle on the stall detection envelope given a conservative slew rate of  $70^\circ/\text{s}$ .

The upper envelope detects when the trajectory will exceed the maximum predefined angle of attack limit, if the current elevator angle is already at  $\delta_{E_{max}}$ , the upper envelope is farther away from trim. This is as a result of the slew transition, caused by velocity step component, being excluded from the state trajectory calculation. In contrast, when the current elevator angle is at  $\delta_{E_{min}}$ , the opposite occurs and the upper envelope moves closer to trim as a result of the velocity step component slewing across the entire deflection range of the elevator. A similar observation can be made

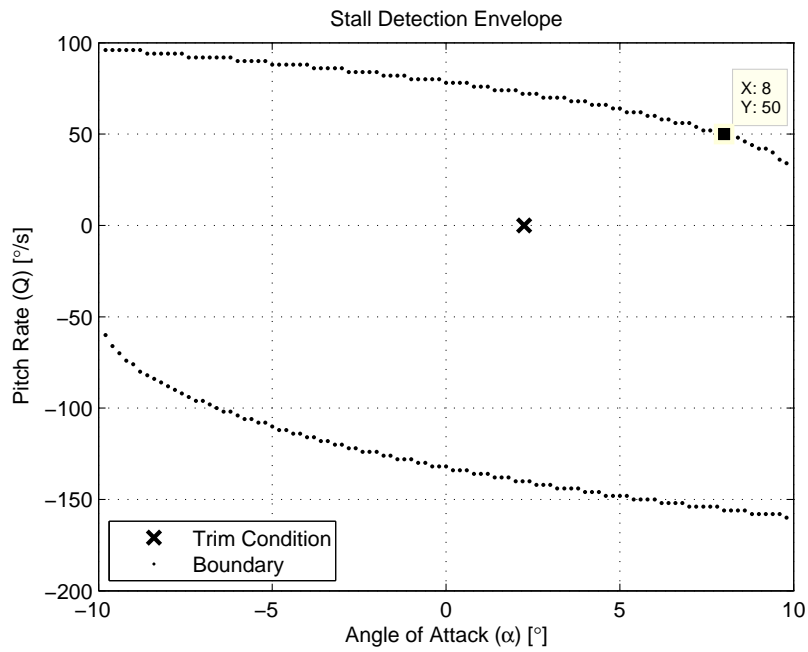


**Figure 5.8:** Stall detection envelope for the stall prevention state trajectory

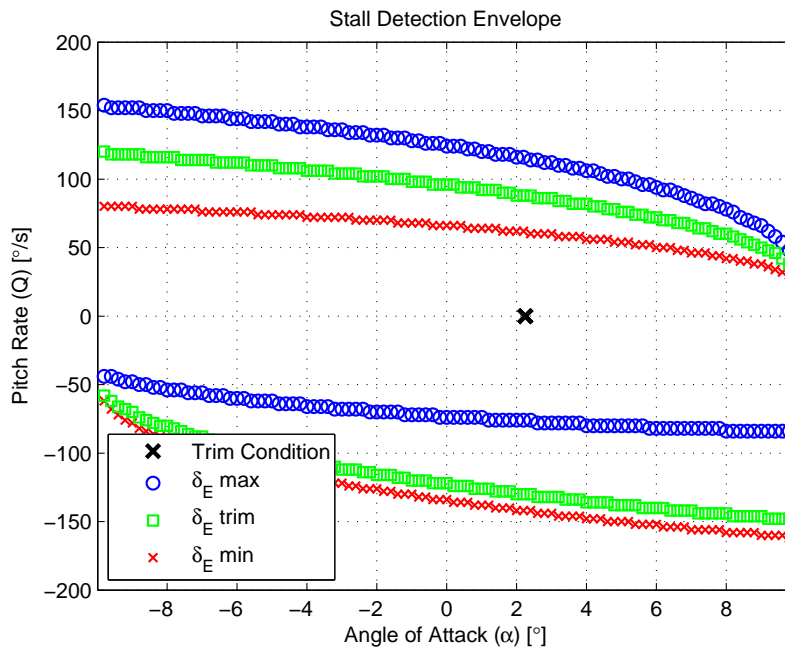


**Figure 5.9:** Effect of variation in the initial elevator angle on the stall detection envelope

for the lower detection envelope.

As a result, the pre-stall region in the phase plane varies dynamically with the operating flight condition, continuously predicting the last possible moment for which active stall prevention could be applied without exceeding the predefined angle of attack limits.



By manipulating the equations derived to calculate the complete state trajectory, the peak angle of attack value can be predicted having only knowledge of the chosen slew rate, initial state and initial elevator values<sup>3</sup>. This will be presented in the next section and will be used to construct the detection algorithm.

## 5.4 AoA Peak Prediction

As mentioned in the previous section, the peak angle of attack needs to be calculated for each of the individual state trajectory components. This is achieved by deriving expressions for the angle of attack peak time instances for each of the separate trajectory components. The peak angle of attack for each trajectory can then be calculated and compared to determine the maximum or minimum for the entire trajectory.

Incorporating these angle of attack peak prediction methods into a detection algorithm, will allow the stall prevention control system to determine the last possible moment to override and dynamically limit the elevator command. Consider the block diagram in Figure 5.10 of the detection algorithm.

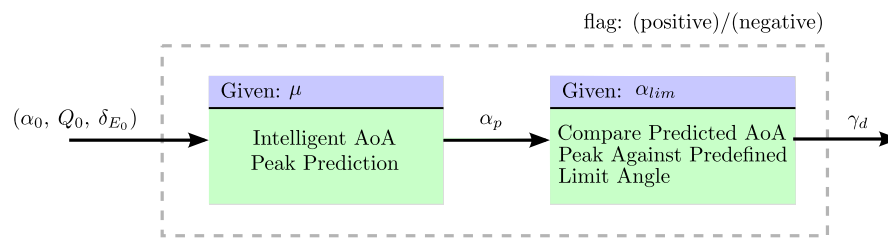


**Figure 5.10:** Detection algorithm block diagram

Depending on the location of the state vector in the phase plane, a flag will be triggered in the detection algorithm to enable the peak prediction for either the positive or negative AoA limit.

The following normalised time convention simplifies the analysis and allows the individual state trajectory components to be considered separately,

$$t_v \in 0 \leq t < t_{max}$$

$$t_c \in t \geq t_{max}$$

where  $t_v$  represents the state trajectory as a result of the velocity step component and  $t_c$  the trajectory as a result of the constant step component.

<sup>3</sup>These initial values referred to here, are the initial values to the state transition equation. However, these are the values at the current flight condition.

### 5.4.1 Peak angle of attack as a result of the velocity step input

For the stall prevention state trajectory presented in Figure 5.7(b), the trajectory caused by only the velocity step component of the elevator command is presented in Figure 5.11. Notice how superimposing the zero input trajectory onto the zero state

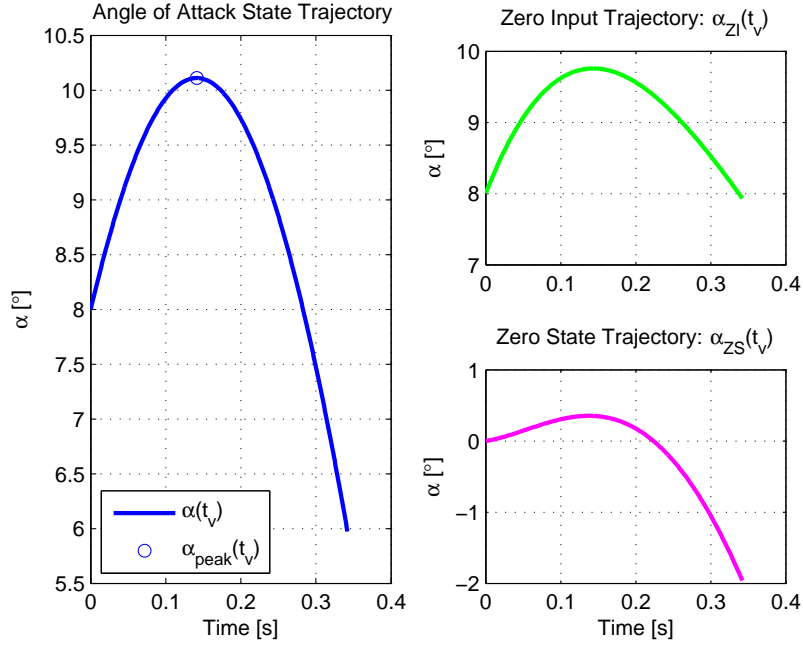


**Figure 5.11:** AoA state trajectory as a result of the velocity step input

trajectory yields the entire state trajectory for this section. The peak angle of attack for this section is also indicated in Figure 5.11.

The state transition equation for this state trajectory is defined in Equation (5.13) with the coefficients given in Table 5.1. The general form of the state transition equation for this part of the state trajectory is restated here for convenience.

$$f(t) = k + k_t t + k_s e^{-\sigma t} \sin(\omega_d t) + k_c e^{-\sigma t} \cos(\omega_d t) \quad (5.14)$$

Taking the first time derivative of Equation (5.14) gives the following expression,

$$\dot{f}(t) = k_t + \hat{k}_s e^{-\sigma t} \sin(\omega_d t) + \hat{k}_c e^{-\sigma t} \cos(\omega_d t)$$

with coefficients,

$$\begin{aligned} \hat{k}_c &= -k_c \sigma + k_s \omega_d \\ \hat{k}_s &= -k_c \omega_d - k_s \sigma \end{aligned}$$

Substituting  $\dot{f}(t) = 0$  and solving for  $t$ , will yield the closed form solution for the time instances at the peaks of the function. The result of this substitution yields the following equation,

$$\hat{K}e^{-\sigma t} \sin(\omega_d t + \hat{\varphi}) = -k_t \quad (5.15)$$

where,

$$\begin{aligned} \hat{K} &= \pm \sqrt{(\hat{k}_c)^2 + (\hat{k}_s)^2} \\ \hat{\varphi} &= \tan^{-1} \left( \frac{\hat{k}_c}{\hat{k}_s} \right) \end{aligned}$$

Due to the non-periodic nature of this equation and the added offset term, solving this equation analytically proves cumbersome. With the available resources, the attempts at finding a closed form solution for the time variable proved unsuccessful. Therefore a numerical approach was adopted to solve Equation (5.15). The method of choice was Newton-Raphson, due to its rapid convergence when the initial iterate is close to the desired value. Newton-Raphson is based on the analytic substitution of the local tangent line for the function and then use the zero of this line as the next approximation of the zero of the function. This is presented graphically in Figure 5.12, with the approximation law expressed in Equation (5.16) below.

$$x_{k+1} = x_k + \frac{f(x_k)}{f'(x_k)} \quad (5.16)$$

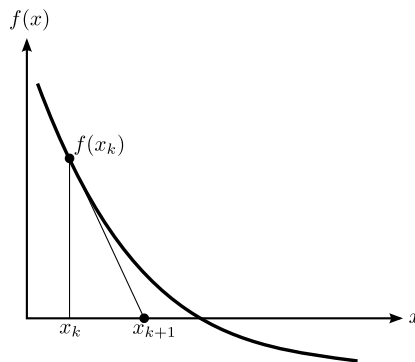


**Figure 5.12:** Graphical presentation of the Newton Raphson approximation method

where  $x$  represents the time variable,  $f(x)$  the state transition equation,  $f'(x)$  the first time derivative of the state transition equation and the subscripts  $k$  and  $k + 1$  indicating the current and next iteration respectively.

The approximation law expressed in Equation (5.16) calculates for the roots of the state transition equation. To solve for the roots of Equation (5.15), the approximation law needs to be expressed as follows,

$$x_{k+1} = x_k + \frac{f'(x_k)}{f''(x_k)} \quad (5.17)$$

One of the weaknesses of this method is that it relies on choosing an initial iterate close to the root's expected position. If the structure of the function  $f(x)$  is not known, then choosing an inaccurate initial iterate can lead to divergence in the approximation. However, since the local structure of the function is known in some detail, an accurate estimate of the time instance at the peak can be made. Upon analysis it was found that by choosing the initial guess to be the time value  $t_{max}/2$ , the numeric solution will always converge to the correct peak for all possible combinations of the initial variables in the local neighbourhood of the stall detection envelope. With the convergence being quadratic in most cases.

For the current combination of initial state values and elevator angle, the root converged in two iterations to within a error margin of  $10^{-4}$ . The result is a time instance with a value of 0.1412 s, which concurs with the peak angle of attack indicated in Figure 5.11.

There exists certain combinations of the initial state and elevator values that will result in Equation (5.15) having no positive real roots for  $t$ . In such cases the numerical approximation will never converge for the initial guess of  $t_{max}/2$ . This is caused by the offset term  $k_t$  and indicates that the peak for the entire state trajectory will most likely coincide with the trajectory section produced by the constant step input component.

The maximum angle of attack of this state trajectory section will therefore either be located at  $t = 0$  or  $t = t_{max}$ . To account for such cases, the convergence of the approximation is monitored by observing the error between approximation steps. If the absolute value of this error is greater than a certain threshold at the end of a specified maximum number of iterations, then it is safe to assume the approximation diverged.

#### 5.4.2 Peak angle of attack as a result of the constant step input

For the stall prevention state trajectory presented in Figure 5.7(b), the trajectory caused by only the constant step component of the elevator command is presented in Figure 5.13. This section of the state trajectory initiates at the end of the previous section, therefore assuming the initial angle of attack and pitch rate state values at  $t_{max}$ .

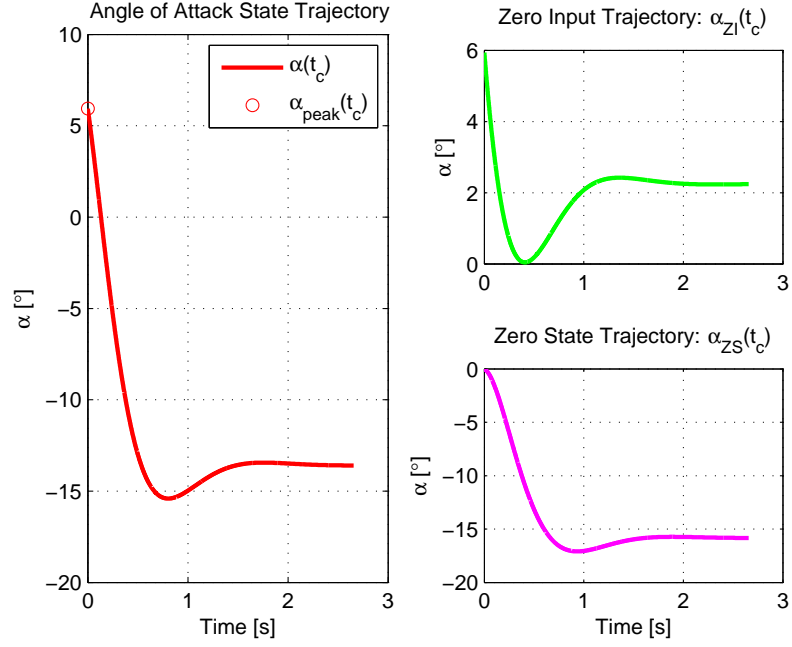


**Figure 5.13:** AoA state trajectory as a result of the constant step input

The state transition equation for this state trajectory is define in Equation (5.12) with the coefficients defined in Table 5.2. The general form of this state transition equation is restated here for convenience.

$$f(t) = k + k_s e^{-\sigma t} \sin(\omega_d t) + k_c e^{-\sigma t} \cos(\omega_d t) \quad (5.18)$$

This is exactly the same form as the zero input state transition equation for the angle of attack state expressed in Equation (4.22). Therefore the closed form solution derived for the peak time instances in Equation (4.25), is transferable to the constant step state trajectory component. The results are expressed here in Equation (5.19),

$$\begin{aligned} 0 &= \hat{K} e^{-\sigma t} \sin(\omega_d t + \hat{\varphi}) \\ \therefore \sin(\omega_d t + \hat{\varphi}) &= 0 \\ \therefore t &= -\frac{\hat{\varphi}}{\omega_d} + \frac{n\pi}{\omega_d} \quad n \in 0, 1, 2, 3, \dots \end{aligned} \quad (5.19)$$

where,

$$\begin{aligned} \hat{K} &= \pm \sqrt{(\hat{k}_c)^2 + (\hat{k}_s)^2} \\ \hat{\varphi} &= \tan^{-1} \left( \frac{\hat{k}_c}{\hat{k}_s} \right) \end{aligned}$$

with coefficients,

$$\begin{aligned}\hat{k}_c &= -k_c\sigma + k_s\omega_d \\ \hat{k}_s &= -k_c\omega_d - k_s\sigma\end{aligned}$$

In this simulation the peak time instance for this response is located at  $t = 0$  s, which is usually the case when the peak time instance calculated for the velocity step induced state trajectory is less than  $t_{max}$ . Thus the peak calculation algorithm includes these considerations during its decision process which allows for the maximum peak value to be calculated with computational efficiency.

### 5.4.3 Linear Verification

To verify the detection algorithm developed in the previous section, consider the following linear simulation applied to the linear normal dynamics model. The simulation is conducted at the same trim condition as before, with the elevator deflected to its minimum angle (therefore full pitch up motion) at the start of the simulation. The angle of attack and pitch rate measurements are then evaluated by the detection algorithm. Consider the calculated state trajectory at  $t = 0.149$  s superimposed onto the measured angle of attack and pitch rate states presented in Figure 5.14.

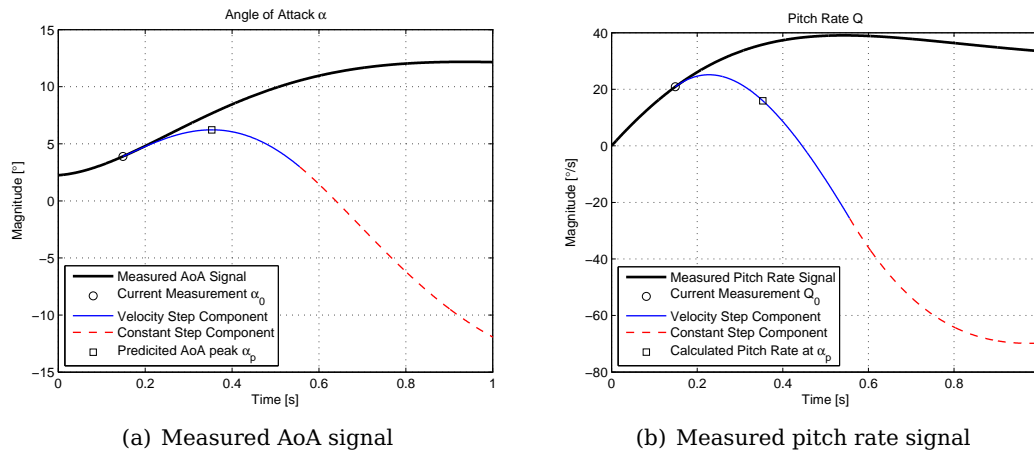


**Figure 5.14:** State trajectory calculated for the stall prevention elevator input signal at  $t = 0.149$  s

The angle of attack peak value indicated in Figure 5.14(a) is calculated using the AoA peak prediction algorithm, which for this measurement yields a value much less than the allowed maximum angle of attack limit. Therefore, at this time instance, the aircraft's autopilot will continue to operate normally without intervention by the stall prevention control system.

The elevator input signal, simulating stall prevention at  $t = 0.149$  s, can be seen in Figure 5.15 superimposed onto the actual elevator command.

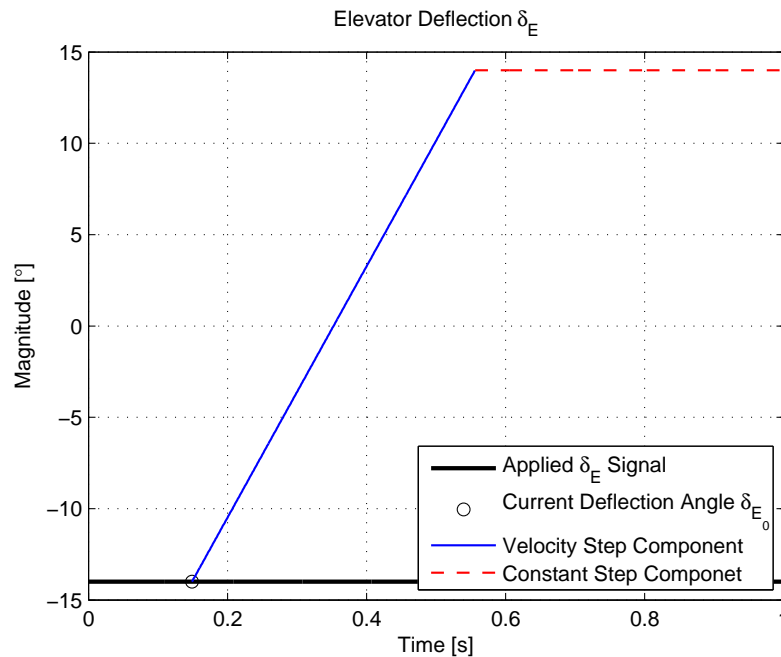


**Figure 5.15:** The elevator input command displaying the simulated recovery excitation signal

By calculating the peak AoA at every state measurement and plotting it as a function of time, gives a graph which indicates the time instance when the state vector will exit the stall detection envelope. This is presented in Figure 5.16.

From Figure 5.16 it is clear that the AoA peak value will first exceed the maximum allowed limit at  $t = 0.418$  s. This time instance relates to a specific angle of attack, pitch rate and elevator deflection angle<sup>4</sup> measurement. To gain insight into the safety margin created by this detection algorithm, consider the phase plane analysis presented of the current simulation.

Figure 5.17 displays a few stall prevention state trajectories progressively simulated for future and past state measurements relative to the state trajectory calculated at  $t = 0.149$  s. The state measurement at  $t = 0.418$  s has the value of  $\alpha = 8.738^\circ$  and  $Q = 37.79^\circ/s$ , which is safely below the maximum allowed AoA limit. This detection will allow adequate time for the prevention control algorithm to respond and prevent the angle of attack from exceeding  $\alpha_{lim}$ .

With the chosen slew rate a conservative estimate of the the elevator's physical capability, the stall prevention controller can easily prevent the angle of attack from exceeding  $\alpha_{lim}$  by simply overriding the elevator command from the NSA controller

<sup>4</sup>Note that for this simulation the elevator deflection is held constant at its minimum saturation angle.

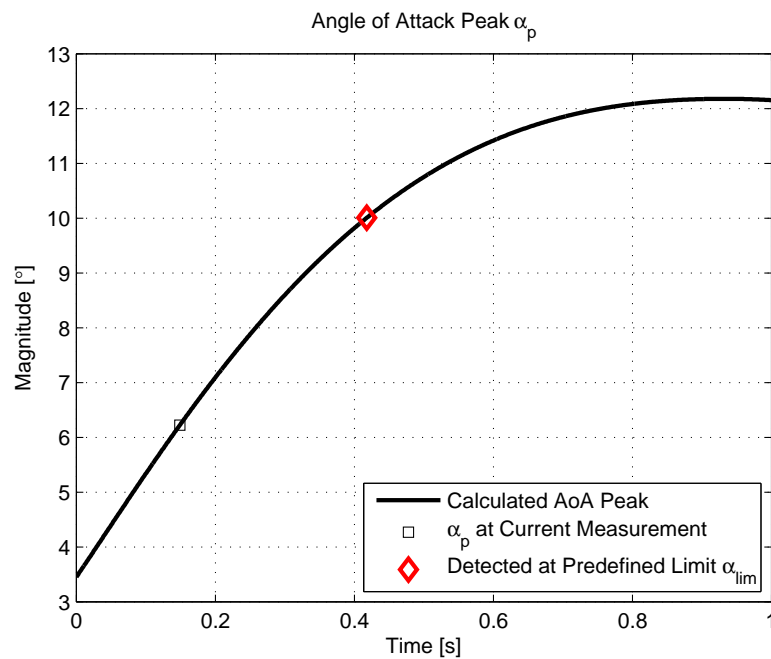


**Figure 5.16:** The calculated AoA peak values for every state measurement

with the elevator command presented in Figure 5.3. However, due to disturbances such as wind or sensor noise, this open loop approach might not yield the desired results. To combat this, a control method was designed to recursively solve for the slew rate of the elevator input signal to allow the state vector to track the predicted stall prevention state trajectory. This will ensure feedback from the measured angle of attack and pitch rate states and in essence is a form of model predictive control. This first stage of the stall prevention control strategy is developed in the following section.

## 5.5 Recursive Model Predictive Slew Rate Control

The purpose of this stage, as mentioned in Chapter 3, is to optionally guide the angle of attack towards the limit angle. The method behind this control approach is to ensure (once detection has occurred) that the angle of attack peak value, calculated by the detection algorithm, will always equal the limit angle during this control stage. This is achieved by adjusting the slew rate of the velocity step section in the stall prevention elevator command. By calculating the appropriate slew rate and applying it to the elevator actuator during this slew transition phase, will ensure that the calculated angle of attack peak will never exceed the predefined limit angle. This allows the angle of attack to track the stall prevention state trajectory and will minimise any overshoot when the second stall prevention control stage is triggered.



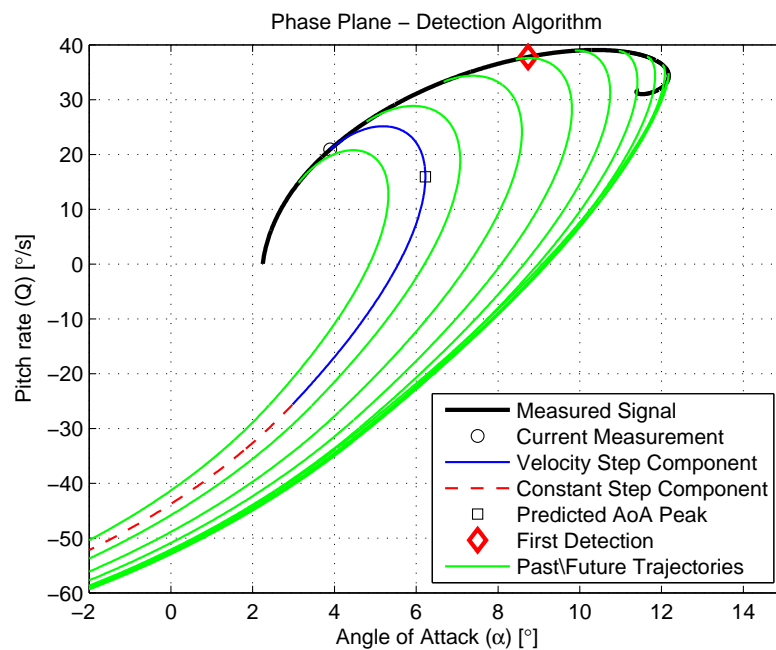


**Figure 5.17:** The Phase Portrait of the linear simulation displaying the calculated recovery trajectories

### 5.5.1 Modified False Position Method

To calculate the appropriate slew rate, the angle of attack peak value needs to be calculated recursively at the current operating condition through inverse interpolation to determine the slew rate which will yield a peak value equal to the limit angle. A method well suited for this application is called *Regula Falsi*, better known as the method of false position [21]. It attempts to minimise a specified function by recursively solving for the appropriate value of the independent variable,

$$y = f(x)$$

find  $x = \xi$  such that,

$$f(\xi) = 0$$

By condensing the peak calculation procedure (developed in the previous chapter) to a function  $\alpha_p(\mu)$  where the slew rate (of the elevator command) is provided as input, the output will then yield the peak angle of attack calculated by forward propagating with the specified slew rate. This is incorporated into the concept of the false position method as follows,

$$f(\mu) = \alpha_{lim} - \alpha_p(\mu) \quad (5.20)$$

where the independent variable becomes the slew rate of the elevator signal and the

objective is to find  $\mu = \mu_\xi$  such that,

$$f(\mu_\xi) = 0$$

therefore,

$$\alpha_p(\mu_\xi) = \alpha_{lim}$$

The method initialises with two initial points ( $\mu_0$  and  $\mu_1$ ) at which the function  $f(\mu)$  will have opposite signs. Therefore two slew rate values where the calculated  $\alpha_p$  is greater and less than the angle of attack limit respectively. This creates an interval where a peak value equal to the limit angle will exist. This interval is then recursively decreased by the computational law in Equation (5.21).

$$\mu_2 = \mu_1 - f(\mu_1) \left( \frac{\mu_1 - \mu_0}{f(\mu_1) - f(\mu_0)} \right) = \frac{\mu_0 f(\mu_1) - \mu_1 f(\mu_0)}{f(\mu_1) - f(\mu_0)} \quad (5.21)$$

After each step, the method continues with  $\mu_2$  and either of  $\mu_0$  or  $\mu_1$  for which the sign of  $f(\mu_0)$  or  $f(\mu_1)$  is opposite to the sign of  $f(\mu_2)$ . This process is repeated until the desired error tolerance between  $\alpha_{lim}$  and  $\alpha_p$  are met, to yield the appropriate slew rate value for the elevator signal.

The main weakness of this method is the one-sided approach to decreasing the interval, which in turn makes the convergence slow. However, through a simple modification in the computation law, this feature of the method is eliminated and rapidly increases the rate of convergence. This modification consists of dividing the function ( $f(\mu_0)$  or  $f(\mu_1)$ ) kept from the previous calculation by two and using this reduced function value for the current calculation [22]. The improvement over the original method is graphically presented in Figure 5.18 and as a result the modified false position method concludes the following procedure,

Given the function  $f(\mu)$  for an interval  $\mu_0 \leq \mu \leq \mu_1$  with  $f(\mu_0)f(\mu_1) < 0$  compute,

$$\mu_2 = \frac{\mu_0 f(\mu_1) - \mu_1 f(\mu_0)}{f(\mu_1) - f(\mu_0)}, \quad f(\mu_2) = \alpha_{lim} - \alpha_p(\mu_2)$$

$$\text{if } f(\mu_0)f(\mu_2) \begin{cases} < 0 & \text{then } \begin{cases} \mu_2 & \text{becomes new } \mu_1 \\ \frac{f(\mu_0)}{2} & \text{becomes new } f(\mu_0) \end{cases} \\ = 0 & \text{then computation is complete} \\ > 0 & \text{then } \begin{cases} \mu_2 & \text{becomes new } \mu_0 \\ \frac{f(\mu_1)}{2} & \text{becomes new } f(\mu_1) \end{cases} \end{cases} \quad (5.22)$$

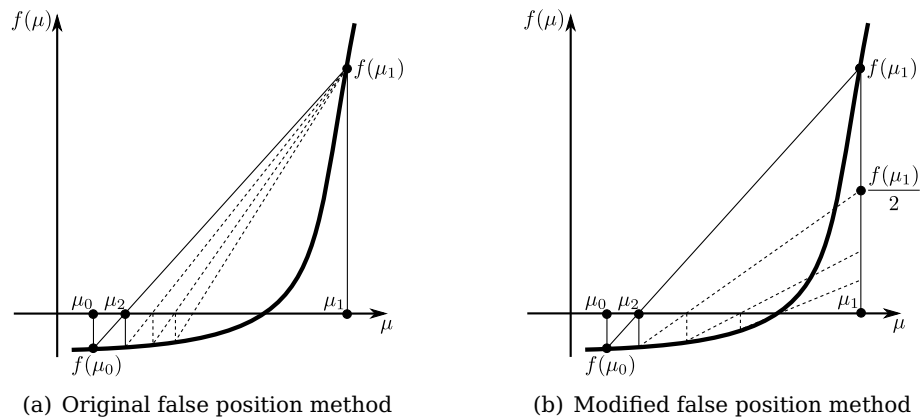


**Figure 5.18:** Graphical presentation of improvement over original false position method

On the actual flight control system, this control stage will make slight adjustments in the slew rate at each state measurement, as necessary. Note however that, during this control stage of the stall prevention control system, the NSA controller is in open loop and the stall prevention control system is continuously monitoring the elevator command calculated by the NSA control law. If the slew rate of this elevator command is less (in the absolute sense) than what is currently commanded by the slew rate control algorithm, it indicates that the  $C_{WR}$  input provided by the guidance control system will not cause the angle of attack to exceed its limit angle. In such an event, the stall prevention control system will deactivate and allow the flight control system to function normally with the NSA controller connected in closed loop.

To verify this slew rate control algorithm, consider the following simulation, where a initial state value was chosen to demonstrate its functionality.

### 5.5.2 Algorithm Verification

Consider the initial state value presented in Figure 5.19, which has a predicted peak angle of attack greater than the limit angle, given the conservative slew rate  $70^\circ/\text{s}$ .

Applying the slew rate control algorithm to this state value, yields the correct slew rate within nine iterations as shown in Figure 5.20.

Note that this state value is chosen to demonstrate the slew rate control algorithm and normally, due to the fast sample rate of the flight control system, small adjustments will be made in the slew rate during this stall prevention stage. Therefore preventing the predicted peak angle of attack from excessively exceeding the limit angle. By choosing the initial slew rate interval to be consistent with what is actually achievable by the physical elevator actuator, will prevent the slew rate control algorithm from requesting unachievable control effort.

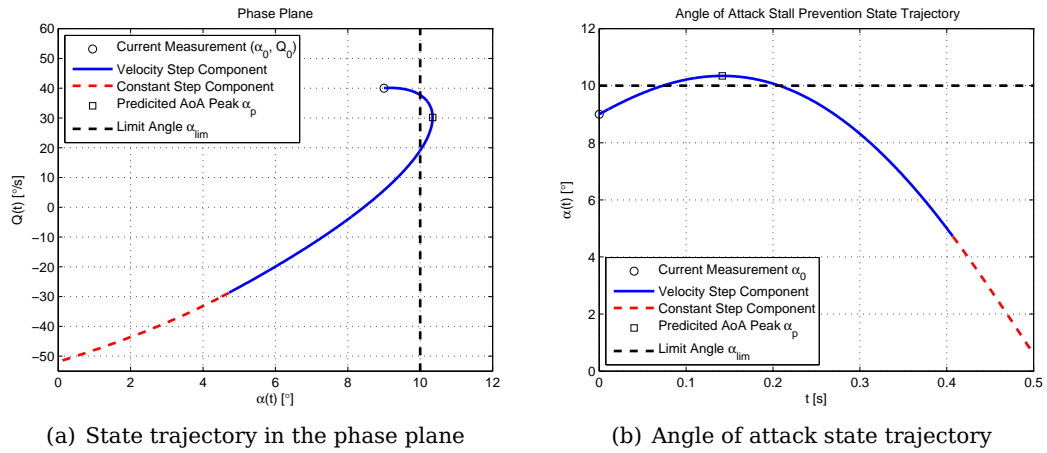


**Figure 5.19:** Simulated stall prevention state trajectory given the predefined slew rate

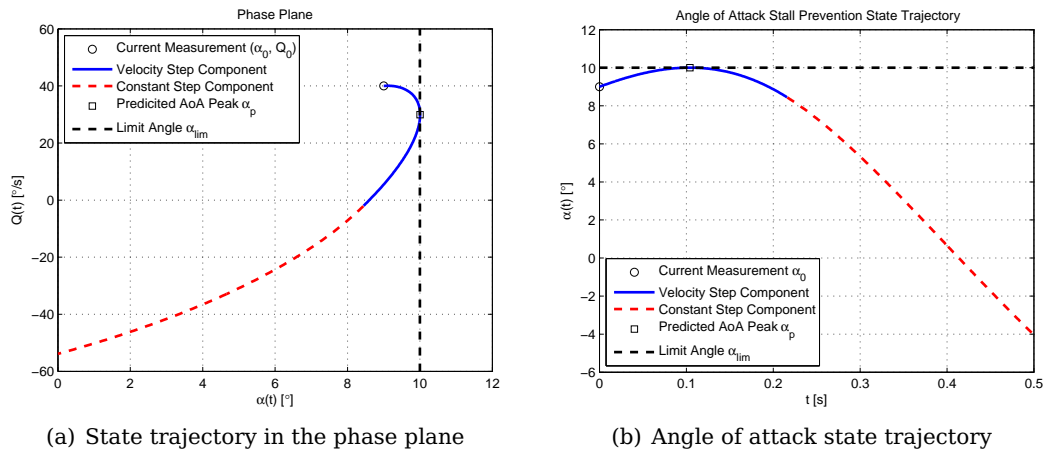


**Figure 5.20:** Simulated stall prevention state trajectory given the calculated slew rate

The modification in the elevator command is presented in Figure 5.21, which indicates the difference between the conservative slew rate and the required slew rate.

As the angle of attack is forced to track the stall prevention state trajectory, the angle of attack gradually approaches the predefined limit angle. When the angle of attack reaches a certain threshold value defined as  $\alpha_h$  where,

$$\alpha_h < \alpha_{lim} < \alpha_{crt}$$

the slew rate control stage terminates and triggers the angle of attack regulating control system to take control of the elevator command. This regulating controller is then initialised and has the purpose of regulating the angle of attack to the predefined limit angle. This AoA regulating controller will be the focus of the next chapter.

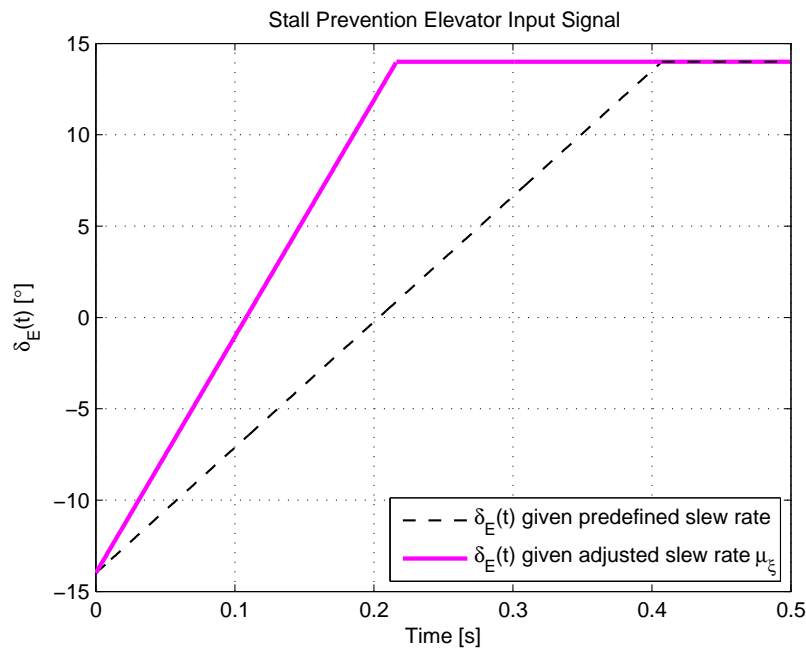


**Figure 5.21:** Adjustment of the stall prevention elevator signal at the current operating condition

## 5.6 Summary

In this chapter a elevator command was designed which will enforce active stall prevention onto the aircraft. This signal was used to calculate the state trajectory resulting from such a stall prevention manoeuvre. This allowed the peak angle of attack to be predicted through a peak prediction algorithm, which forms part of the detection algorithm. This led to the design of a control algorithm which allows the angle of attack to track this stall prevention state trajectory.

With the stall prevention part of the control strategy in place, the next step is to constrain the angle of attack at this limit angle by regulating it using some form of a reference tracking control system. The control system chosen for this purpose is based on the same control architecture as the NSA controller and will be designed in the following chapter.

## Chapter 6

# Angle of Attack Regulating Control

The switching policy developed in the previous chapter, will disconnect the NSA controller when the angle of attack approaches the predefined limit of the linear lift region. The stall prevention control system will then be activated and the slew rate control stage will guide the angle of attack towards the limit angle by overriding the elevator command to track the stall prevention state trajectory.

The chapter presents the development of the second stage of the control strategy and describes the finite state machine which forms the stall prevention control system.

### 6.1 Stall Prevention Control Strategy Description

The stall prevention control strategy includes two control stages, the *slew rate control* stage and *angle of attack regulating control* stage, which operates within a finite state machine configuration. Both stages prevents the angle of attack from exceeding its predefined limit angle, by dynamically limiting the elevator command.

Consider the conceptual representation of the operation of this stall prevention control system as presented in Figure 6.1, where  $t_d$  and  $t_c$  indicates when detection has occurred and when the angle of attack regulating stage has been activated respectively.

The slew rate control stage is the initial phase in the prevention control strategy and is triggered by the detection algorithm. As before, the purpose of this stage is to guide the angle of attack towards the limit angle by adjusting the slew rate of the elevator command, through feedback provided by the measured angle of attack and pitch rate signals. Once the angle of attack reaches the threshold value  $\alpha_h$ , this control stage will terminate and trigger the regulating control stage to activate as presented in

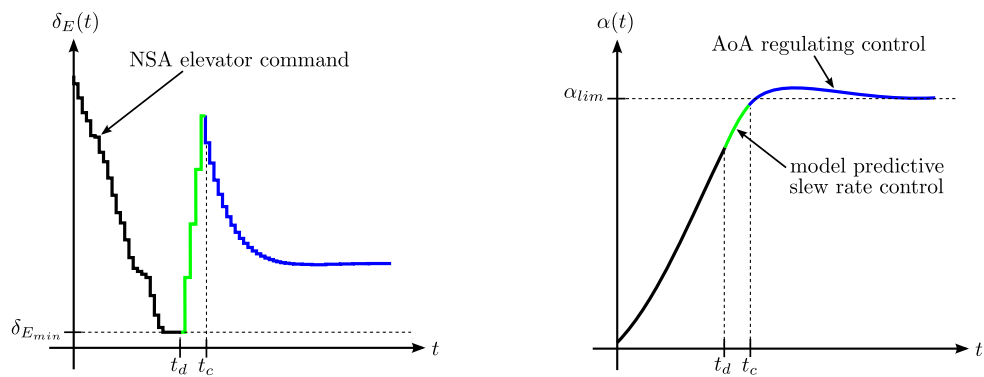


**Figure 6.1:** Stall prevention control overriding the elevator command signal

Figure 6.1. The angle of attack regulating control stage is designed to track the limit angle. This is achieved by providing the limit angle as the reference input to an angle of attack controller.

The slew rate control stage effectively acts to absorb the high energy contained within the state values as the state trajectory approaches the limit angle. This provides the AoA regulating controller with manageable initial state value. If the slew rate control strategy was omitted from the design, at the point of detection, the initial state condition will cause the closed loop AoA regulating control response to overshoot violently. Therefore by having the initial slew rate control stage, a model predictive element is included in the control design without the complication of a full model predictive controller.

### 6.1.1 Finite State Machine

As mentioned, these two stages operate as a finite state machine. With reference to Figure 3.10, this state machine will be located within the decision block  $W_{stall}$  and will function as the stall prevention control (SPC) block. The finite state machine will control the switching between the slew rate control stage (SRC) and AoA regulating control stage (AoARC) when the stall prevention control system is active. This state machine structure is presented in Figure 6.2 for the positive stall prevention case only.

While the stall prevention control algorithm is active, the NSA controller will be disconnected and in an open-loop configuration. It will still be excited by the normal specific reference input ( $C_{WR}$ ) provided by the outer loop guidance control systems, but the elevator output command will not be connected to the flight control system. The elevator command calculated by the control law of the open loop NSA controller, will indicate when it is safe to allow the flight control system to command the elevator. At any time during stall prevention control, if the elevator command from the NSA controller is less than the command provided by the stall prevention control sys-

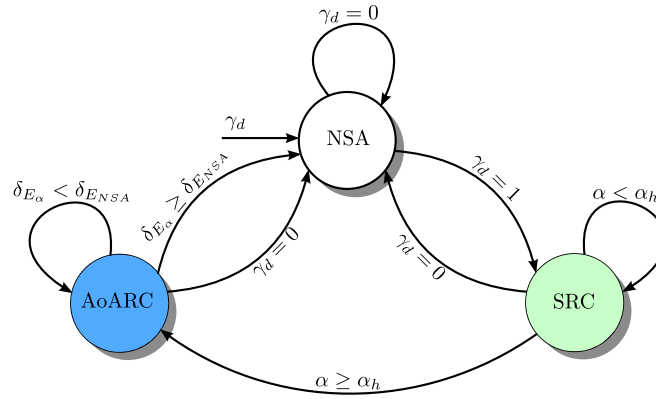


**Figure 6.2:** Stall prevention control finite state machine

tem, stall prevention will deactivate and allow the flight control system to function normally. At this time the NSA controller will be reinitialised at the current operating condition, reconnect in closed loop configuration and the detection algorithm will continue to monitor the state trajectories.

The section present the design and step response testing of the second control stage in the stall prevention control system.

## 6.2 AoA Reference Tracking Controller

The AoA controller is based on the same design principles as the normal specific acceleration controller described in §3.4.2. The controller will be designed to dynamically invert the gravity coupling term and provide enough degrees of freedom to allow for full placement of the closed loop poles. Thus, the feedback control law that will be used is defined below with reference to the conceptual block-diagram of the controller in Figure 6.3,

$$\delta_E = -K_\alpha \alpha - K_Q Q - K_E E_\alpha + \bar{N} \alpha_R + \delta_{di} \quad (6.1)$$

where,

$$\dot{E}_\alpha = \alpha - \alpha_R$$

The static offset terms, presented through the coefficients of zero-lift  $C_{L_0}$  and zero-moment  $C_{m_0}$ , will be omitted during this design since their only effect would be a constant steady state error in the response, thus adding no additional dynamics to the system. This steady state error however, will be eliminated by the augmented integrator state  $E_\alpha$ . Integrator dynamics are usually required to be fast enough not to influence the control response to the reference input. A feedforward term is therefore included in the control law to allow for the integrator dynamics to be slower. Furthermore, the integrator will be capable of removing the unwanted bias introduced by the gravity term, but only for small flight path angles. To ensure the gravity coupling is



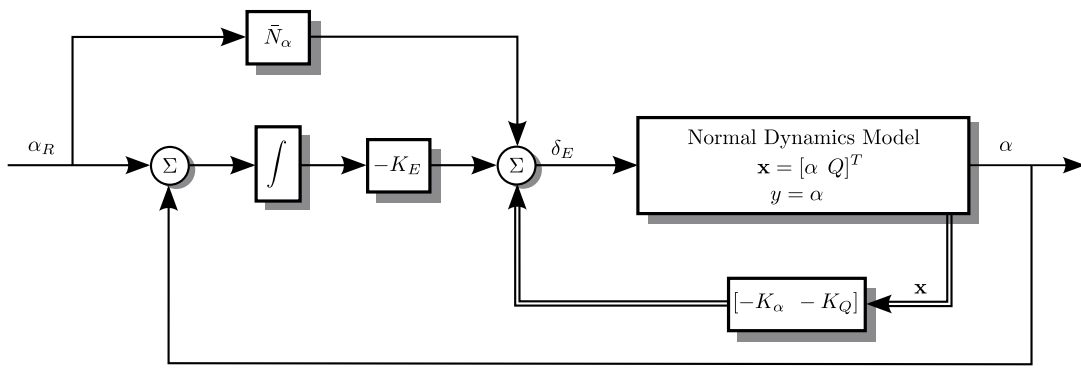


**Figure 6.3:** Angle of attack controller for the aircraft’s normal dynamics

eliminated at any gross attitude, thus allowing for full manoeuvrability, the elevator control input is used to dynamically invert this effect through the  $\delta_{di}$  term.

### 6.2.1 Controller Design

Through analysis it was found that the minimum phase (MP) zero that arise due to the transfer from elevator input to angle of attack output, is located at a very high frequency, hence it is a *fast LHP zero*. In general, zeros affect the transient response of a system by adding overshoot or undershoot, depending on its proximity to the stability boundary (imaginary axis) [18]. This minimum phase zero (due to its fast nature) can be assumed to be located at infinity. The effect of this approximation will be investigated through simulation. The pole and zero location for both the complete and simplified model dynamics are displayed in Figure 6.4 and Figure 6.5, as well as their respective bode plots.

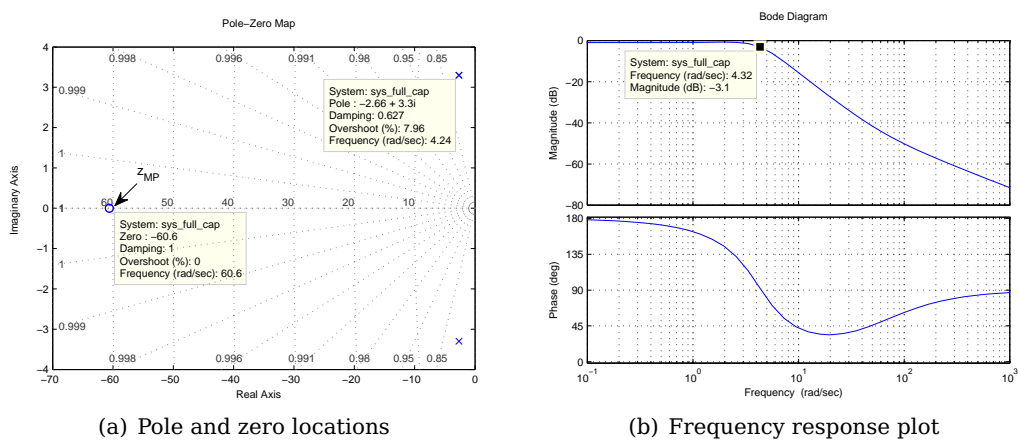


**Figure 6.4:** The poles and zeros from elevator to angle of attack for complete model

The effect of the minimum phase zero from elevator to angle of attack can therefore be neglected, allowing the normal dynamics model in Equation (3.19) to be simplified.

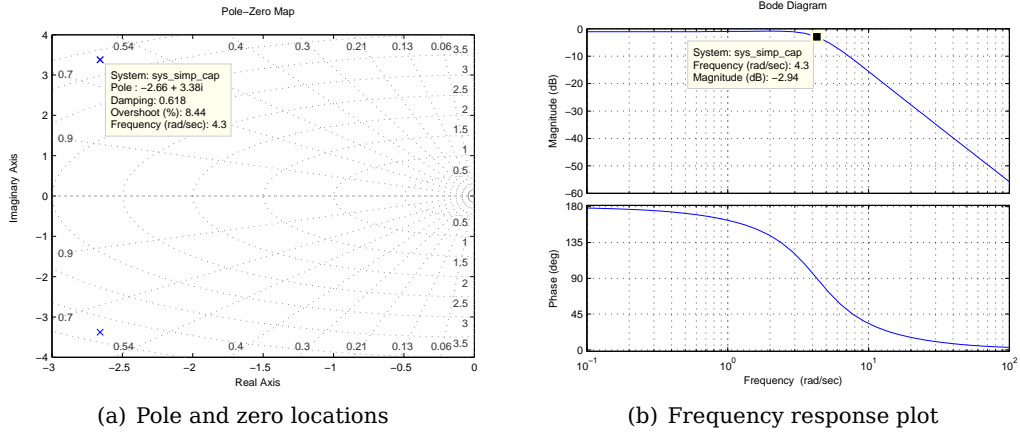


**Figure 6.5:** The poles and zeros from elevator to angle of attack for simplified model

Considering the characteristic equation for the zeros from elevator input to angle of attack output, yields the following expression,

$$z(s) = C \text{adj}(s\mathbf{I} - \mathbf{A}) \mathbf{B} + D \det(s\mathbf{I} - \mathbf{A}) \quad (6.2)$$

A standard assumption usually made to simplify the dynamics is the following,

$$\left| \frac{L_Q}{m\bar{V}} \right| \ll 1 \quad (6.3)$$

Note that this assumption is valid for nearly all aircraft [17]. Expanding Equation (6.2) and applying the above assumption gives,

$$\begin{aligned} z(s) &= \begin{bmatrix} 1 & 0 \end{bmatrix} \begin{bmatrix} s - \frac{M_Q}{I_{yy}} & 1 \\ \frac{M_\alpha}{I_{yy}} & s + \frac{L_\alpha}{m\bar{V}} \end{bmatrix} \begin{bmatrix} -\frac{L_{\delta_E}}{m\bar{V}} \\ \frac{M_{\delta_E}}{I_{yy}} \end{bmatrix} \\ &= \frac{L_{\delta_E}}{m} \left[ \left( \frac{L_\alpha}{m\bar{V}} \right) s + \left( \frac{L_\alpha}{m\bar{V}} \frac{M_Q}{I_{yy}} - \frac{M_{\delta_E}}{L_{\delta_E}} \frac{L_\alpha}{I_{yy}} \right) \right] \end{aligned} \quad (6.4)$$

To neglect the effect from the MP zero, the following simplification is made with reference to Equation (6.4),

$$C_{L_{\delta_E}} = 0 \quad (6.5)$$

This results in the simplified normal dynamics model presented in Equation (6.6), where the static terms have been omitted.

$$\begin{bmatrix} \dot{\alpha} \\ \dot{Q} \end{bmatrix} = \begin{bmatrix} -\frac{L_\alpha}{m\bar{V}} & 1 \\ \frac{M_\alpha}{I_{yy}} & \frac{M_Q}{I_{yy}} \end{bmatrix} \begin{bmatrix} \alpha \\ Q \end{bmatrix} + \begin{bmatrix} 0 \\ \frac{M_{\delta_E}}{I_{yy}} \end{bmatrix} \delta_E + \begin{bmatrix} \frac{g}{\bar{V}} \\ 0 \end{bmatrix} e_{33}^{WI} \quad (6.6)$$

This simplification does not affect the pole locations from elevator input to angle of attack output as proved in Figure 6.5. This allows for the following derivation of the dynamic inversion term, starting with the simplified angle of attack dynamic equation,

$$\dot{\alpha} = \left( -\frac{L_\alpha}{m\bar{V}} \right) \alpha + (1) Q + \frac{g}{\bar{V}} e_{33}^{WI} \quad (6.7)$$

Differentiating this equation once with respect to time and recalling that the coefficients of the terms are constant due to either the time scale separation condition or their static nature, yields the following after substitution from the simplified pitch rate dynamic equation,

$$\begin{aligned} \ddot{\alpha} &= \left( -\frac{L_\alpha}{m\bar{V}} \right) \dot{\alpha} + \dot{Q} + \frac{g}{\bar{V}} \dot{e}_{33}^{WI} \\ &= \left( -\frac{L_\alpha}{m\bar{V}} \right) \dot{\alpha} + \left( \frac{M_\alpha}{I_{yy}} \right) \alpha + \left( \frac{M_Q}{I_{yy}} \right) Q + \left( \frac{M_{\delta_E}}{I_{yy}} \right) \delta_E + \frac{g}{\bar{V}} \dot{e}_{33}^{WI} \end{aligned} \quad (6.8)$$

Substituting the control law expressed in Equation (6.1) into the above result, yields,

$$\begin{aligned} \ddot{\alpha} &= \left( -\frac{L_\alpha}{m\bar{V}} \right) \dot{\alpha} + \left( \frac{M_\alpha}{I_{yy}} - K_\alpha \frac{M_{\delta_E}}{I_{yy}} \right) \alpha + \left( \frac{M_Q}{I_{yy}} - K_Q \frac{M_{\delta_E}}{I_{yy}} \right) Q \\ &\quad + \left( -K_E \frac{M_{\delta_E}}{I_{yy}} \right) E_\alpha + \left( \bar{N} \frac{M_{\delta_E}}{I_{yy}} \right) \alpha_R + \left( \frac{M_{\delta_E}}{I_{yy}} \right) \delta_{di} + \frac{g}{\bar{V}} \dot{e}_{33}^{WI} \end{aligned} \quad (6.9)$$

At this stage, the elevator command can be used to remove the effect of the gravity coupling terms. However, upon analysis of Equation (6.7), the gravity coupling will be reintroduced by the  $Q$  term, since the feedback control law makes use of pitch rate feedback. To eliminate the  $Q$  term, Equation (6.7) is rewritten with  $Q$  as the subject of the expression and then substituted into the above result to give,

$$\begin{aligned} \ddot{\alpha} &= \left( \frac{M_Q}{I_{yy}} - K_Q \frac{M_{\delta_E}}{I_{yy}} - \frac{L_\alpha}{m\bar{V}} \right) \dot{\alpha} + \left( \frac{M_\alpha}{I_{yy}} - K_\alpha \frac{M_{\delta_E}}{I_{yy}} + \frac{M_Q}{I_{yy}} \frac{L_\alpha}{m\bar{V}} - K_Q \frac{M_{\delta_E}}{I_{yy}} \frac{L_\alpha}{m\bar{V}} \right) \alpha \\ &\quad + \left( -K_E \frac{M_{\delta_E}}{I_{yy}} \right) E_\alpha + \left( \bar{N} \frac{M_{\delta_E}}{I_{yy}} \right) \alpha_R + \left( \frac{M_{\delta_E}}{I_{yy}} \right) \delta_{di} \\ &\quad + \frac{g}{\bar{V}} \dot{e}_{33}^{WI} + \left( \frac{M_Q}{I_{yy}} - K_Q \frac{M_{\delta_E}}{I_{yy}} \right) \frac{g}{\bar{V}} e_{33}^{WI} \end{aligned} \quad (6.10)$$

The angle of attack closed loop dynamics will then become,

$$\begin{aligned} \ddot{\alpha} &= \left( \frac{M_Q}{I_{yy}} - K_Q \frac{M_{\delta_E}}{I_{yy}} - \frac{L_\alpha}{m\bar{V}} \right) \dot{\alpha} + \left( \frac{M_\alpha}{I_{yy}} - K_\alpha \frac{M_{\delta_E}}{I_{yy}} + \frac{M_Q}{I_{yy}} \frac{L_\alpha}{m\bar{V}} - K_Q \frac{M_{\delta_E}}{I_{yy}} \frac{L_\alpha}{m\bar{V}} \right) \alpha \\ &\quad + \left( -K_E \frac{M_{\delta_E}}{I_{yy}} \right) E_\alpha + \left( \bar{N} \frac{M_{\delta_E}}{I_{yy}} \right) \alpha_R \end{aligned} \quad (6.11)$$

with,

$$\dot{E}_\alpha = \alpha - \alpha_R \quad (6.12)$$

when,

$$\left(\frac{M_{\delta_E}}{I_{yy}}\right) \delta_{di} + \frac{g}{\bar{V}} \dot{e}_{33}^{WI} + \left(\frac{M_Q}{I_{yy}} - K_Q \frac{M_{\delta_E}}{I_{yy}}\right) \frac{g}{\bar{V}} e_{33}^{WI} = 0$$

Therefore the dynamic inversion part of the control law takes the form,

$$\begin{aligned} \delta_{di} &= \left(\frac{I_{yy} g}{M_{\delta_E} \bar{V}}\right) \left(\dot{e}_{33}^{WI} + \left(\frac{M_Q}{I_{yy}} - K_Q \frac{M_{\delta_E}}{I_{yy}}\right) e_{33}^{WI}\right) \\ &= \left(\frac{I_{yy} g}{M_{\delta_E} \bar{V}}\right) \left[\left(\frac{C_W + e_{33}^{WI} g}{\bar{V}}\right) e_{13}^{WI} + P_W e_{23}^{WI} + \left(\frac{M_Q}{I_{yy}} - K_Q \frac{M_{\delta_E}}{I_{yy}}\right) e_{33}^{WI}\right] \end{aligned} \quad (6.13)$$

With the dynamic inversion control law in place, the focus can now shift towards solving the feedback gains of the closed loop system. This is achieved by deriving the characteristic equation of the closed loop angle of attack dynamics and then comparing the coefficients of this polynomial to those of the desired characteristic equation for the closed loop system.

Taking Equation (6.11) and writing it in state space form gives,

$$\begin{aligned} \mathbf{x} &= \begin{bmatrix} \dot{\alpha} & \alpha & E_\alpha \end{bmatrix}^T \quad r = \alpha_R \\ \dot{\mathbf{x}} &= \hat{\mathbf{A}}\mathbf{x} + \hat{\mathbf{B}}r \end{aligned} \quad (6.14)$$

where,

$$\hat{\mathbf{A}} = \begin{bmatrix} \left(\frac{M_Q}{I_{yy}} - K_Q \frac{M_{\delta_E}}{I_{yy}} - \frac{L_\alpha}{m\bar{V}}\right) & \left(\frac{M_\alpha}{I_{yy}} - K_\alpha \frac{M_{\delta_E}}{I_{yy}} + \frac{M_Q L_\alpha}{I_{yy} m\bar{V}} - K_Q \frac{M_{\delta_E} L_\alpha}{I_{yy} m\bar{V}}\right) & \left(-K_E \frac{M_{\delta_E}}{I_{yy}}\right) \\ 1 & 0 & 0 \\ 0 & 1 & 0 \end{bmatrix}$$

$$\hat{\mathbf{B}} = \begin{bmatrix} \left(\bar{N} \frac{M_{\delta_E}}{I_{yy}}\right) \\ 0 \\ -1 \end{bmatrix}$$

The characteristic equation of the closed loop system can be derived by solving the following equation, with  $\mathbf{I}$  the identity matrix,

$$\lambda_c(s) = |s\mathbf{I} - \hat{\mathbf{A}}| \quad (6.15)$$

However, since  $\hat{\mathbf{A}}$  is in *control canonical* form, the closed loop characteristic equation

can be derived from inspection as,

$$\begin{aligned} \lambda_c(s) = & s^3 + \left( \frac{M_Q}{I_{yy}} - K_Q \frac{M_{\delta_E}}{I_{yy}} - \frac{L_\alpha}{m\bar{V}} \right) s^2 \\ & + \left( \frac{M_\alpha}{I_{yy}} - K_\alpha \frac{M_{\delta_E}}{I_{yy}} + \frac{M_Q}{I_{yy}} \frac{L_\alpha}{m\bar{V}} - K_Q \frac{M_{\delta_E}}{I_{yy}} \frac{L_\alpha}{m\bar{V}} \right) s + \left( -K_E \frac{M_{\delta_E}}{I_{yy}} \right) \end{aligned} \quad (6.16)$$

With the desired characteristic equation describing the locations of the closed loop poles for the angle of attack dynamics defined as,

$$\lambda_d(s) = s^3 + \gamma_2 s^2 + \gamma_1 s + \gamma_0 \quad (6.17)$$

Matching the coefficients between the two characteristic polynomials and solving for the control law feedback gains yields,

$$\gamma_2 = \left( \frac{M_Q}{I_{yy}} - K_Q \frac{M_{\delta_E}}{I_{yy}} - \frac{L_\alpha}{m\bar{V}} \right) \quad (6.18)$$

$$\gamma_1 = \left( \frac{M_\alpha}{I_{yy}} - K_\alpha \frac{M_{\delta_E}}{I_{yy}} + \frac{M_Q}{I_{yy}} \frac{L_\alpha}{m\bar{V}} - K_Q \frac{M_{\delta_E}}{I_{yy}} \frac{L_\alpha}{m\bar{V}} \right) \quad (6.19)$$

$$\gamma_0 = \left( -K_E \frac{M_{\delta_E}}{I_{yy}} \right) \quad (6.20)$$

Thus,

$$K_\alpha = \frac{I_{yy}}{M_{\delta_E}} \left( \gamma_1 + \frac{M_\alpha}{I_{yy}} - \frac{L_\alpha}{m\bar{V}} \gamma_2 + \left( \frac{L_\alpha}{m\bar{V}} \right)^2 \right) \quad (6.21)$$

$$K_Q = \frac{I_{yy}}{M_{\delta_E}} \left( \gamma_2 + \frac{M_Q}{I_{yy}} - \frac{L_\alpha}{m\bar{V}} \right) \quad (6.22)$$

$$K_E = \frac{I_{yy}}{M_{\delta_E}} (\gamma_0) \quad (6.23)$$

with,

$$\bar{N} = -\frac{K_E}{z_I} \quad (6.24)$$

where  $z_I$  is the location of the zero introduced by the feedforward gain. Usual design practice dictates that the location of the feedforward zero is to be chosen to coincide with the location of the pole from the augmented integrator state. In theory this cancels the effect induced by the integrator dynamics on the closed loop response. However, this is not always the case in a practical system, therefore the integrator dynamics and feedforward gain needs to be chosen with this in mind.

Substituting the feedback gain  $K_Q$  into the dynamic inversion control law of Equation (6.13) gives,

$$\delta_{di} = \left( \frac{I_{yy} g}{M_{\delta_E} \bar{V}} \right) \left[ \left( \frac{C_W + e_{33}^{WI} g}{\bar{V}} \right) e_{13}^{WI} + P_W e_{23}^{WI} + \left( -\gamma_2 + \frac{L_\alpha}{m \bar{V}} \right) e_{33}^{WI} \right] \quad (6.25)$$

The following section is aimed at investigating allowable closed loop pole placement options to satisfy the flight control system's design constraints and to ensure desirable closed loop response characteristics.

### 6.2.2 Linear Closed Loop Analysis and Pole Placement

Since the angle of attack tracking controller is a substitute for the normal specific acceleration controller during stall prevention, it is subjected to the same time scale separation lower frequency bound in the sense of innerloop control. As previously discussed in Chapter 3, this lower frequency bound is determined by the desired velocity magnitude bandwidth  $\omega_v$  in the outerloop control. Upon analysis of the longitudinal transfer function from elevator displacement to forward velocity, this bandwidth is typically less than 1 rad/s. According to the time scale separation principal, the lower frequency bound should be five times greater than this.

The maximum bandwidth achievable by the closed loop controller is not limited by any non-minimum phase constraint, but it is however limited by the actual achievable servo response. For the stall detection algorithm and the slew rate control phase, the slew rate parameter chosen is a conservative value compared to what is actually achievable by the servos of the elevator actuator. This creates a *buffer of safety* against model uncertainties. In order to choose suitable closed loop pole locations, the actual slew rate of the servos needs to be calculated. According to [20], the servos can be modelled as a simple low-pass filter with a cut-off frequency chosen based on the slew rate limit given in the servo specification sheet. To relate the slew rate of the servo horn to the actual control surface deflection rate, the following expression is used,

$$\omega_c = \frac{\dot{\delta}_{sr}}{A} \quad (6.26)$$

when  $\dot{\delta}_{sr}$  is the slew rate limit and  $A$  is the magnitude of the servo arm deflection,  $\omega_c$  becomes the maximum servo bandwidth.

For typical servos used with unmanned aerial vehicle projects, the flowing upper frequency bound is calculated for the elevator actuator with saturation limits at  $\pm 14^\circ$ ,

$$\omega_c = \frac{260^\circ/s}{2(14^\circ)} = 9.286 \text{ rad.s}^{-1} \quad (6.27)$$

Therefore the bandwidth constraints imposed on the placement of the closed loop poles are,

$$5\omega_v < \omega_{n_{CL}} < \omega_c$$

The open loop short period mode poles during trimmed flight are located at an undamped natural frequency of  $4.24 \text{ rad.s}^{-1}$ . Since the controller should operate effectively over the aircraft's full range of specified velocities<sup>1</sup>, the closed loop pole locations should be chosen with this in mind. The closed loop short period mode poles were chosen at a slightly higher bandwidth of  $6 \text{ rad.s}^{-1}$ , which coincides with the undamped natural frequency of the open loop short period mode poles at the maximum allowed velocity. This is located well within the frequency bounds discussed here and do not severely strain the amount of control input required by the controller. Since the slew rate control phase ensures desirable initial conditions for the angle of attack tracking controller, the damping of the closed loop poles were chosen to be optimal ( $\zeta = 0.707$ ) to achieve the desired control response.

Consider the following step response analysis, for the closed loop control system conducted on the complete and simplified normal dynamics models, in Figure 6.6.

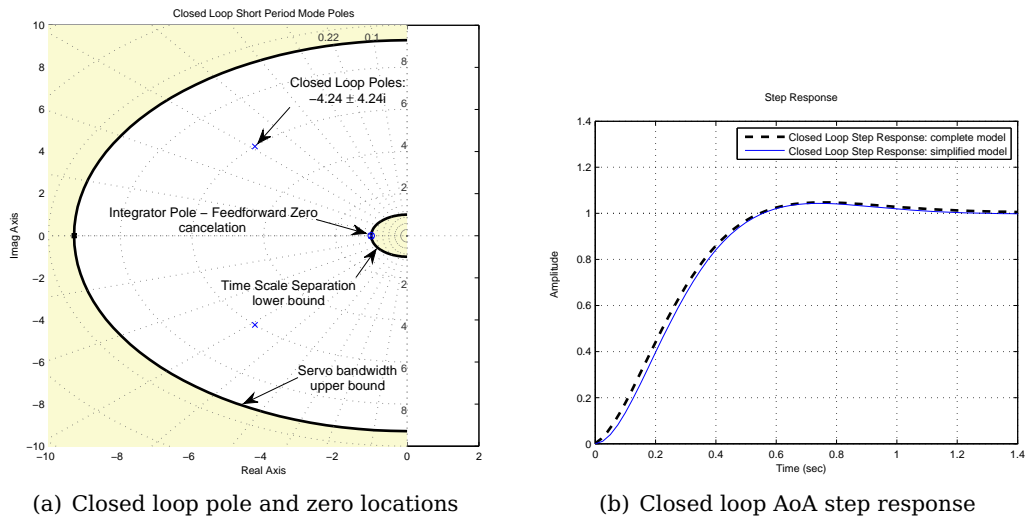


**Figure 6.6:** Closed loop angle of attack step response on both the complete and simplified normal dynamics models

Both step response simulations were conducted with the slew rate and saturation nonlinearities of the elevator command taken into account. Notice the negligible difference in the respective transient responses caused by the minimum phase zero approximation. There is no significant change in the damping for the closed loop step

<sup>1</sup>The specified range of velocities for this particular UAV range from a minimum  $\bar{V} = 17 \text{ m/s}$  to a maximum  $\bar{V} = 30 \text{ m/s}$ .

response with the complete normal dynamics model as compared to the designed damping with the simplified model.

As discussed earlier, the feedforward gain  $\bar{N}$  allows zero steady state error tracking with slower integrator dynamics. The effect of including the feedforward term is presented in Figure 6.7 when complete pole-zero cancellation is achieved.

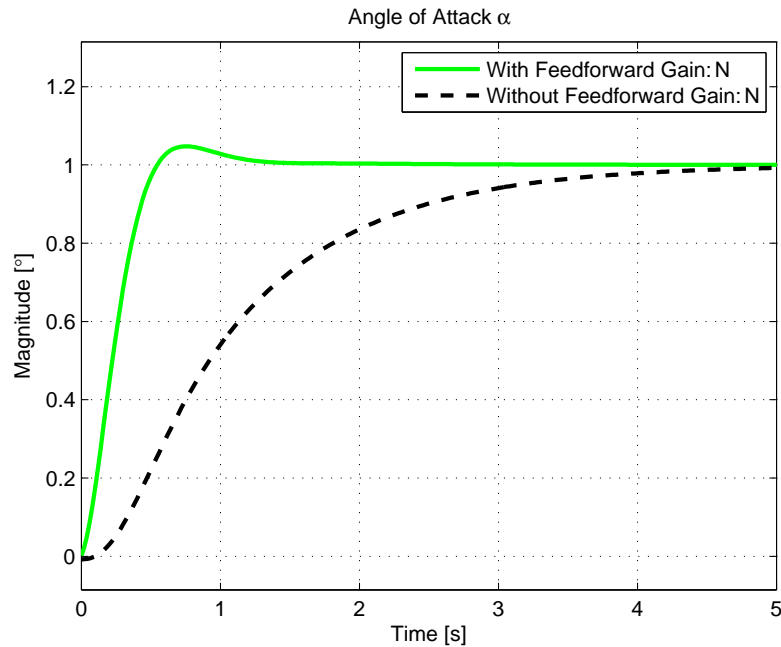


**Figure 6.7:** Effect of feedforward gain on the closed loop AoA step response

In practice however, the integrator pole and feedforward zero will not entirely cancel, resulting in slower error dynamics which in turn could lead to increased overshoot in the closed loop. Therefore, care should be taken not to provide excessive feedforward due to model inaccuracies.

Another implication on practical implementation exists, in the form of system delays and anti-windup that needs to be considered in the closed loop analysis. This will be addressed in the following section.

### 6.2.3 System Delays and Anti-Windup

The digital flight control system used for this aerial vehicle operates at a sampling rate of 50Hz. The flight control system utilises a full sample period to calculate the appropriate elevator command based on the state measurements ( $\alpha$  and  $Q$ ) taken at the start of the current sample. Therefore a delay is present in the system, between the measurements and the command output.



The aircraft’s normal dynamics operate at a frequency at least 30 times less than the sampling rate of the flight control system, a digital implementation of the continuous closed loop angle of attack controller can then be designed accurately through *emulation* [23]. This allows the controller to be designed in the continuous-time domain and transformed to the discrete-time domain.

Analysing the system delay in the discrete-time domain with the discretised control law, yields the results presented in Figure 6.8 for a closed loop step response.

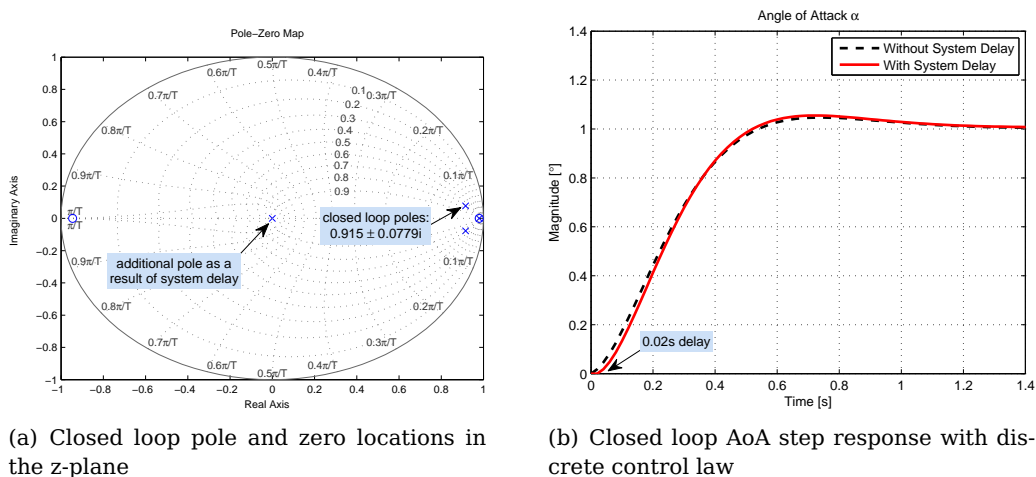


**Figure 6.8:** Closed loop angle of attack step response displaying the effect of a system delay

The closed loop step response in Figure 6.8 was conducted on the complete normal dynamics model with the system delay and the actuator nonlinearities included in the simulation. The one sample period time delay in the step response caused a slight increase in the designed overshoot. Due to the fast sample rate of the flight control system, the delay is not significant to cause undesirable closed loop response or instability. However, combined with model uncertainty related to the feedforward zero placement and sensor noise, the effect induced by the system delay could become significant.

An ever present problem in control is that all real actuators have limited authority which implies that they are physically constrained in amplitude and/or rate of change. Therefore, if the desired elevator input signal is denoted by  $\hat{\delta}_E(t)$  and the actual elevator signal is denoted by  $\delta_E(t)$  then the saturation can be described as follows,

$$\delta_E(t) = \mathbf{Sat} \left\langle \hat{\delta}_E(t) \right\rangle \triangleq \begin{cases} \delta_{E_{max}} & \text{if } \hat{\delta}_E(t) > \delta_{E_{max}} \\ \hat{\delta}_E(t) & \text{if } \delta_{E_{min}} \leq \hat{\delta}_E(t) \leq \delta_{E_{max}} \\ \delta_{E_{min}} & \text{if } \hat{\delta}_E(t) < \delta_{E_{min}} \end{cases} \quad (6.28)$$

When the elevator input command reaches an amplitude limit (positive or negative deflection limit) the integrator in the control law will continue to integrate due to the error signal between the desired and achievable angle of attack. This is known as *wind-up*. The integrator state can therefore reach unacceptably high values which will result in a unwanted transient response when this accumulated energy is released. Control systems usually handle this important problem by adding *anti-wind-up* mechanisms to the compensator design. The angle of attack tracking control systems handles this problem by keeping the integrator state constant while the elevator input signal is saturated. Therefore effectively turning the integrator off and reducing the control law to a proportional feedback law during elevator saturation, thus preventing any unwanted transients.

### 6.3 Summary

The AoA regulating control system was successfully designed in this chapter. It produced the desired closed loop characteristic during the step response analyses, even with the added system nonlinearities. With all the aspects of the stall prevention control system in place, the next step is to investigate its performance through simulation.

The complete stall prevention control system developed in this project will be analysed through linear and nonlinear simulations in the following chapter. This will verify the operational functionality of this stall prevention control strategy and will highlight any shortcomings or weaknesses.

## Chapter 7

# Simulation and Analysis

The following simulations are setup to allow the normal specific acceleration reference command  $C_{W_R}$  (usually provided by the outerloop guidance controller) to be commanded manually. This is achieved through either a pre-generated signal or pilot input. The elevator command is then calculated using the control law expressed in Equation (3.21) for the normal specific acceleration controller. Therefore the pilot effectively flies the aircraft through the innerloop NSA controller. During this time, the detection algorithm will continuously monitor the normal dynamics states and will activate the stall prevention control system based on the stall detection principle defined in Chapter 4.

### 7.1 Linear Simulation

For this simulation, a pre-generated  $C_{W_R}$  signal was used to ensure consistent results during multiple simulation attempts. The elevator signal calculated using the NSA control law, is provided as input to the linear normal dynamics model. Note however, that both the system delay and the actuator nonlinearities are included in this simulation. The stall prevention control system is allowed to override the elevator input signal once activated by the detection algorithm.

Consider the results presented in Figure 7.1 obtained when the pilot attempted to pull-up to steeply, causing the angle of attack to approach the stall angle.

During this linear simulation the air velocity and flight path angle are assumed constant. The markers in the figures indicate the detection onset point and the switch point from slew rate control to AoA tracking control as 1 and 2 respectively. Notice the early detection due to the moderately high pitch rate manoeuvre. The slew rate control is immediately applied after detection, thus overriding the elevator command as seen in Figure 7.1(a). This forces the normal dynamics states to track the best possible trajectory to prevent the angle of attack from exceeding the limit angle. This

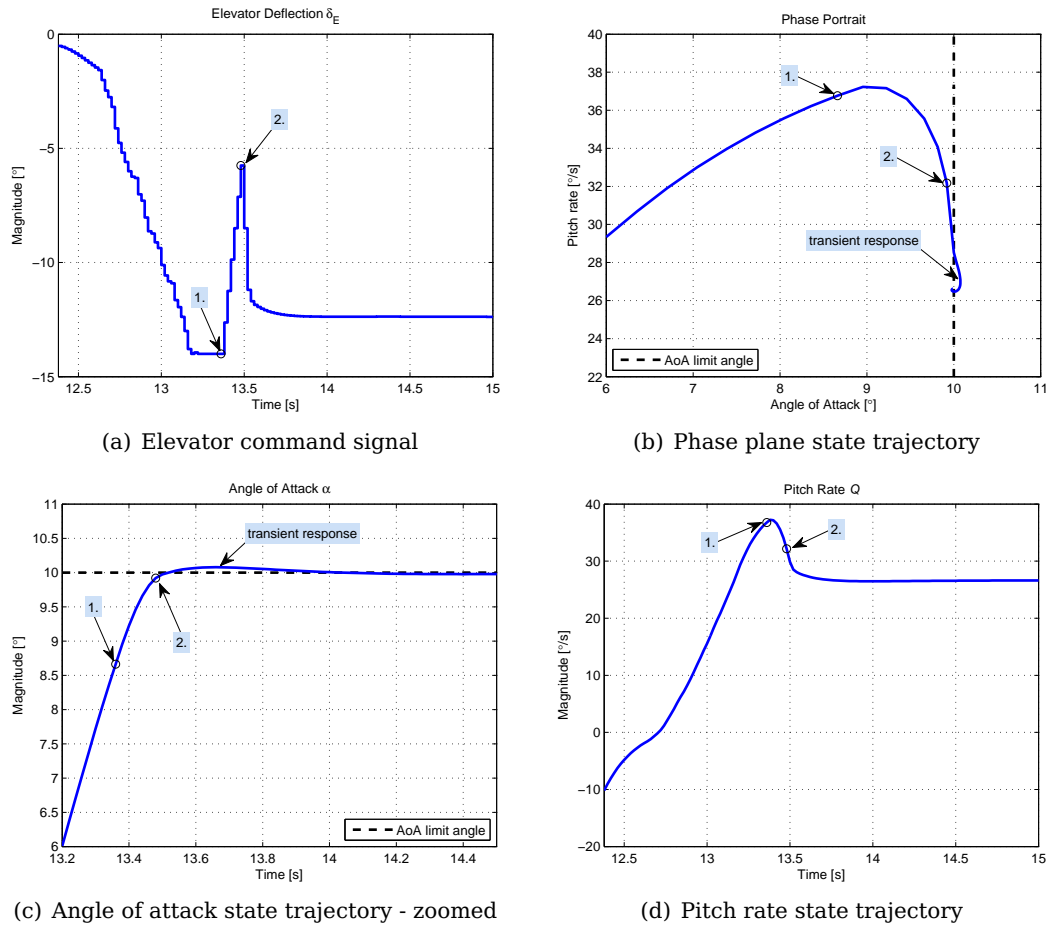


**Figure 7.1:** Linear simulation results

reduces the pitch rate and absorbs some of the energy from the manoeuvre, thus providing acceptable state values to initialise the AoA tracking controller at 2. The AoA tracking controller immediately reacts to constrain the angle of attack and regulate it to the limit angle, resulting in a small transient caused by the overshoot from the response.

This verifies the combined operation and functionality of the control strategy and its feasibility to prevent the occurrence of aerodynamic stall by limiting the angle of attack to an acceptable maximum (or minimum for negative stall prevention) angle.

The next simulation analyses the stall prevention control system response on the full nonlinear six-degrees-of-freedom aircraft model in the presence of realistic sensor noise.

## 7.2 Nonlinear SIL Simulation

The full nonlinear aircraft model, consisting of all the inner and outer loop dynamics, as presented in Figure 3.5, was used to create a virtual aircraft simulation environment in *Matlab* via *Simulink*. This allows the controllers designed in this project to be evaluated against a relatively accurate testbed by conducting *software-in-the-loop* (SIL) simulations to analyse their performance in the presence of system noise and nonlinearities.

Noise models for the different sensors used by the virtual aircraft, were based on real-world sensors by consulting their respective data sheets and acquiring realistic noise values. For the accelerometers and rate gyroscope sensors, noise induced by the vibration from the aircraft's engine were also accounted for. The noise model adopted for the angle of attack sensor is presented in Table 7.1 and is based on a typical vane sensor [24].

| Angle of Attack Range                | Noise Values     |
|--------------------------------------|------------------|
| $19^\circ \leq \alpha \leq 45^\circ$ | $\pm 0.35^\circ$ |
| $10^\circ \leq \alpha \leq 18^\circ$ | $\pm 0.15^\circ$ |
| $5^\circ \leq \alpha < 10^\circ$     | $\pm 0.10^\circ$ |
| $3^\circ \leq \alpha < 5^\circ$      | $\pm 0.15^\circ$ |
| $-30^\circ \leq \alpha < 3^\circ$    | $\pm 0.35^\circ$ |

**Table 7.1:** The accuracy of a typical AoA vane sensor

In addition, the SIL simulation also includes a graphical output, which visually displays the aircraft and its flight trajectories in real time. This allows for more effective analysis through visual perception of the virtual flight simulation. This graphical output was originally developed by [25] and later improved by [26]. Figure 7.2 displays a screen print of the latest version of this graphical output displaying a model of the UAV used during this project.

This SIL simulation will validate any simplifications and approximations made during the development of the aircraft model and the design of the controllers. It will also verify the assumptions made regarding the gravity coupling during the development of the detection algorithm.

The velocity magnitude is not a constant parameter in this full nonlinear environment, therefore it is rather cumbersome to test the stall prevention control system without violating the stall speed during flight manoeuvres. This could be overcome by including some form of a *thrust recovery control system*<sup>1</sup>. Therefore the thrust had to be maintained manually during these simulations. Two tests were chosen to demonstrate

<sup>1</sup>This will be discussed in the recommendations section in Chapter 8.

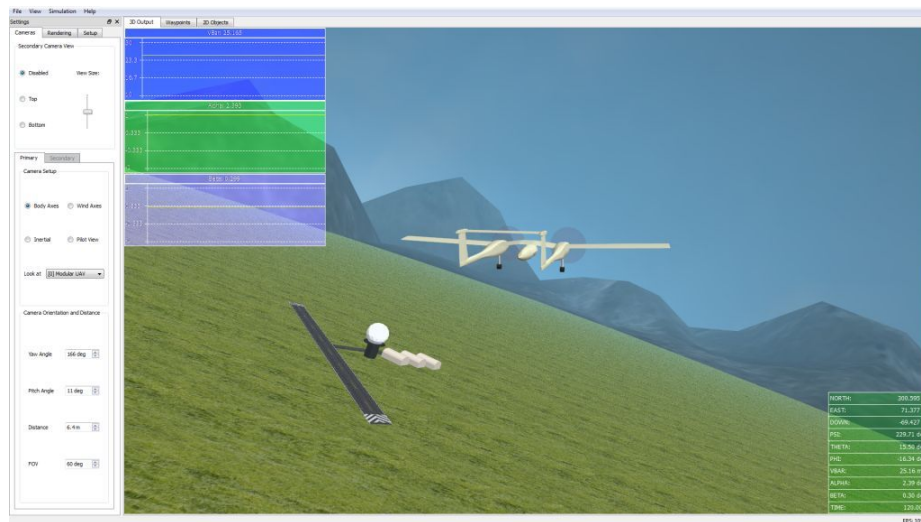


**Figure 7.2:** Virtual aircraft simulation graphical output

the operation and performance of the stall prevention control system. These include a slow speed flight test and a steep pull-up flight test. For these simulations, the  $C_{W_R}$  signal was commanded by a pilot through a joystick. The results from the two respective test simulations are now presented.

### 7.2.1 Slow Speed Flight

The first simulation was conducted with the thrust setting at its minimum, while the reference normal specific acceleration was held at 1g. This input caused the aircraft to slow down resulting in an increase in angle of attack to maintain the reference command of straight and level flight. Due to the high aspect ratio rectangular wing of the aircraft it has good gliding capabilities. Therefore the aircraft reached an equilibrium velocity greater than the stall speed, at an angle of attack less than the critical angle but close to the predefined limit angle. The aircraft thus descended, wings-level at a steady rate.

The pilot then commands additional  $C_{W_R}$  to pitch the nose up in an attempt to exceed the predefined maximum angle of attack limit of  $10^\circ$ . The results for this simulation, is presented in Figure 7.3.

With the marker definitions the same as before, in Figure 7.3 the stall prevention control system activates at 1 and control the slew rate of the elevator to allow the angle of attack to gradually reach the limit angle. As soon as the angle of attack reaches the threshold angle, the AoA regulating controller initialises and constrains the angle of attack to the predefined limit angle. The additional noise on the elevator signal during this stage was found to be caused by the feedforward term. Upon analysis, the feedforward term did not entirely cancel the effect of the slow integrator pole at

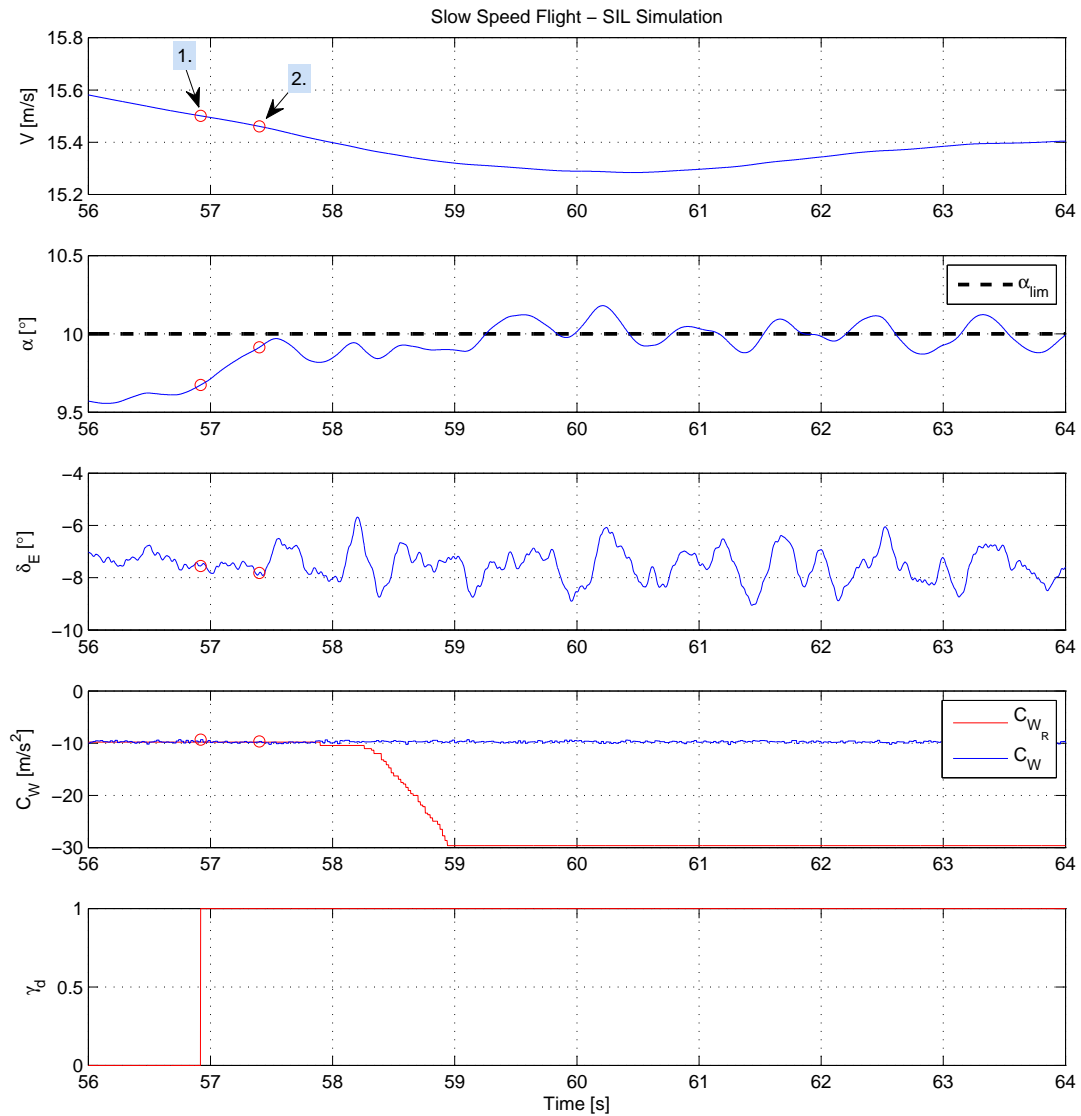


**Figure 7.3:** Nonlinear slow speed flight simulation results

this slow air velocity. This affected the error dynamics of the control system and as a result, allowed the angle of attack sensor noise to influence the closed loop response. This was amplified by the 20 ms system delay of the flight control system.

However, even with this added noise, the AoA regulating control system regulates the angle of attack at the limit angle within an acceptable margin of  $\pm 0.2^\circ$ . After the stall prevention control system is activated, the pilot commands additional normal specific acceleration at  $t = 58$  s in an attempt to stall the aircraft. The AoA regulating controller continues to constrain the angle of attack without being influenced by this command. To prevent the integrators in the flight control system from winding up, flags are set in the climb rate control loop and NSA control system to activate their respective anti-windup mechanisms during stall prevention control.

This type of flight condition also applies well during autonomous landing procedures,

as discussed during the literature study in Chapter 2. The stall prevention control strategy proves effective in overriding the elevator command and preventing the angle of attack from exceeding the predefined limit angle during slow flight manoeuvres.

### 7.2.2 Steep Pull-up

The next simulation tests the stall prevention control strategy against steep pull-up manoeuvres, similar to what can be expected in the event of a secondary stall or steep climb. For this simulation the thrust was held constant at its trim setting, the pilot then commanded negative-g to put the aircraft in a short dive and followed with strong positive-g to pull up steeply. The resulting response of the stall prevention control system, is displayed in Figure 7.5.

With reference to the stall detection envelope, the algorithm detects stall at a relatively early angle at  $t = 5.36$  s, due to this high pitch rate manoeuvre. Notice that the threshold angle is reached rather quickly between markers 1 and 2. As a result, the slew rate control stage had sufficient time to limit the pitch rate as presented in Figure 7.4, but due to the system delay, was unable to provide the AoA regulating controller with desirable initial state values. As a result, unexpected overshoot is exhibited in the transient response.

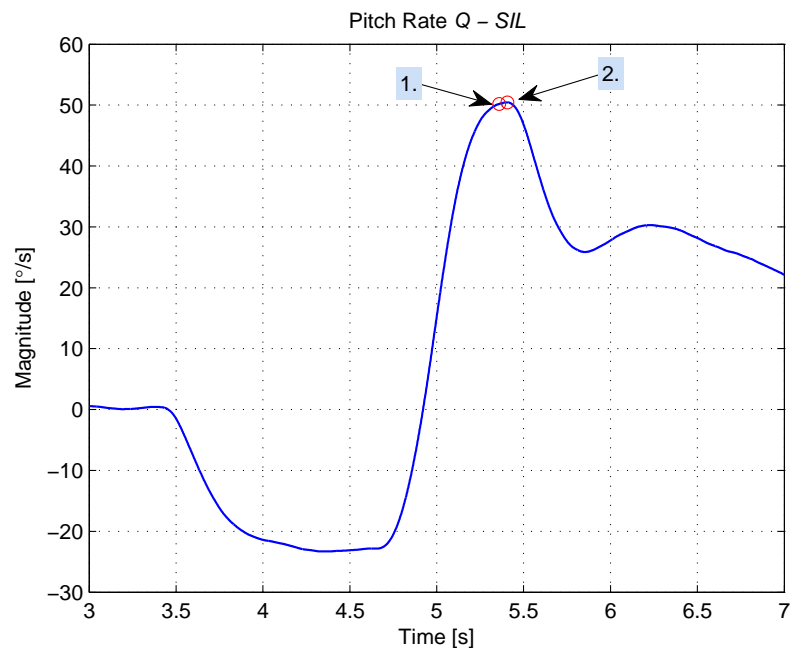


**Figure 7.4:** Nonlinear step pull-up simulation results for the pitch rate

Due to the stable airframe of this aerial vehicle, this excessively steep manoeuvre was the only method by which the performance of the stall prevention control system



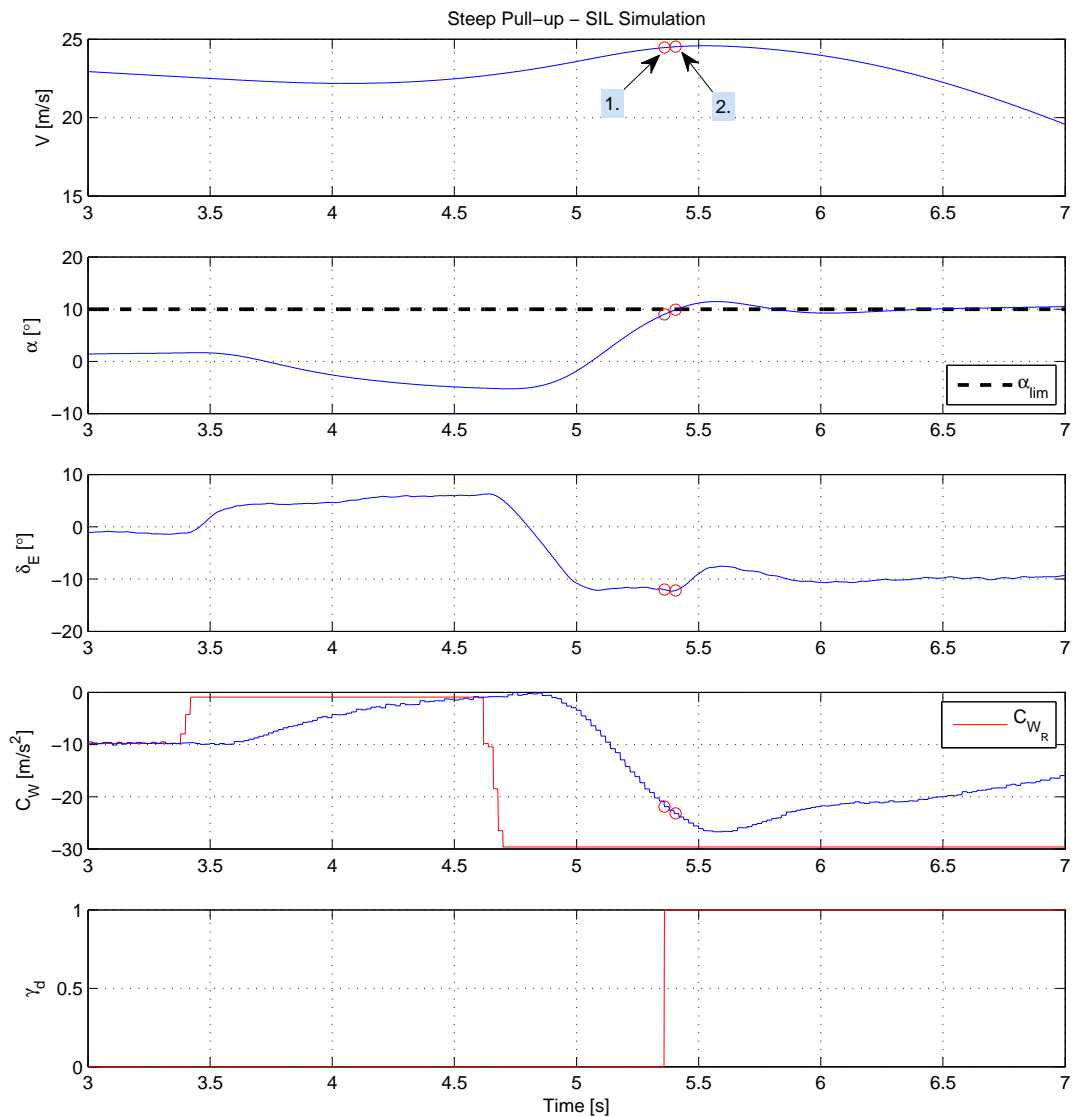


**Figure 7.5:** Nonlinear step pull-up simulation results

could be tested and analysed. Note that during autonomous flight for this type of aerial vehicle, the control commands would rarely enforce such aggressive manoeuvres. However, from Figure 7.5 it is clear that the stall prevention control system proved effective in constraining the angle of attack and limiting the normal specific acceleration.

### 7.2.3 Reactivating the NSA Control System

The NSA control system will be allowed to function in closed loop form once the required normal specific acceleration  $C_{WR}$  is less than what is allowed by the stall prevention control system. Therefore, once the elevator command calculated by the NSA control law is less than the elevator command applied by the AoA regulating

control law, normal unconstrained flight control will resume.

Consider the results of such a typical reactivation of the NSA control system presented in Figure 7.6.

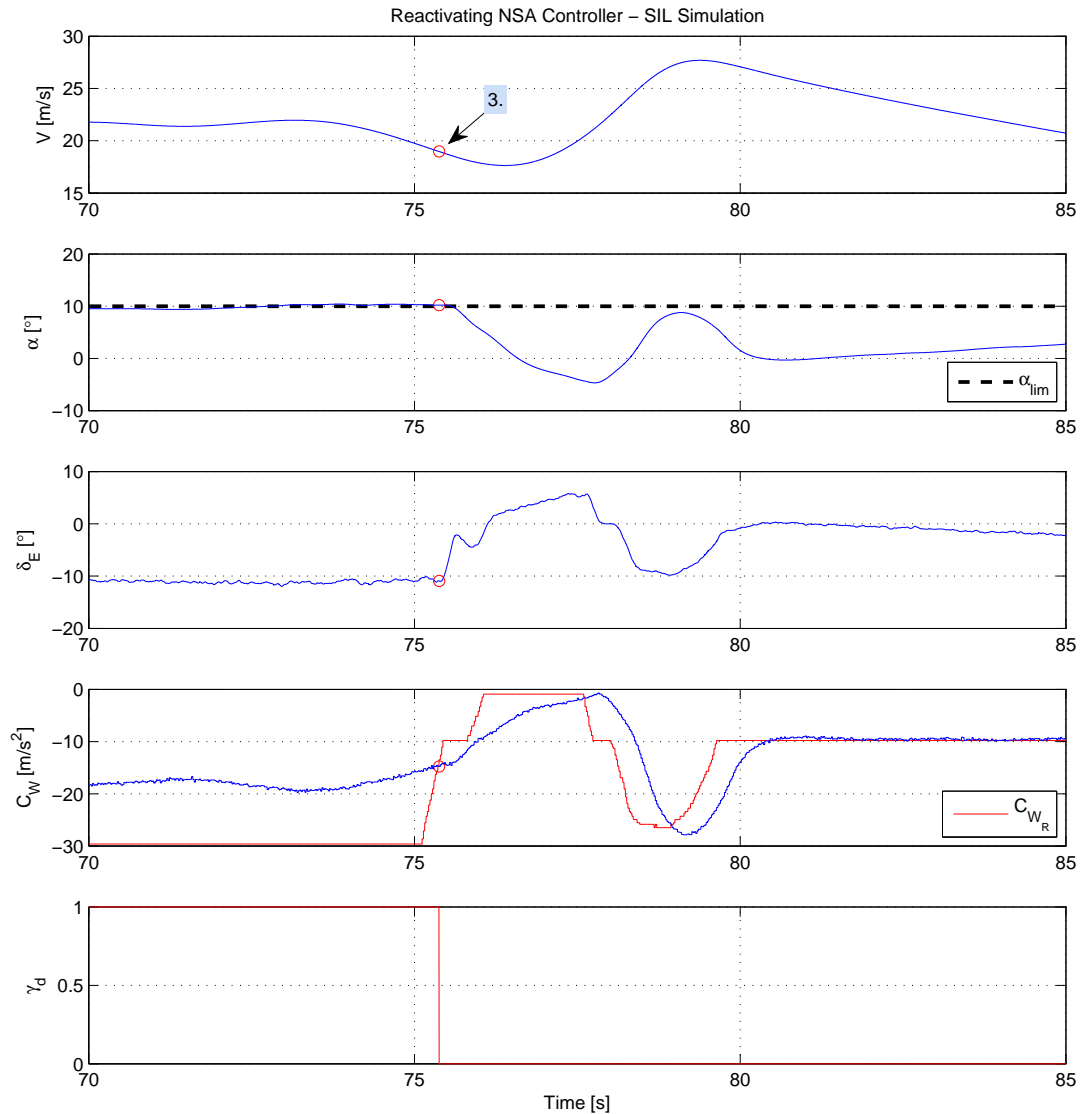


**Figure 7.6:** Nonlinear SIL simulation result for reconnecting the NSA controller

At marker 3 the stall prevention control system is deactivated and the NSA control system is reinitialised. The normal specific acceleration controller therefore resumes tracking the reference command without any undesired transients behavior during this transition from stall prevention control to normal unconstrained flight control.

Therefore, the stall prevention control system effectively constrains the angle of attack, thus preventing stall without severely limiting the flight control system. The control strategy exhibits the desired behaviour during on and off transitions and does not impose any additional constraints on the system.

The next section investigates the sensitivity of this stall prevention control system to model uncertainties.

## 7.3 Sensitivity Analysis

This section investigates the robustness of the stall prevention control strategy as a result of model uncertainties. It analyses the sensitivity of the stall prevention control system as well as the stall detection algorithm against parameter deviations. The method adopted for this investigation is a *worst-case performance* analysis that will determine the maximum and minimum worst-case response of the stall prevention control system for a certain level of parameter uncertainty.

### 7.3.1 Investigating Parameter Uncertainty

The parameters involved mainly consist of the aerodynamic stability and control derivatives, mass and inertia. However, only the parameters constrained to the longitudinal aircraft model will be considered. The mass can be accurately determined before flight and since the reduction in weight as a result of fuel consumption can be considered negligible, a high certainty rating is assigned to this parameter. The inertia ( $I_{yy}$  about the  $y_B$ -axis) is more difficult to determine and will therefore be assigned a lower certainty rating. However, the parameters that significantly influence the longitudinal model (concerning this analysis, more specifically the normal dynamics) are the aerodynamic derivatives.

A number of methods are used to evaluate the aerodynamic stability and control derivatives of an aircraft. These include analytical calculations from first principles, classical wind tunnel experimental measurements and flight test experimental measurements. The accuracy of the derivatives are subject to the quality of the source material and the method of evaluation, but ultimately the derivative values can at best be considered estimates regardless of the applied method. These methods are briefly described below.

**Analytical Calculations** This is the simplest and least accurate method for estimating the aerodynamic derivatives especially for the lateral-directional derivatives due to the difficulty in modelling the influence of the fuselage. However this method provides a good foundation for starting an analysis into the aerodynamic properties of the airframe by giving insight into the origins of the aerodynamic phenomena involved. The accuracy of these calculated derivative can be improved through the use of *semi-empirical* estimations by modifying the calculations with the addition of experimental aerodynamic reference data. Many software applications exist aimed at calculating

the stability and control derivatives. An example of such a program is AVL. For this research project, AVL was the main tool used to evaluate the stability and control derivatives of the aerial vehicle involved. The results are listed in Appendix B.

**Wind Tunnel Experiments** These tests involve subjecting a model of the airframe to a steady flow and analysing the force and moments at various static conditions of wind velocity, incidence angle and control surface deflection. Although uncertainty enters through the effects of scaling, measurements are made for actual aerodynamic flow conditions and in principle gives good estimates of the derivatives.

**Flight Test Experiments** Flight test measurement data of deliberate excitation of the aircraft's different modes of motion are used to indirectly estimate the aerodynamic derivatives. This is known as *parameter identification* which is entirely computational and based on the mathematical model of the aircraft. Since it is not always possible to perturb a single motion variable without affecting some of the other motions, inaccuracies arise due to the techniques and analysis algorithms applied. This analytical process makes full use of state space computational tools and applies them to the aircraft model in order to estimate the best state description that matches the input-output response of the aircraft.

### 7.3.2 Level of Uncertainty

The larger research project mentioned in Chapter 1, includes a system identification sub component which sole purpose is to estimate the aircraft stability and control derivatives online during flight. Supplying these estimated aerodynamic derivatives to the stall detection and prevention algorithms, could improve the accuracy of the state trajectory predictions depending on the accuracy of the sensors and their susceptibility to noise.

However, according to [7], the analytically calculated longitudinal derivatives are in general of higher fidelity compared to the lateral derivatives. Thus for this analysis, a conservative estimate of the level of uncertainty were chosen as a global factor for all the aerodynamic derivatives involved. The certainty rating were chosen as 80%, which means that any particular stability or control derivative is allowed to have a *worst-case deviation* of 20% in both a positive and negative direction.

The parameters involved in this sensitivity analysis with their respective certainty ratings are the following,

The next section conducts simulations on the stall detection algorithm and stall prevention controller based on these parameter certainty ratings.

| Stability Derivatives |                  | Control Derivatives |                  |
|-----------------------|------------------|---------------------|------------------|
| Derivative            | Certainty Rating | Derivative          | Certainty Rating |
| $C_{L\alpha}$         | 80%              | $C_{L\delta_E}$     | 80%              |
| $C_{LQ}$              | 80%              | $C_{m\delta_E}$     | 80%              |
| $C_{m\alpha}$         | 80%              |                     |                  |
| $C_{mQ}$              | 80%              |                     |                  |

**Table 7.2:** Certainty ratings for the estimated longitudinal stability and control derivatives

| Static Coefficients |                  | Additional Parameters |                  |
|---------------------|------------------|-----------------------|------------------|
| Coefficient         | Certainty Rating | Parameter             | Certainty Rating |
| $C_{L_0}$           | 80%              | $m$                   | 98%              |
| $C_{m_0}$           | 80%              | $I_{yy}$              | 85%              |

**Table 7.3:** Certainty ratings for the estimated longitudinal static coefficients as well as the mass and inertia

## 7.4 Worst-Case Performance Simulation

For this simulation, the parameter values listed in Appendix B are considered the nominal values (these include the derivative estimates calculated with AVL) and will be used to benchmark the algorithms and control strategies developed in this project. Therefore, for the ten variable parameters listed in Table 7.2 and Table 7.3, each allowed a minimum and maximum deviation value, the number of iterative simulations required to simulate all possible combinations are  $2^{10}$ .

### 7.4.1 Detection Algorithm

The first analysis involves the detection algorithm developed in Chapter 5. Consider the linear simulation results in Figure 7.7, when the elevator command is held constant at its minimum saturation angle, resulting in a pull-up manoeuvre forcing the angle of attack towards the stall angle.

The above results indicates that at the current measurement marker, the detection algorithm will trigger when the aircraft model is known perfectly. Applying a worst-case performance analysis at this particular measurement and comparing it to this nominal case, yields the results in Figure 7.8 for all possible combinations of the varied parameters.

Analysing the calculated trajectories against the nominal case, indicates a maximum worst-case deviation of 17% and a minimum worst-case deviation of 10% for the calculated peak angle of attack. In addition, both the maximum and minimum peak occurs at a later and earlier time instance respectively when compared to the nominal peak. This result conveys that parameter uncertainty will cause the detection algorithm to

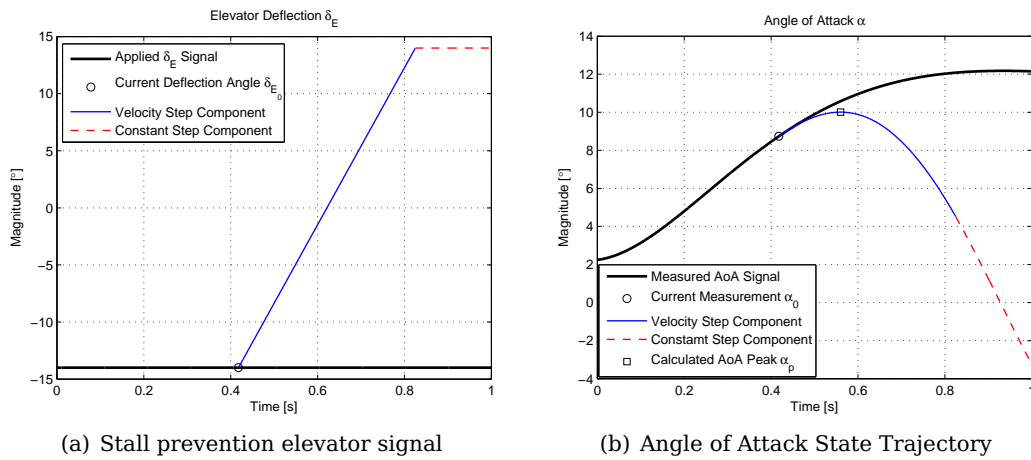


Figure 7.7: State trajectories calculated for stall prevention elevator input signal

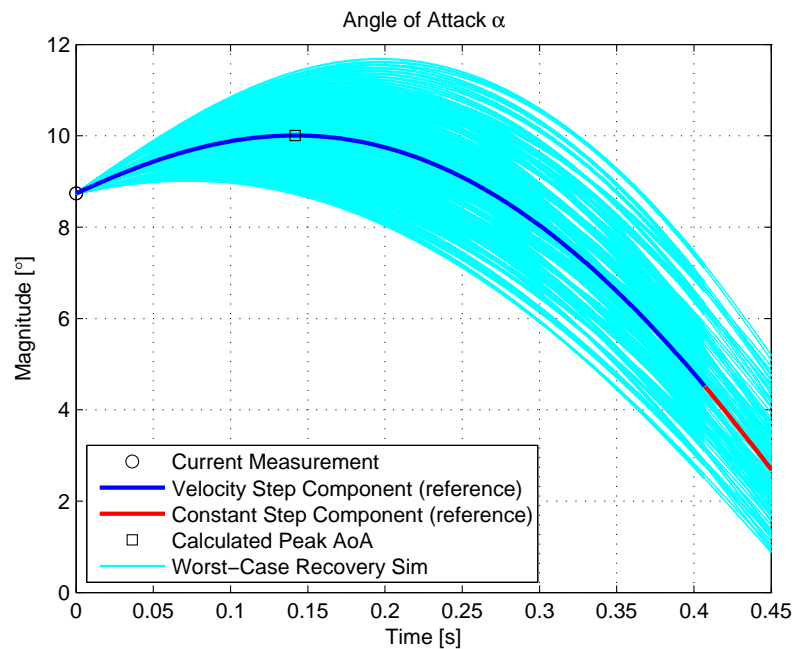
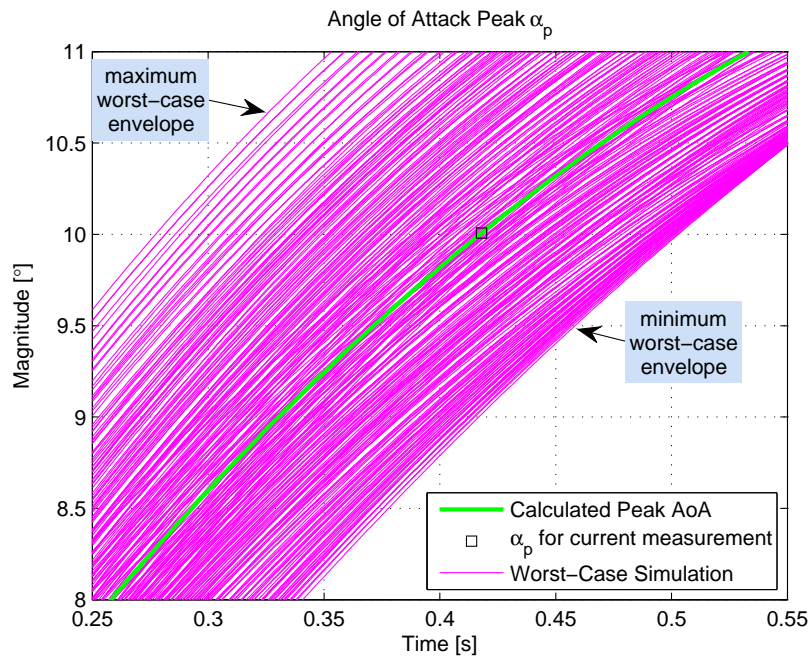


Figure 7.8: AoA stall prevention state trajectory with worst-case parameter variation

predict stall either too early or delayed. In order to better visualise this result, consider the following simulation which calculates the peak angle of attack for the stall prevention state trajectory of each parameter variation combination at each measurement of the measured angle of attack signal presented in Figure 7.7.

The result of this simulation is presented in Figure 7.9 and only display the calculated peak angles of attack in the region of interest about the current measurement marker. Notice that, for a combination of parameter variations causing the maximum worst-case envelope, the stall detection algorithm will trigger at an earlier time when compared to the nominal case. This results in premature detection, causing the stall prevention controller to override the NSA controller early, limiting the operating en-



**Figure 7.9:** AoA stall prevention state trajectory peak values with worst-case parameter variation

velope of the existing flight control system. In contrast, the combination of parameter variations causing the minimum worst-case envelope, will delay the detection causing it to trigger very close to the limit angle boundary.

Upon analysis, it was found that only a few parameters greatly influence the envelope of this worst-case simulation. These include the following aerodynamic derivatives,

- The static lift coefficient  $C_{L_0}$ , which characterises the lift produced by the camber of the wing's mean aerodynamic chord.
- The lift-curve-slope  $C_{L_\alpha}$ , which characterises the relationship between lift and angle of attack.
- The pitch stiffness  $C_{m_\alpha}$ , which characterises the pitching moment caused by a perturbation angle of attack.
- The elevator control power  $C_{m_{\delta_E}}$ , which characterises how effective the elevator is in creating a pitching moment.

Conducting the previous simulation whilst only varying the parameters listed above, yields the maximum and minimum worst-case envelope presented in Figure 7.10, with the maximum and minimum worst-case parameter variation combinations given by Table 7.4.

The detection time instances for both the maximum and minimum worst-case parameter variations are clearly indicated in Figure 7.10. The time instances of this pre-

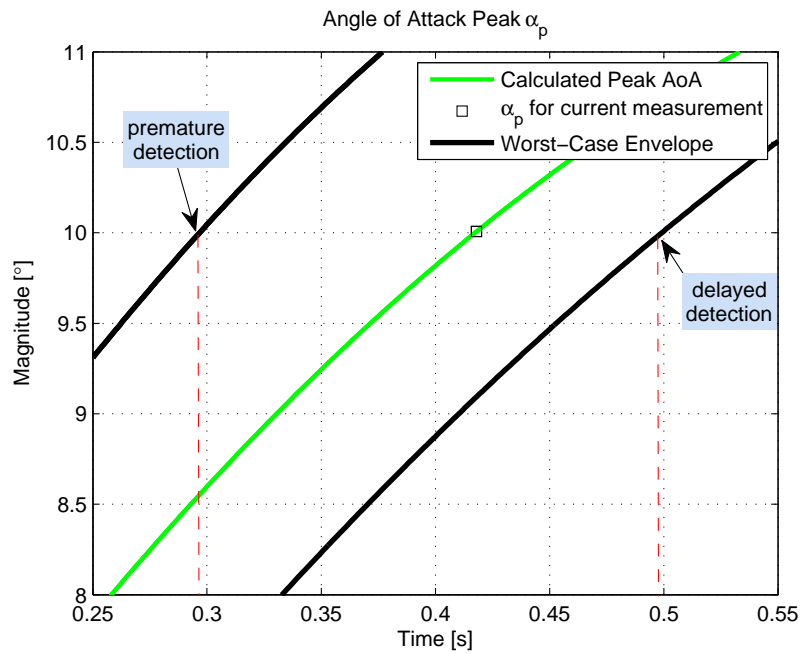


**Figure 7.10:** AoA stall prevention state trajectory peak values with  $C_{L_0}$ ,  $C_{L_\alpha}$ ,  $C_{m_\alpha}$  and  $C_{m_{\delta_E}}$  worst-case parameter variation

| Maximum Worst-Case |           | Minimum Worst-Case |           |
|--------------------|-----------|--------------------|-----------|
| Derivative         | Variation | Derivative         | Variation |
| $C_{L_\alpha}$     | -20%      | $C_{L_\alpha}$     | +20%      |
| $C_{L_Q}$          | -20%      | $C_{L_Q}$          | +20%      |
| $C_{m_\alpha}$     | -20%      | $C_{m_\alpha}$     | +20%      |
| $C_{m_Q}$          | +20%      | $C_{m_Q}$          | -20%      |

**Table 7.4:** Parameter variation combinations describing the maximum and minimum worst-case performance envelope

mature and delayed detection, directly relate to measured angle of attack values in Figure 7.7. Applying these two worst-case parameter variations to the respective angle of attack measurements on the measured signal in Figure 7.7, yields the results presented in Figure 7.11.

For this particular simulation, the worst-case premature detection will occur at  $6.6^\circ$  angle of attack and the worst-case delayed detection  $\alpha_p$  will occur at  $9.8^\circ$  angle of attack, causing the stall prevention controller to respond inefficiently. Notice the significant difference in the predicted state trajectories for the maximum and minimum worst-case parameter variations. The effect of this maximum and minimum worst-case parameter variation combination on the stall prevention control strategy will be investigated in the next section.



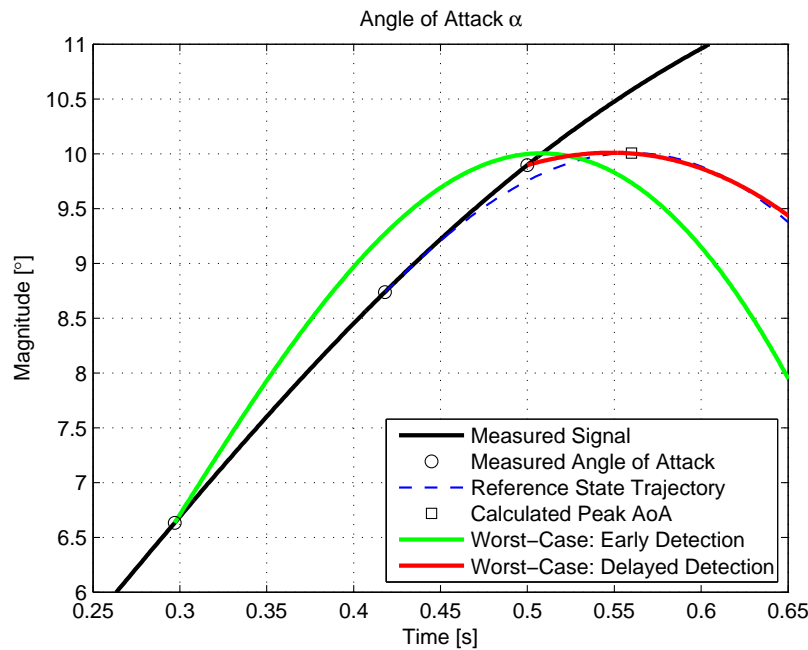


**Figure 7.11:** AoA stall prevention state trajectory for worst-case premature and delayed detection

#### 7.4.2 Stall Prevention Control System

The effect of this worst-case parameter variation on the stall prevention controller is more than just premature or delayed activation. The slew rate control algorithm is model predictive and thus dependant on the results provided by the forward predicted state trajectories. Since the control strategy consists of two stages, parameter variations in the initial slew rate control stage would affect the transient response of the AoA regulating control stage.

The feedback provided by the angle of attack sensor will desensitise the stall prevention control algorithm to parameter errors in the model. As a result, although stall is detected either premature or delayed, the algorithm will adapt the amount of preventative control it applies based on where the actual angle of attack transitioned to in state space. As a result, the undershoot or overshoot of the response is always less than the stall prediction error made at the inception of stall detection.

To demonstrate this, consider the linear simulation conducted in §7.1 to verify the control strategy operation and functionality. This simulation will now be extended to include the minimum and maximum worst-cases, as derived in this section. The results from the simulation of §7.1 will be included in this worst-case analysis to act as a benchmark for purpose of comparison.

The simulation results for the two respective worst-case parameter variations are presented in Figure 7.12. Note that the saturation constraint on the elevator has been removed from this analysis to give a clear view of the delayed stall prevention

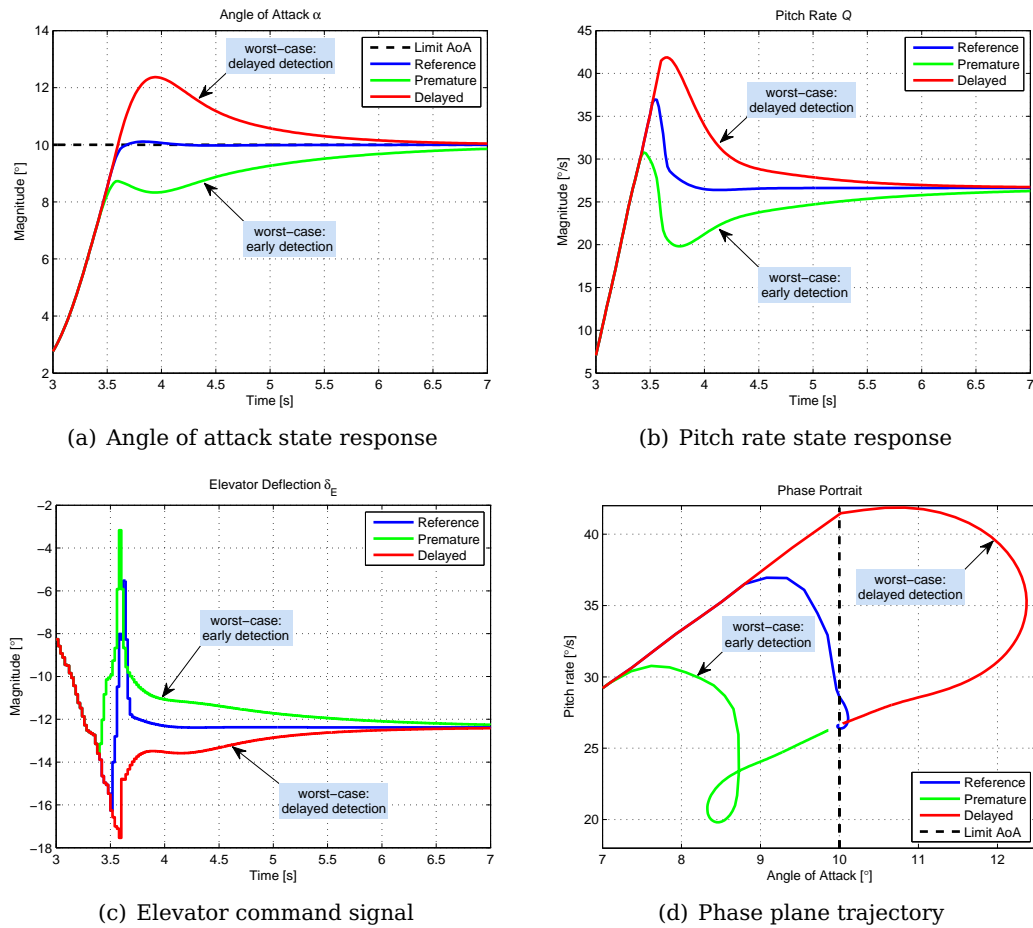


**Figure 7.12:** Linear worst-case performance simulation results

response. For all three response plots, the augmented integrator state removes any parameter uncertainty from the aircraft model in the steady state by enforcing zero steady state error during the AoA regulating control stage.

In the event of a worst-case premature stall detection, the slew rate control stage overestimates the angle of attack state response. This is caused by the slew rate control stage utilising the same forward prediction as calculated by the stall detection algorithm. Therefore it predicts a peak angle of attack that is greater than what is actually achievable by the aircraft, as presented in Figure 7.11. This results in the slew rate control stage applying too much control effort to the elevator, causing the actual angle of attack to peak below the predefined limit angle. When the AoA regulating control stage is triggered by this early peak, it initialises with unexpected state values, resulting in a significant transient. Fortunately, due to the augmented integrator state, all model uncertainty is removed in the steady state as the angle of attack is regulated towards the predefined limit angle.

In the event of a worst-case delayed stall detection, the slew rate control stage underestimates the angle of attack response. Therefore providing insufficient control

effort to the elevator during this stage of the prevention control strategy. However, due to this under estimation, the detection triggers close to the threshold value  $\alpha_h$ , thus providing little time for the slew rate control stage to react, as presented in Figure 7.11. The AoA regulating control stage activates almost immediately after the delayed detection, initialising with undesirable state values, causing a significant transient response with considerable overshoot. When the elevator saturation constraint is included in the simulation, the results are as follows,

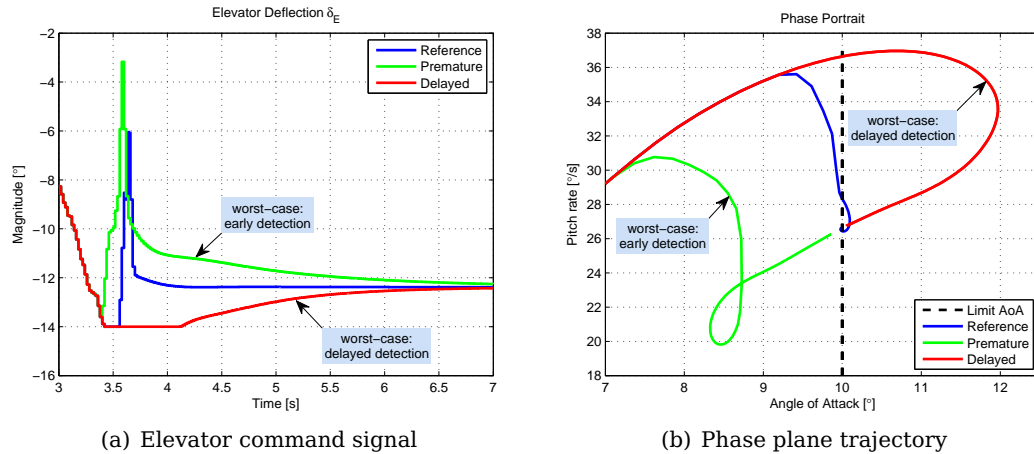


**Figure 7.13:** Linear worst-case performance simulation results

Notice how the elevator saturation limit actually assists in reducing the peak overshoot caused by the delayed detection. This analysis concludes the worst-case effects that model uncertainty has on the stall prevention control system developed in this project.

## 7.5 Summary

In this chapter the stall prevention control system was analysed during various simulations conducted on the linear and nonlinear aircraft models. The stall prevention control strategy proved effective in constraining the angle of attack without imposing undesired restrictions on the existing flight control system.

It was found that model uncertainty could cause either early or delayed detection. Since parameter uncertainty will cause this model prediction to over- or underestimate the state trajectory, the slew rate control stage will respond by applying too much or too little control effort respectively. Once the angle of attack signal peaks or reaches the threshold angle, the AoA regulating control stage will be activated. If this control stage initialises with unexpected state values, a significant transient could be expected in the response. However, due to the added integrator state, the controller will ensure zero error in the steady state.

A large uncertainty in the aerodynamic derivatives  $C_{L_0}$ ,  $C_{L_\alpha}$ ,  $C_{m_\alpha}$  and  $C_{m_{\delta_E}}$  could lead to undesirable performance in the transient of the stall preventative response. It is therefore of paramount importance to accurately determine these parameters through either semi-empirical methods or wind tunnel experiments.

## Chapter 8

# Conclusions and Recommendations

This chapter concludes this thesis with a summary of the work presented and highlights the contributions made to this field of research at the electronic systems laboratory. Recommendations for further research on this topic are made and possible future improvements are proposed.

### 8.1 Summary

This thesis reported on the research conducted to investigate, design and develop a flight control subsystem capable of preventing a fixed-wing aircraft from entering aerodynamic stall.

The main purpose of the stall prevention control system was to constrain the angle of attack of the aircraft, by augmenting the existing flight control system without imposing any severe restriction on the normal flight envelope. Appropriate stall prevention procedures were investigated in a literature study and the longitudinal motion of the aircraft was identified as the main focus of this control problem. Limiting the angle of attack to the linear aerodynamic region, will prevent stall and allow model simplification and assumptions to be made.

The stall prevention control system designed in this project was based on the aircraft model and acceleration based flight control strategy developed by [1]. This allows the stall prevention control system to be applied at any gross attitude, thus making it particularly useful for highly manoeuvrable UAV's.

For this first iteration of the stall prevention control problem, only the elevator control surface was incorporated to prevent stall. Therefore the stall prevention control system was required to augment only the aircraft's normal dynamics. A switching

strategy was developed to constrain the angle of attack by switching between two separate control systems, where the primary controller was the existing normal specific acceleration (NSA) control system and the secondary controller the angle of attack regulating control system.

The detection algorithm behind the switching strategy was developed and included a model predictive element to foresee an approaching stall before it occurs. This was accomplished through analytic forward propagation of the angle of attack state to predict when the state trajectory will result in stall. This enables the stall prevention control system to only constrain the angle of attack at the last possible moment, thus ensuring that the stall prevention control system will only intervene when necessary. This led to the development of the concept of a pre-stall region bounded by a detection envelop in the phase plane.

The stall prevention control system was implemented as a finite state machine and consisted of two control stages. The first stage was responsible for dynamically limiting the elevator control command to optimally guide the angle of attack towards the limit angle. To accomplish this a recursive model predictive slew rate control algorithm was developed with feedback from an angle of attack measurement, which takes the slew rate and saturation limits of the aircraft's servos into account. The second control stage was responsible for regulating the angle of attack at this limit angle, once the first stage prevented the angle of attack from exceeding this predefined limit. This control strategy avoided the design of a complex full model predictive control system and was sufficient for constraining and regulating the angle of attack.

In addition, this switching strategy allowed the NSA control system to regain control of the elevator control surface once the exiting flight control system returned to a operating condition within the pre-stall bounded region in the phase plane. This reactivation of the NSA controller was designed to allow for a smooth transition from stall prevention to normal unconstrained flight control, without exhibiting any switching transients.

The complete stall prevention control strategy was tested and analysed through simulation on the linear and nonlinear aircraft models. Software in the loop simulations (SIL) verified the different aspects and performance of the stall prevention control system. Furthermore, a sensitivity analysis was conducted on this stall prevention control strategy to determine its robustness and susceptibility to model uncertainty. During this analysis four aerodynamic derivatives were identified to have the largest effect of the robustness of this stall prevention control system.

### 8.1.1 Computational Efficiency

Computational efficiency plays a key role since it determines the ability of this control strategy to be implemented on various hardware platforms. To ensure that this stall prevention control augmentation strategy can be implemented on the existing low cost avionics package housing the existing flight control system, care was taken during the development of the various detection and prevention control algorithms.

Closed form solutions were pursued and derived as far as possible. When no closed form solution was available, for example in the detection algorithm, a numerical method was developed to enforce rapid convergence. This method also included the ability to detect divergence to prevent unnecessary computations. The recursive model predictive slew rate control algorithm incorporates this peak predicting algorithm into a modified false position method to control the slew rate of the elevator command during the initial stage of the stall prevention control strategy.

The computational efficiency of this stall prevention control strategy will need to be verified during hardware in the loop (HIL) simulations to determine if it is feasible to implement this control strategy on the existing low cost avionics package.

### 8.1.2 Contributions

During the course of this research project, the following contributions were made towards the development of future projects on UAV's within the ESL autonomous flight research group:

- An extensive literature study was conducted, consulting with various literature sources to form a chapter dedicated to the phenomena of aerodynamic stall. This will prove valuable for future research and will provide a convenient starting point.
- A switching control strategy was developed to augment the existing flight control system. This will allow for effortless integration into the existing flight control architecture. The modular nature of this control strategy allows for expansion or improvement of individual control components.
- A phase plane approach was adopted to analyse the normal dynamics of the aircraft. This led to the design of a predictive algorithm to foresee an approaching stall based on the model dynamics. This analysis tool is not limited to the linear domain and could be extended to include nonlinear dynamics, most notably those governing post-stall, where similar techniques could be used to return the aircraft safely to pre-stall flight.

- A model predictive slew rate control algorithm was developed, which incorporates feedback from an angle of attack measurement, to prevent the angle of attack from exceeding a predefined limit angle.
- A control system was designed to regulate the angle of attack once it reaches the predefined limit angle.

Since the current UAV does not have any form of angle of attack measuring device fitted to it, Appendix B investigates and proposes typical sensors which will allow the angle of attack to be measured during flight.

## 8.2 Recommendations

The following recommendations arise directly from the analysis results presented in Chapter 7 and will be discussed briefly in the following itemised form.

- The model based nature of the detection algorithm and slew rate control algorithm requires accurate estimates of the aerodynamic derivatives  $C_{L_0}$ ,  $C_{L_\alpha}$ ,  $C_{m_\alpha}$  and  $C_{m_{\delta_E}}$ . Therefore, instead of relying on empirically calculated aerodynamics derivative data, actual wind-tunnel test data will need to be considered to ensure the best possible performance for this stall prevention control strategy.
- An angle of attack sensor will also need to be developed and calibrated through wind-tunnel testing. The AoA sensor will be required to provide feedback to the stall prevention control system. Consult Appendix B and the references therein to obtain the necessary information on AoA sensors and how to calibrate them.
- Before this stall prevention control system is integrated into the fault-tolerant flight control system, every individual aspect of the control strategy will need to be verified through practical flight tests. As an example, select a predefined angle of attack limit well inside the linear aerodynamic region. This is to test the control algorithms developed in this project without allowing the velocity to decrease towards the stall speed.

### 8.2.1 Further Research

A possible improvement to this stall prevention control system is to design a controller to replace the second stage of the control strategy, which will regulate the angle of attack and will be less susceptible to sensor noise.

A definite extension to this current stall prevention control strategy, is to incorporate the axial dynamics through the design of some form of thrust recovery control system.



This will account for the loss of velocity and will command the aircraft to increase thrust during stall prevention, thus ensuring that the velocity never decreases below the stall speed. This will account for all the longitudinal dynamics of the aircraft. The stall prevention control algorithms could also be extended to recover from stall using all the nonlinear aircraft dynamics.

In addition, the stall prevention control strategy could be further extended to account for the lateral dynamics, by designing a spin prevention control system. This control system will prevent the aircraft from entering autorotation during stall prevention control and will be particularly useful during fast highly banked turns. This would yield a control system which could augment the existing flight control architecture and constrain an aircraft to a safe flight envelope.

# List of References

- [1] Peddle, I.: *Acceleration Based Maneuver Flight Control System for Unmanned Aerial Vehicles*. Ph.D. thesis, University of Stellenbosch, 2008.
- [2] John D. Anderson, J.: *Fundamentals of Aerodynamics*. McGraw-Hill, 1984.
- [3] Shevell, R.S.: *Fundamentals of Flight*. 2nd edn. Prentice-Hall, Inc, 1989.
- [4] FAA-H-8083-3A: *Airplane Flying Handbook*. Federal Aviation Administration Publications, 2004.
- [5] Roskam, J.: *Airplane Flight Dynamics and Automatic Flight Controls*, vol. Part I. 3rd edn. DARcorporation, 2001.
- [6] Talay, T.A.: *Introduction to the Aerodynamics of Flight*. NASA Scientific and Technical Information Office, 1975. Prepared at Langley Research Centre.
- [7] Cook, M.V.: *Flight Dynamics Principles*. 2nd edn. Butterworth-Heinemann, 2007.
- [8] Perkins, C.D. and Hage, R.E.: *Airplane Performance Stability and Control*. John Wiley & Sons, 1949.
- [9] Simons, M.: *Model Aircraft Aerodynamics*. Forth edn. Argus Books, 1994.
- [10] Kermode, A.: *Mechanics of Flight*. Metric edition edn. Pitman Publishing Limited, 1979.
- [11] McCormick, B.: *Aerodynamics, Aeronautics and Flight Mechanics*. Forth edn. Argus Books, 1994.
- [12] Shyy, W., Lian, Y., Tang, J., Viieru, D. and Liu, H.: *Aerodynamics of Low Reynolds Number Flyers*. Cambridge Aerospace Series. Cambridge University Press, 2008.
- [13] Kutz, M.: *Eshbach's Handbook of Engineering Fundamentals*. 5th edn. John Wiley & Sons, Inc, 2009.
- [14] Kimberlin, R.D.: *Flight Testing of Fixed-Wing Aircraft*. AIAA Education Series. American Institute of Aeronautics and Astronautics, Inc, 1940.

- [15] FAA-H-8083-25A: *Pilot's Handbook of Aeronautical Knowledge*. United States Department of Transportation, Federal Aviation Administration, 2008.
- [16] Peddle, I. and Jones, T.: Acceleration Based 3D Manoeuvre Flight Control System for UAV's: Strategy and Longitudinal Design. *Automatica*, 2008.
- [17] Etkin, B.: *Dynamics of Flight Stability and Control*. 3rd edn. John Wiley and Sons, NJ, 1996.
- [18] Goodwin, G.C., Graebe, S.F. and Salgado, M.E.: *Control System Design*. Prentice-Hall, 2001.
- [19] Gopal, M.: *Control Systems: Principles and Design*. 2nd edn. McGraw-Hill, 2003.
- [20] Blaauw, D.: *Flight Control System for a Variable Stability Blended-Wing-Body Unmanned Aerial Vehicle*. Master's thesis, University of Stellenbosch, 2009.
- [21] Abramowitz, M. and Stegun, I.A.: *Handbook of Mathematical Functions*. Ninth edn. Dover Publications, 1970.
- [22] Hamming, R.: *Numerical Methods for Scientists and Engineers*. 2nd edn. Dover Publications, 1986.
- [23] Gopal, M.: *Digital Control and State Variable Methods*. 2nd edn. McGraw-Hill, 2004.
- [24] Edwards A. Hearing, J.: Heated angle of attack vane. Data sheet, SpaceAge Control, Inc., 1997.
- [25] Silberbauer, M.: Simulation visualization system. Undergraduate Final Year Project, 2005.
- [26] Gaum, R.: *Aggressive Flight Control Techniques for a Fixed-wing Unmanned Aerial Vehicle*. Master's thesis, University of Stellenbosch, 2009.
- [27] Nelson, D.R.C.: *Flight Stability and Automatic Control*. McGraw-Hill, 1989.
- [28] Blakelock, J.H.: *Automatic Control of Aircraft and Missiles*. 2nd edn. John Wiley & Sons, Inc., 1991.
- [29] Etkin, B.: *Dynamics of Atmospheric Flight*. John Wiley & Sons, Inc., 1972.
- [30] Edwards A. Hearing, J.: Airdata calibration of high-performance aircraft for measuring atmospheric wind profiles. Technical memorandum 101714, NASA, 1989.
- [31] Edwards A. Hearing, J.: Airdata measurement and calibration. Technical memorandum 104316, NASA, 1995.

# **Appendices**

# Appendix A

## Mathematical Derivations

### A.1 Aircraft Trim Condition

Trimmed flight occurs only when all the forces and moments acting about the aircraft's  $CG$  are in equilibrium. For a given  $CG$  position, altitude and airspeed, the trim condition is defined by the angle of attack, elevator angle, thrust, pitch attitude and flight path angle. During symmetric level flight the flight path angle  $\theta_W$  is zero with the pitch attitude exactly equal to the angle of attack. The pitching moment about the  $CG$  ( $M$ ) as well as the pitch rate ( $Q$ ) are zero.

A simplified representation of the forces and moments acting on an aircraft during symmetric level flight is shown in Figure A.1, with the lateral forces and moments assumed to remain in equilibrium throughout.

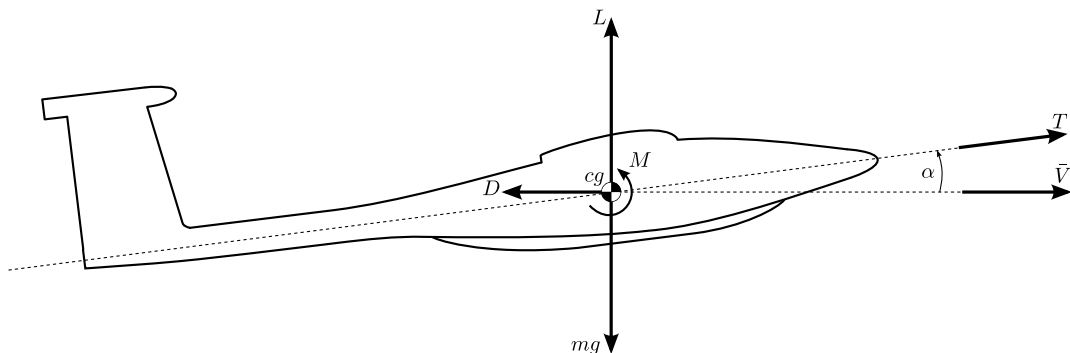


**Figure A.1:** Forces and moments acting on an aircraft during symmetric level flight

Assuming a commonly used force and moment model for longitudinal flight, where the thrust vector is assumed to act through the aircraft's  $CG$  along the axial body axis and that the total drag moment is assumed insignificant due to the small vertical displacement between the  $AC$  and the  $CG$  on most aircraft configurations [7]. From

Equation (3.9) and (3.10) it can be shown that during trimmed flight, when the angle of attack is usually small and  $C_W = -g$ ,

$$D \approx T \quad (\text{A.1})$$

$$L \approx mg \quad (\text{A.2})$$

Applying these relationships to the lift and pitching moment coefficients expressed in Equations (3.14) and (3.15) yields the following,

$$C_{m_0} + C_{m_\alpha} \alpha + C_{m_{\delta_E}} \delta_E = 0 \quad (\text{A.3})$$

$$C_{L_0} + C_{L_\alpha} \alpha + C_{L_{\delta_E}} \delta_E = \frac{mg}{qS} \quad (\text{A.4})$$

The above result can be solved simultaneously for the trim angle of attack and trim elevator deflection angle as follows,

$$\begin{aligned} \begin{bmatrix} C_{m_\alpha} & C_{m_{\delta_E}} \\ C_{L_\alpha} & C_{L_{\delta_E}} \end{bmatrix} \begin{bmatrix} \alpha \\ \delta_E \end{bmatrix} &= \begin{bmatrix} -C_{m_0} \\ \frac{mg}{qS} - C_{L_0} \end{bmatrix} \\ \therefore \begin{bmatrix} \alpha_{trim} \\ \delta_{E_{trim}} \end{bmatrix} &= \begin{bmatrix} C_{m_\alpha} & C_{m_{\delta_E}} \\ C_{L_\alpha} & C_{L_{\delta_E}} \end{bmatrix}^{-1} \begin{bmatrix} -C_{m_0} \\ \frac{mg}{qS} - C_{L_0} \end{bmatrix} \end{aligned} \quad (\text{A.5})$$

Since the stability and control derivatives are constant for the linear model<sup>1</sup>, it is clear from the above equation that the trim values are dependant on the dynamic pressure and therefore quadratically proportional to the air velocity (see Appendix A.4).

## A.2 Longitudinal Stability Characteristics

### A.2.1 Vertical speed stability

According to [5], for static stability against vertical velocity perturbations during steady state flight, the lift-curve-slope  $C_{L_\alpha}$  of an airframe must be positive, therefore,

$$C_{L_\alpha} > 0 \quad (\text{A.6})$$

This condition will be satisfied as long as the angle of attack remains lower than the critical angle. The derivative  $C_{L_\alpha}$  therefore plays an important roll in defining the flying quality when the airframe is subjected to turbulence. The aircraft will experience continuous changes in angle of attack induced by the turbulent air. This

<sup>1</sup>With this assumption, the compressibility, aeroelastic and propulsive system effects are ignored.

in turn relates to the load factor ( $n$ ) of the aircraft which can be expressed as,

$$n = \frac{L}{W} = \frac{C_L \mathbf{q} S}{W} \quad (\text{A.7})$$

differentiating this expression with respect to the angle of attack yields,

$$\frac{\partial n}{\partial \alpha} = n_\alpha = \frac{\mathbf{q} C_{L_\alpha}}{(W/S)} \quad (\text{A.8})$$

where the derivative  $n_\alpha$  is referred to as *the load factor due to gust induced angle of attack* and defines the aircraft's gust responsiveness. If its numeric value is large, the airframe will be very sensitive to turbulence and exhibit poor flying quality. Consequently, if its numeric value is small, the airframe would glide smoothly through turbulence.

The wing design of the UAV used during this research project, has a relatively high aspect ratio with no sweep angle, therefore it will yield a large value for  $C_{L_\alpha}$ . By combining this with a large value of *wing loading* ( $W/S$ ), the airframe would exhibit adequate stability against turbulence.

The derivative  $C_{L_\alpha}$ , together with  $C_{m_\alpha}$  and  $C_{m_Q}$ , also plays an important roll in determining the damping ratio of the short period mode oscillation of the airframe. A relatively large damping ratio is desirable and also contribute to the overall flying quality if the airframe. However, excessive damping will inhibit the airframe's manoeuvrability. This will be shown in the following chapter.

### A.2.2 Angle of attack stability

During steady state flight, the pitching moment about the aircraft's centre of gravity ( $M$ ) is zero and the aircraft is referred to as being in *equilibrium*. At this trim condition, the aircraft is travelling at a constant speed and altitude with the elevator and angle of attack fixed at a certain angle.

When the vehicle experiences a disturbance in angle of attack  $\Delta\alpha$ , while keeping the elevator angle fixed, the aircraft will be perturbed from its equilibrium condition. A natural statically stable airframe would tend to oppose the disturbance by reacting with a negative pitching moment  $\Delta C_m$ , thus restoring the angle of attack to its equilibrium value [27]. This will only happen when,

$$C_{m_\alpha} < 0 \quad (\text{A.9})$$

referred to as the condition for *longitudinal static stability*. This forms an important criteria for an aircraft to be able to safely recover from stall or to ensure adequate

stall prevention capability. If  $C_{m_\alpha}$  were to be positive at the onset of stall, then the aircraft would be pushed deeper into stall and it would be unlikely to recover.

Consider the simplified longitudinal aircraft model in Figure A.2, displaying only the normal forces and pitching moments acting at the aircraft's reference centres. It has been assumed that during steady level flight, the thrust and drag forces are in equilibrium and that small disturbances in incidence cause negligible change in this condition, thus only affecting the lift forces and pitching moments.

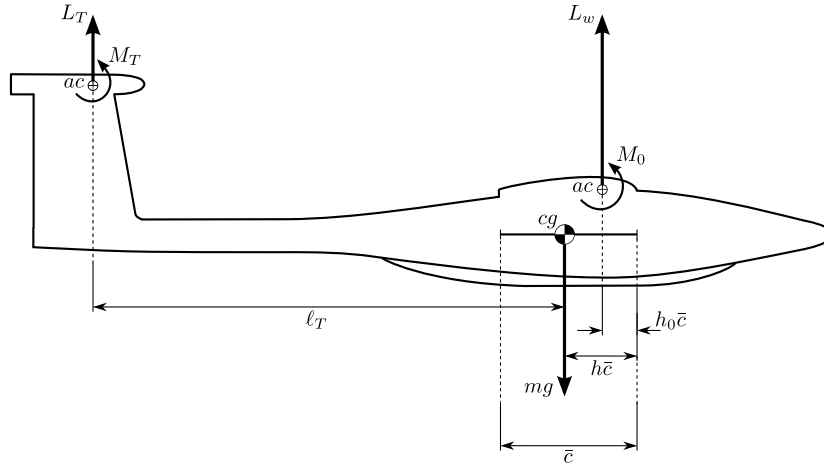


**Figure A.2:** Simple pitching moment model for a statically stable airframe configuration

For the purpose of this stability investigation this is a viable assumption which greatly simplifies the pitching moment equation about the aircraft's *CG*, which is expressed as follows,

$$M = M_0 + L_w (h - h_0) \bar{c} - L_T \ell_T + M_T \quad (\text{A.10})$$

where the wing and fuselage are assumed to behave as a wing alone. This is a satisfactory assumption for subsonic aircraft with relatively high aspect ratio wing's, such as the airframe used for this research project. The aerofoil of the horizontal stabiliser usually has zero camber, thus  $M_T$  becomes zero.

Expressing the moment equation in its coefficient form yields,

$$C_m = C_{m_0} + C_{L_w} (h - h_0) - V_H C_{L_T} \quad (\text{A.11})$$

where  $V_H$  denotes the horizontal tail volume ratio.

Since  $C_{L_T}$  is the lift coefficient based on the surface area of the horizontal stabiliser  $S_T$ , the tail contribution to the total lift coefficient  $C_L$  is then  $C_{L_T} \frac{S_T}{S}$ . Therefore, the lift coefficient of the wing  $C_{L_w}$  can be approximated as  $C_L$  since the tail contribution



is small compared to the wing which yields [5],

$$C_m = C_{m_0} + C_L(h - h_0) - V_H C_{L_T} \quad (\text{A.12})$$

Taking the first derivative of Equation (A.12) with respect to  $\alpha$  yields the expression for the *pitch stiffness*,

$$C_{m_\alpha} = C_{L_\alpha}(h - h_0) - V_H C_{L_{T_\alpha}} \quad (\text{A.13})$$

Notice that  $C_{m_\alpha}$  depends linearly on the position of the CG and since  $C_{L_\alpha}$  is usually large and positive, the magnitude and sign of  $C_{m_\alpha}$  is strongly affected by  $h$ . The CG position for which  $C_{m_\alpha}$  is zero, defines the aft limit for the CG location and marks the transition point between static stability and instability in pitch. This position is referred to as the *controls fixed neutral point* (NP) and is denoted  $h_n$ , which can be readily calculated from Equation (A.12).

The difference between the CG and the NP is referred to as the *static margin*  $K_n$ , which gives a numerical indication of the level of stability in pitch for a particular airframe and is expressed as,

$$K_n = -\frac{C_{m_\alpha}}{C_{L_\alpha}} = h_n - h \quad (\text{A.14})$$

Since  $C_{m_\alpha}$  is required to be negative according to the stability condition,  $h < h_n$  or  $K_n > 0$ , in other words the CG has to be located forward of the NP. The forward limit of the CG position is determined by control considerations, since too much stability requires a large amount of control effort to manoeuvre the aircraft [20].

Therefore, the position of the CG plays an important roll in determining the ability of the aircraft to be controlled during a recovery procedure as well as the stability of the aircraft to return to its trim condition.

### A.3 Static Contribution

Gravity couples into the short period mode motion (normal dynamics) through the flight path angle  $\theta_W$ . Upon analysis of the longitudinal transfer functions for elevator displacement in the frequency domain [28], it is evident that a considerable variation in  $\theta$  occurs at the undamped natural frequency of the short period mode and that the forward velocity remains relatively constant during this mode of motion<sup>2</sup>. However, this does not invalidate the approximation made by assuming constant  $\theta_W$  during forward propagation of the recovery response, since the angle of attack peak as a result of this recovery response is the primary interest of this algorithm. This peak

<sup>2</sup>Where the relationship between the pitch attitude  $\theta$  and the flight path angle  $\theta_W$  is the angle of attack:  $\theta = \alpha + \theta_W$

generally occurs within 0.5s and the variation in  $\theta_W$  induced by the recovery excitation signal only affects the steady state of the recovery response. Therefore the initial transient of the recovery response trajectory remains unaffected by the variation of  $\theta_W$  through the gravity term.

Consider the following simulation conducted on the stall detection algorithm to verify this approximation and to substantiate the above statements.

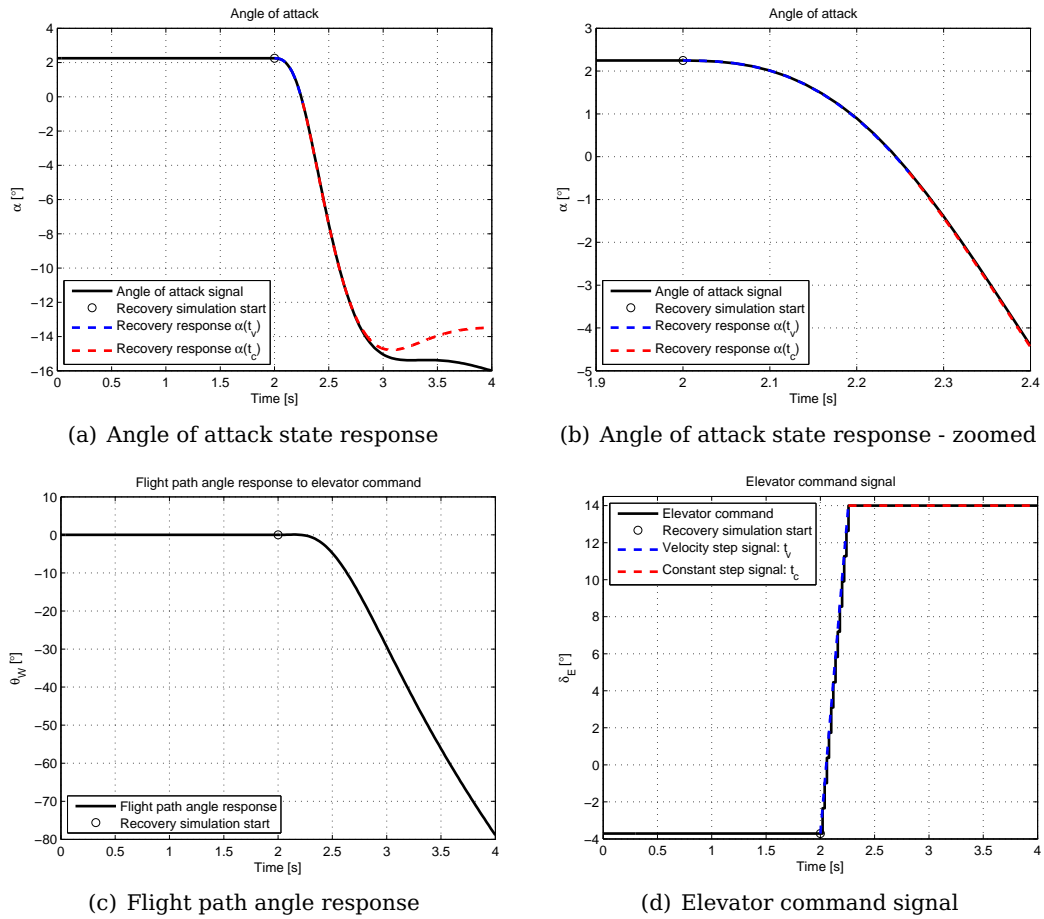


**Figure A.3:** Effect of flight path angle on angle of attack recovery transient trajectory

For this simulation the aerial vehicle is flying straight and level. At the time instance of 2.0 s, the elevator command signal is given a velocity step and is then held constant at its maximum limit. This resembles the excitation signal used for the recovery response trajectory forward propagation. The figures present the actual response from the linear model to this elevator signal as well as the predicted trajectory, calculated with Equation (5.13), at the onset of this elevator command at 2.0 s.

Notice that the flight path angle  $\theta_W$  remains zero during trimmed flight and that it only starts to have a significant effect after that elevator has already reached its saturation limit. Also notice the slight undershoot caused in  $\theta_W$  by the elevator signal

change. This is due to the fact that the rate of change of flight path angle is coupled to the normal specific acceleration [16], which from the point mass kinematics can be expressed as,

$$\dot{\theta}_W = \frac{-(C_W + g \cos \theta_W)}{\bar{V}} \quad (\text{A.15})$$

Within 0.5 s of the elevator signal change, the flight path angle remains relatively small and has negligible effect on the angle of attack response. Since by this time the calculated response due to the velocity step has already completed, with the angle of attack peak usually coinciding with the part of the recovery response, the change in the gravity term can be considered negligible.

The effect of this approximation only becomes apparent once  $\theta_W$  has become sufficiently large with respect to its initial value at 2.0 s. Therefore, by assuming the flight path angle  $\theta_W$  remains constant during the forward state prediction, the actual linear behaviour during the time of interest will be approximated accurately.

To derive the expressions for the static contribution, consider the following expansion of the static term in (4.3),

$$\Phi(s) \mathbf{b} s^{-1} = \frac{1}{\lambda(s)} \begin{bmatrix} s - a_{22} & a_{12} \\ a_{21} & s - a_{11} \end{bmatrix} \begin{bmatrix} b_1 \\ b_2 \end{bmatrix} \begin{pmatrix} 1 \\ s \end{pmatrix} = \begin{bmatrix} \mathcal{F}_\alpha(s) \\ \mathcal{F}_Q(s) \end{bmatrix} \quad (\text{A.16})$$

with  $\mathcal{F}_\alpha(s)$  and  $\mathcal{F}_Q(s)$  both having the symbolic form expressed in Equation (A.17).

$$\mathcal{F}(s) = \frac{a_2 s^2 + a_1 s + a_0}{s^2 \left( (s + \sigma)^2 + \omega_d^2 \right)} \quad (\text{A.17})$$

The coefficients  $a_2$ ,  $a_1$  and  $a_0$  in Equation (A.17) are defined as follows for the angle of attack and pitch rate static contribution as follows,

$$\mathcal{F}_\alpha(s) \begin{cases} a_2 = b_1 \\ a_1 = b_2 a_{12} - b_1 a_{22} \\ a_0 = 0 \end{cases} ; \quad \mathcal{F}_Q(s) \begin{cases} a_2 = b_2 \\ a_1 = b_1 a_{21} - b_2 a_{11} \\ a_0 = 0 \end{cases}$$

Conducting a partial fraction expansion on the expression in Equation (A.17), yields the following equation,

$$\frac{a_2 s + a_1}{s \left( (s + \sigma)^2 + \omega_d^2 \right)} = \frac{A_1}{s} + \frac{A_3 \omega_d + A_4 (s + \sigma)}{(s + \sigma)^2 + \omega_d^2} \quad (\text{A.18})$$

which can easily be inverse Laplace transformed to give the time expressions of the static contribution. The resulting time functions are derived to have the following

form for both the angle of attack and pitch rate states.

$$\mathcal{L}^{-1}[\mathcal{F}(s)] = f(t) = A_1 + A_3 e^{-\sigma t} \sin(\omega_d t) + A_4 e^{-\sigma t} \cos(\omega_d t) \quad (\text{A.19})$$

The coefficients  $A_1$ ,  $A_3$  and  $A_4$  in Equation (A.19) are defined for both the angle of attack and pitch rate static contribution equations as follows,

$$\alpha_{SC}(t); Q_{SC}(t) \begin{cases} A_1 = a_1 \kappa^{-1} \\ A_3 = (a_2 \sigma - a_1 + \omega_d^2 A_1) (\omega_d \sigma)^{-1} \\ A_4 = -A_1 \end{cases}$$

with  $\kappa = \sigma^2 + \omega_d^2$ .

#### A.4 Variation of Elevator Trim Angle with Velocity

The term on the right-hand-side of Equation (A.4) can be considered as the lift coefficient at the trim velocity,

$$C_{L_{trim}} = \frac{mg}{\frac{1}{2} \rho V_a^2 S} \quad (\text{A.20})$$

According to [29], the variation of  $\delta_{E_{trim}}$  with velocity is a unique function of  $C_{L_{trim}}$  for each specific  $cg$  position. Since  $C_{L_{trim}}$  is in turn fixed by the air velocity for horizontal flight, then  $\delta_{E_{trim}}$  becomes a unique function of  $V_a$ . Examples of typical desirable curve forms, for the elevator trim angle with variation in air speed for different  $cg$  positions are presented in Figure A.4.

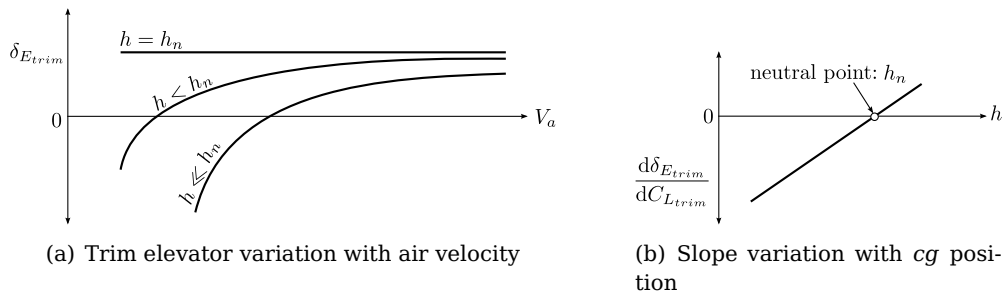


**Figure A.4:** Example of variation of elevator angle to trim with speed and  $cg$

For any  $CG$  position, an increase in the trim air velocity from any initial value, requires a downward deflection of the elevator and as a result a decrease in angle of attack. The rate of the movement  $\frac{d\delta_{E_{trim}}}{dV_a}$ , referred to as *the elevator position stability*, decreases with the aft movement of the  $CG$ . When the  $CG$  coincides with the  $NP$ , the

pilot (or flight control system) will have no control over trim speed, thus the vehicle becomes difficult to control. When the *CG* is located aft the *NP*, the elevator position stability will reverse, causing the controllability of the vehicle to deteriorate rapidly [27].

With the state trim values defined, the focus now lies with solving the state transition matrix. This will be presented in the following section.

## A.5 Elevator Effectiveness

As discussed in Chapter 2, the elevator control surface is used to reduce the pitch attitude (and thus the angle of attack) of the aircraft during stall prevention and recovery procedures. The control effectiveness of the elevator is a measure of how effective elevator is in producing the desired control moment, in this case pitching moment. It is a function of the size of the control surface and the *tail volume ratio*. Although the pitch attitude can be controlled by either an aft (conventional) or forward (canard) horizontal stabiliser, the following investigation is restricted to an conventional tail configuration. The effectiveness of the elevator to control the behaviour of the aircraft's angle of attack will now be investigated.

When the elevator is deflected, it changes the lift and pitching moment of the aircraft [27]. This can be expressed for the lift and pitching moments coefficients as follows,

$$\begin{aligned} C_L &= C_{L_w} + \eta \frac{S_t}{S} \Delta C_{L_t} \\ &= C_{L_0} + C_{L_\alpha} \alpha + C_{L_Q} Q + \Delta C_L \end{aligned} \quad (\text{A.21})$$

$$\begin{aligned} C_m &= C_{m_0} + (h - h_0) C_{L_w} - V_H \eta \Delta C_{L_t} \\ &= C_{m_\alpha} \alpha + C_{m_Q} Q + \Delta C_m \end{aligned} \quad (\text{A.22})$$

with,

$$\Delta C_L = C_{L_{\delta_E}} \delta_E \quad (\text{A.23})$$

$$\Delta C_m = C_{m_{\delta_E}} \delta_E \quad (\text{A.24})$$

The variables  $V_H$  and  $\eta$  describe the horizontal tail volume ratio and the tail efficiency respectively. The horizontal tail volume ratio is an important geometric parameter which is a measure of the aerodynamic effectiveness of the tailplane as a stabilising device. Typical values fall within the range  $0.5 \leq V_H \leq 1.3$  and is given by,

$$V_H = \frac{\ell_t S_t}{\bar{c} S} \quad (\text{A.25})$$

where  $\ell_t$  and  $S_t$  are the tail moment arm and gross area of the tailplane respectively. The tail efficiency depends on the location of the tailplane and is described by the ratio between the dynamic pressures at the tailplane and wing. If the tailplane is located in the wake region of the wing or fuselage, it would have a magnitude less than unity. Typical values fall within the range  $0.8 \leq \eta \leq 1.2$  and is given by,

$$\eta = \frac{\frac{1}{2}\rho V_t^2}{\frac{1}{2}\rho V_w^2} \quad (\text{A.26})$$

Therefore, when the elevator is deflected from its current trim angle, it causes the  $C_m$ - $\alpha$  and  $C_L$ - $\alpha$  curves to shift, resulting in a shift in the equilibrium flight condition [29]. The magnitude of this shift is characterised by the aerodynamic derivatives  $C_{L\delta_E}$  and  $C_{m\delta_E}$  as described by Equations (A.23) and (A.24). This is graphically presented in Figure A.5, where the sign convention specified in Chapter 3 are assumed.

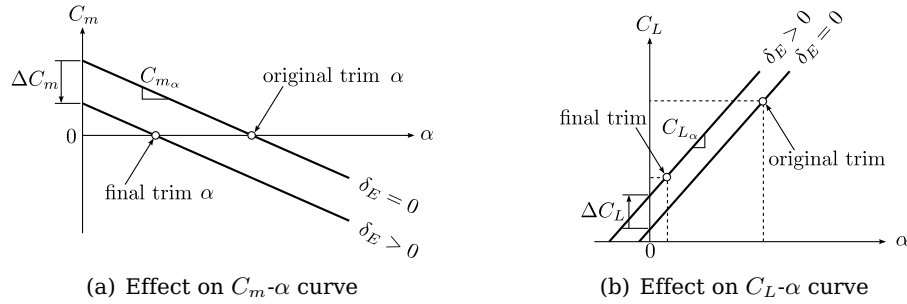


**Figure A.5:** Effect of elevator deflection angle on  $C_m$ - $\alpha$  and  $C_L$ - $\alpha$  curves

The aerodynamic derivative  $C_{m\delta_E}$  is referred to as *the elevator control power*. The larger the value of  $C_{m\delta_E}$ , the more effective the elevator is in creating a pitching moment. Assuming that this change in lift is equal to the change in lift force at the tail, the derivatives in Equations (A.23) and (A.24) can be related to the aerodynamic and geometric characteristics of the tailplane as follows,

$$\Delta C_L = \eta \frac{S_t}{S} \Delta C_{L_t} = \eta \frac{S_t}{S} \frac{dC_{L_t}}{d\delta_E} \delta_E \quad (\text{A.27})$$

$$\Delta C_m = -V_H \eta \Delta C_{L_t} = -V_H \eta \frac{dC_{L_t}}{d\delta_E} \delta_E \quad (\text{A.28})$$

where *the elevator effectiveness* (also known as the lift effectiveness of a control surface) is denoted by  $\frac{dC_{L_t}}{d\delta_E}$ , which is proportional to the size of the control surface and can be estimated from the following equation,

$$\frac{dC_{L_t}}{d\delta_E} = \frac{dC_{L_t}}{d\alpha_t} \frac{d\alpha_t}{d\delta_E} \quad (\text{A.29})$$

The parameter  $\frac{d\alpha_t}{d\delta_E}$  is referred to as *the angle of attack effectiveness* and is an important parameter which describes the change in angle of attack due to elevator deflection at constant lift coefficient [5]. As long as the angle of attack is less than the critical angle, the following holds,

$$\frac{d\alpha_t}{d\delta_E} = \alpha_{\delta_E} = \frac{C_{L\delta_E}}{C_{L\alpha}} \tag{A.30}$$

For a control surface planform with low sweep angles, the following expression is a good approximation for  $\alpha_{\delta_E}$ ,

$$\alpha_{\delta_E} = \frac{1}{S_t} \int_{-b/2}^{b/2} \alpha_{\delta_E}(y) c(y) dy \tag{A.31}$$

The relationship between  $\alpha_{\delta_E}$  and the control surface chord ratio  $\frac{c_f}{c}$ , is presented in Figure A.6 along with a graphical description of the aerial vehicle's control surface.

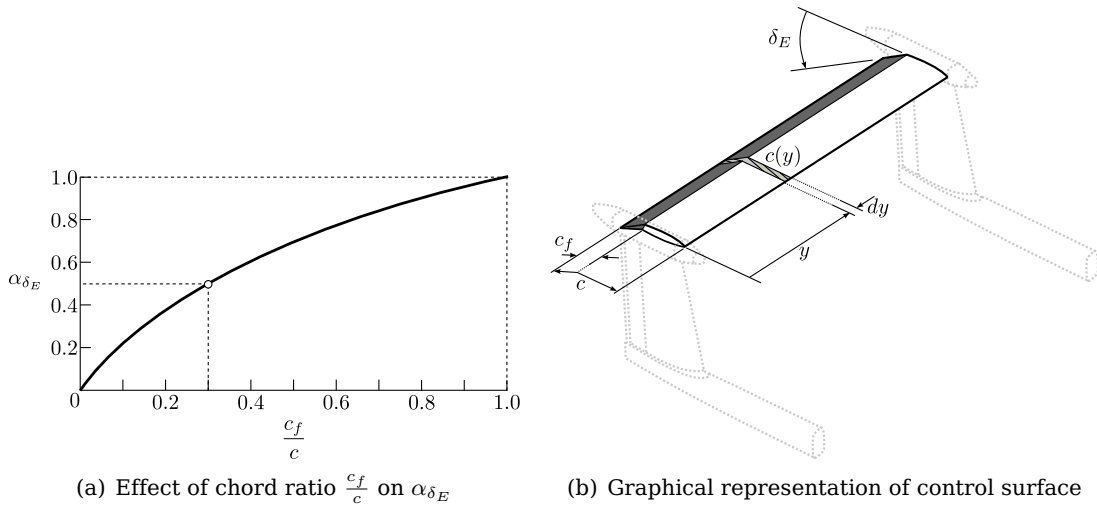


**Figure A.6:** Control surface effectiveness parameter

Notice that a control surface with a 30% chord, has 50% efficiency of an all moving planform in controlling the angle of attack. This is the reason why hinged control surfaces are so widely used, thus very high per unit chord length efficiency.

Consider the transfer from elevator command to angle of attack response for the airframe used during this research. The bode plot analysis at trimmed flight yields the results in Figure A.7 which indicates a control bandwidth of 4.32 rad/s. Since typical human pilots control bandwidth range up to 4.0 rad/s, a pilot will have good control over angle of attack with the elevator.

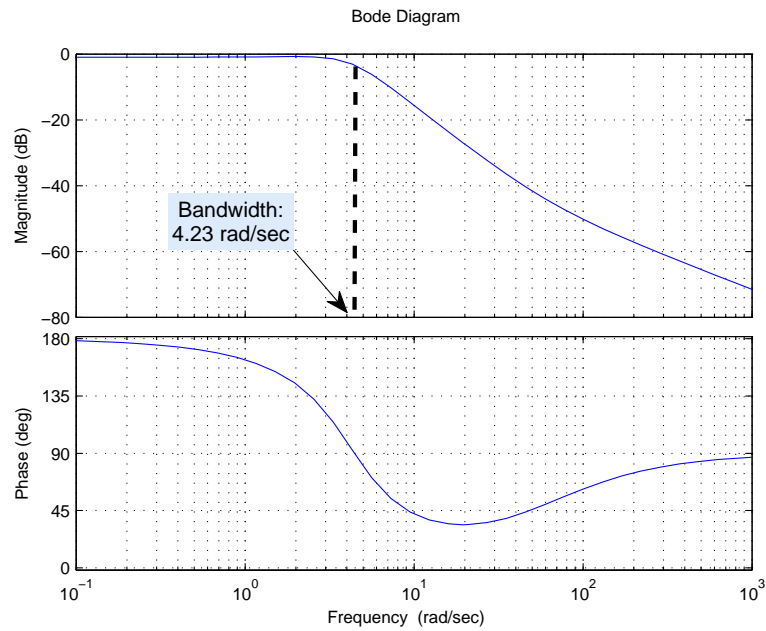


**Figure A.7:** Angle of attack to elevator open loop bode plot



# Appendix B

## Aircraft Data

The geometric, inertial, propulsion and aerodynamic parameters for the modular unmanned aerial vehicle used during this research project is provided in this appendix.

### B.1 Geometric, Inertial and Propulsion Properties

These parameters are the following,

#### Geometric:

|                 |                        |                     |
|-----------------|------------------------|---------------------|
| $\bar{c}$ :     | Mean aerodynamic chord | 0.36 m              |
| $b$ :           | Wing span              | 4.0 m               |
| $S$ :           | Wing surface area      | 1.44 m <sup>2</sup> |
| $\mathcal{R}$ : | Aspect ratio           | 11.11               |
| $e$ :           | Wing efficiency factor | 0.85                |

#### Inertial:

|                  |                              |   |
|------------------|------------------------------|---|
| $m$ :            | mass                         | 26 kg   |
| $\mathbf{I}_B$ : | Principal moments of inertia | $\begin{bmatrix} 16.534 & 0 & 0 \\ 0 & 11.583 & 0 \\ 0 & 0 & 13.671 \end{bmatrix} \text{kgm}^3$ |

#### Propulsion:

|             |                       |        |
|-------------|-----------------------|--------|
| $T_{max}$ : | Maximum engine thrust | 150 N  |
| $\tau_T$ :  | Engine lag            | 0.40 s |

## B.2 Trim Condition

The following trim flight condition were chosen for control system design purposes,

### Trimmed Flight:

|             |                             |                          |
|-------------|-----------------------------|--------------------------|
| $\bar{V}$ : | The trim velocity magnitude | 22 m/s                   |
| $\rho$ :    | The trim air density        | 1.0588 kg/m <sup>3</sup> |

## B.3 Aerodynamic Modelling

One of the most difficult tasks is to quantify the aerodynamic behaviour of an aircraft since the flow conditions around the airframe are generally complex. In order to mathematically describe the aerodynamic forces and moments acting on the airframe, a compromise needs to be made between accuracy and analytical suitability. The result leads to simpler approximate aerodynamic models which lend themselves easily to linearised equation of motion and describe the aerodynamic properties of the airframe with an acceptable degree of accuracy. The consequence of this compromise is that the aerodynamic models are only valid for a small range of operating conditions and so too the solution to the linearised equations of motion. By constraining the flight envelope of the aircraft to this linearised operating region, the aerodynamic model will remain valid which allows for the design of elegant control systems.

The concept of aerodynamic derivatives are a means of describing the aerodynamic properties of the airframe. These derivatives include aerodynamic stability and control derivatives. Various methods exist for determining the aerodynamic derivatives of an airframe. The accuracy of the derivatives are subject to the quality of the source material and the method of evaluation, but ultimately the derivative values can at best be considered as estimates regardless of the applied method.

In [7] the aerodynamic derivatives used to mathematically model the aerodynamic behaviour of the airframe are referred to as *quasi-static* quantities which are based on, and derived from, static aerodynamic conditions but which are used in the description of dynamically varying aerodynamic conditions. This describes the procedure of a small perturbation model about a certain equilibrium condition and will be assumed throughout this research. It should be noted that this limits the aerodynamic model to perturbation motion (internal or external) small in magnitude and duration about the nominal trim condition.

### B.3.1 Analysis with AVL

*Athena Vortex Lattice*, was originally developed by Harold Youngren and updated and modified since by both Harold Youngren and Mark Drela. AVL has a large number of features aimed at rapid aircraft configuration analysis. A few of these features include calculating aerodynamic components of lifting surfaces and bodies, simulation with control surface deflections, trim calculation of operating variables and calculation of the stability and control derivatives of the aircraft. The latter feature being very useful in deriving the mathematical model of the aerial vehicle. AVL is best suited for aerodynamic configurations which consist mainly of thin lifting surfaces at small angles of attack and sideslip.

AVL also provides the capability to model slender bodies such as fuselages. The purpose of this analysis is to calculate the stability and control derivatives. These derivatives define the link between the aircraft dynamics and the airframe aerodynamics, thus giving insight into the dominant aerodynamic properties driving the airframe dynamics. AVL calculates the stability and control derivatives about a certain trim flight condition. These derivative values will be substituted into the linear aircraft model that will be used as the plant for the autopilot control system. The derived linear aerodynamic model is therefore limited to small perturbation motion about this flight condition.

Consider the graphical output in Figure B.1, generated with AVL of the aerial vehicle used during this project.

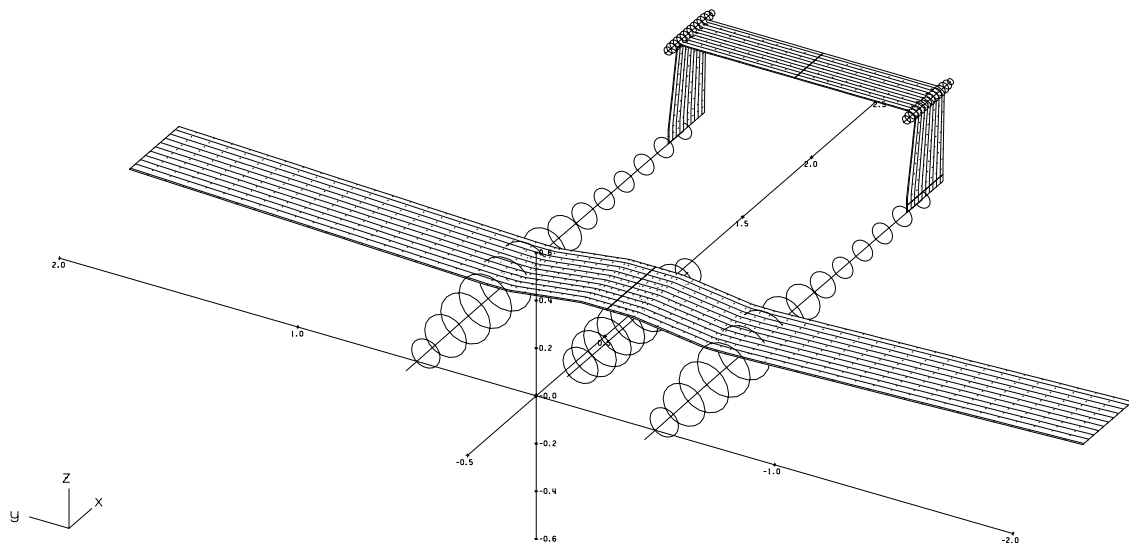


**Figure B.1:** The aerofoil and fuselage assembly of the aerial vehicle as designed in AVL

Assuming the same trim flight condition as adopted throughout this project, these estimated dimensionless aerodynamic derivative values are presented in Table B.1

and Table B.2.

| Longitudinal Stability and Control Derivatives |              |                     |             |
|--|--------------|---------------------|-------------|
| Stability Derivatives                          |              | Control Derivatives |             |
| $C_{L\alpha}$                                  | = 46.032292  | $C_{L\delta_E}$     | = 0.007172  |
| $C_{LQ}$                                       | = 8.628332   | $C_{m\delta_E}$     | = -0.024727 |
| $C_{m\alpha}$                                  | = -0.551039  |                     |             |
| $C_{mQ}$                                       | = -18.672926 |                     |             |

**Table B.1:** The non-dimensional longitudinal stability and control derivatives

| Lateral Stability and Control Derivatives |             |                     |             |
|---|-------------|---------------------|-------------|
| Stability Derivatives                     |             | Control Derivatives |             |
| $C_{Y\beta}$                              | = -0.416437 | $C_{Y\delta_R}$     | = 0.003727  |
| $C_{Y_P}$                                 | = 0.064577  | $C_{Y\delta_A}$     | = -0.000340 |
| $C_{Y_R}$                                 | = 0.215613  | $C_{l\delta_R}$     | = 0.000097  |
| $C_{l\beta}$                              | = -0.079487 | $C_{l\delta_A}$     | = -0.005699 |
| $C_{l_P}$                                 | = -0.634106 | $C_{n\delta_R}$     | = -0.001236 |
| $C_{l_R}$                                 | = 0.185521  | $C_{n\delta_A}$     | = 0.000147  |
| $C_{n\beta}$                              | = 0.081492  |                     |             |
| $C_{n_P}$                                 | = -0.067172 |                     |             |
| $C_{n_R}$                                 | = -0.088430 |                     |             |

**Table B.2:** The non-dimensional lateral stability and control derivatives

The longitudinal derivatives due to acceleration perturbations are neglected from the estimation. These include  $C_{L\dot{\alpha}}$ ,  $C_{m\dot{\alpha}}$  which characterises the *downwash lag* induced by the exhaust airflow from the wing flowing over the tailplane. In performance aircraft these derivatives could have a significant effect of the aerodynamics of the airframe. However, due to the conservative design of the airframe used during this research project and the location of the horizontal stabiliser, these effects will only become apparent at very high angles of attack and therefore are ignored. An alternative method of obtaining accurate estimates of the stability and control derivatives is to conduct a wind tunnel test.

## B.4 Numeric Aerodynamic Investigation

This analysis attempts to numerically identify the critical angle of attack at the maximum lift coefficient as well as the maximum angle of attack that defines the limit of the linear lift region, by utilising aerodynamic software. The software applications that were used for this analysis are freeware, since that is what was available. These

applications are *XFOIL v6.96* and *XFLR5 v4.16* which will be briefly presented in this section. Analysis with these applications will result in a rough estimate of the angle of attack limits for this aerial vehicle. A more thorough approach would be to utilise full CFD (Computational Fluid Dynamics) software packages to gain a more accurate of the aircraft's lift curve, but this would also just be an computational estimate. For the purpose of this research project, that level of accuracy is not required and the analysis with the freeware applications will be sufficient. Note however, that the angle of attack values determined from this analysis, do not limit the development of the algorithms in this project. The algorithm will allow for any maximum angle of attack to be defined by the designer.

#### B.4.1 XFOIL

An interactive program for the design and analysis of subsonic isolated aerofoils. XFOIL was developed by Mark Drela<sup>1</sup> and Harold Youngren<sup>2</sup> at MIT. It consists of a collection of menu-driven routines which perform various useful functions. These functions include viscous (and inviscid) analysis of an existing aerofoil allowing lift and drag predictions just beyond  $C_{L_{max}}$ , aerofoil design and redesign, drag polar calculation with fixed or varying Reynolds and/or Mach numbers and also plotting of geometry, pressure distributions, and polars. It simulates with good accuracy the air-flow around a two dimensional (2D) aerofoil section travelling through the air on its own. This is a purely ideal case which neglects the wing and its associated planform induced effects such as induced drag. This analysis is useful for comparing different types of aerofoils but lacks if one wishes to analyse the performance of the wing or a complete aircraft.

The following analysis was conducted on a aerofoil section of the aerial vehicle's wing (main lift generating surface). The profile of this aerofoil section has a reference code of *SD7062*. This aerofoil profile is preferred for low speed and low Reynolds number flight due to its lift and drag performance in these conditions. For a trimmed air velocity and air density of 22 m/s and 1.0588 kg/m<sup>3</sup> respectively, the associated Reynolds number and Mach number are calculated to be 481078.7827 and 0.06577 respectively. Applying a virtual wind tunnel analysis to this aerofoil section at this trimmed flight condition and analysing the effect of viscous flow around this aerofoil section by taking the boundary layers and wake into account, yields the results displayed in Figure B.2. The resulting pressure distribution on the upper and lower surface of the aerofoil is shown in Figure B.2(a) at this trim angle of attack, where the solid and dashed lines indicates the pressure distribution as a result of the viscous flow and inviscid flow respectively. This difference is due to the modification of the effective aerofoil

---

<sup>1</sup>Mark Drela, MIT Aero & Astro

<sup>2</sup>Harold Youngren, Aerocraft, Inc.

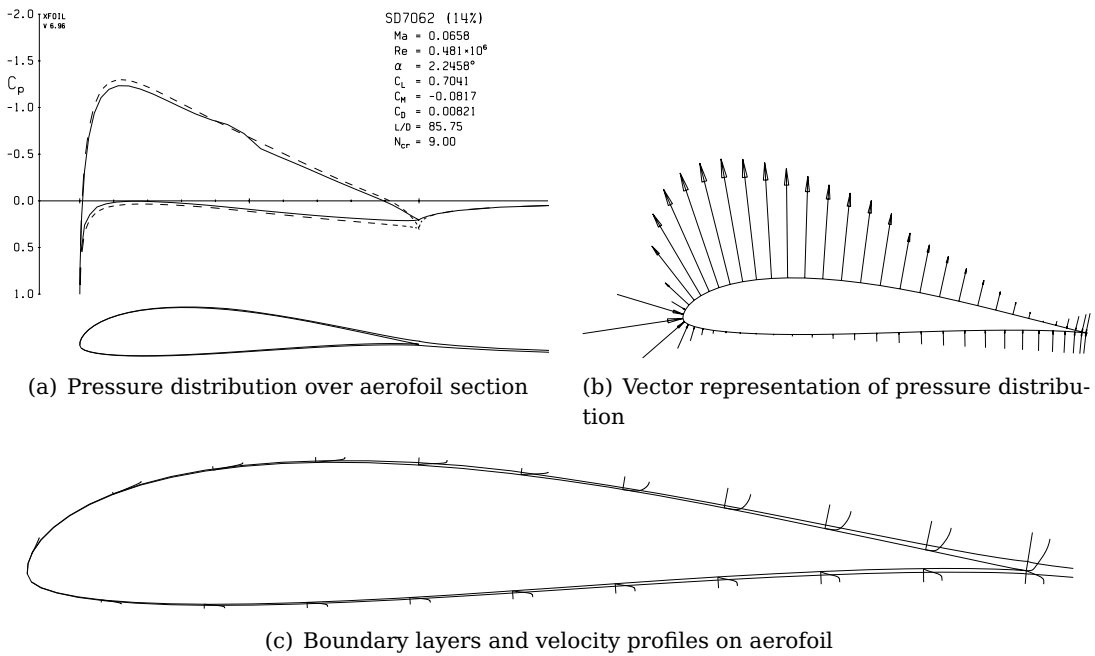


**Figure B.2:** Aerofoil section of main wing of aerial vehicle

shape by the boundary layer. The vector representation of the pressure distribution is displayed in Figure B.2(b). The boundary layer and velocity profiles on the aerofoil at this flight condition is displayed in Figure B.2(c).

Conducting a polar analysis by sweeping the aerofoil section through a range of angle of attack values in viscous airflow and accumulating the results will yield the lift and drag polars as a function of the angle of attack. Simulating this in XFOIL yields the results presented in Figure B.3 displaying the nonlinear nature of the lift and drag produced.

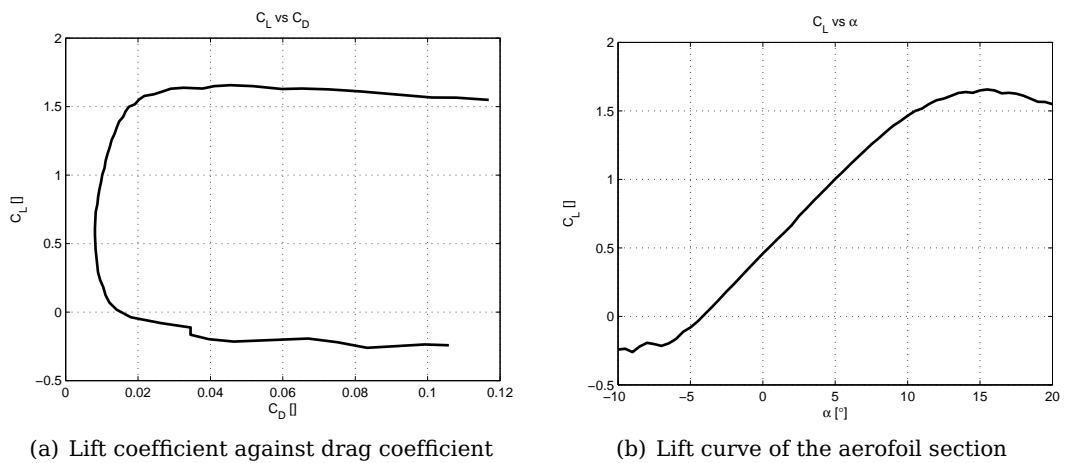


**Figure B.3:** Polar plots for lift and drag coefficients simulated with XFOIL

Notice that the angle of attack value of  $10^\circ$  lies at the edge of the linear lift region. Exceeding this angle results in a nonlinear relationship between lift and angle of attack. The drag curve is the superposition of the friction drag ( $C_{D_f}$ ) and the pressure drag ( $C_{D_p}$ ) as a result of the skin friction and the surface pressure on the aerofoil section respectively. With the friction drag being dominant at low angle of attack values and the pressure drag dominant at large angle of attack values.

### B.4.2 XFLR5

A program developed by André Deperrois, expands on the analysis of XFOIL by allowing the design and analysis of a complete wing/aircraft assembly by incorporating the well known *vortex lattice method* (VLM). The classical VLM analysis assumes a purely inviscid flow around the lifting bodies and is therefore a bit unrealistic for the Reynolds numbers used by model aircraft, XFLR5 postulates that the viscous and inviscid contributions to aerodynamic forces are linearly independent, so that an inviscid VLM output may be complemented by a viscous XFOIL analysis to get a more realistic mathematical model. Since this independence hypothesis is not supported by a theoretical model, the analysis results needs to be verified and considered preliminary and experimental.

XFLR5 allows the wing to be analysed using a nonlinear version of the *Lifting Line Theory* (LLT) by taking into account the viscous effects in relation to  $C_L$  as a function of  $\alpha$ . The nonlinear lift behaviour is interpolated onto pre-generated XFOIL polars curves and then solved using an iteration loop. This numerical method also comes with limitations and will lack in accuracy when wings with low aspect ratio and large sweep angles are analysed. This however poses no problem to the wing analysed in this project, yet the results still needs to be considered experimental. Importing the aerofoil profile of the aerial vehicles main wing into XFLR5 and designing the wing of the UAV yields the geometric representation of the wing displayed in Figure B.4.

Analysing the entire wing structure with this nonlinear LLT at the flight conditions (Reynolds number and Mach number) specified earlier, yields the lift and drag characteristics presented in Figure B.5.

Since the wing planform is rectangular, the lift polar looks very similar to that simulated with XFOIL (where the aspect ratio was assumed to be infinite), displaying desirable gradual stall characteristics. However, due to the wing's finite nature, the slope of this curve will be different. The positive angle of attack value at the edge of the linear region however remains unchanged. The negative angle of attack limit seems to lie close to  $-10^\circ$ . Since the lift curve becomes irregular at the negative end, this angle of attack limit is merely an approximation and a more conservative value needs to be chosen as the negative limit of the linear lift region.

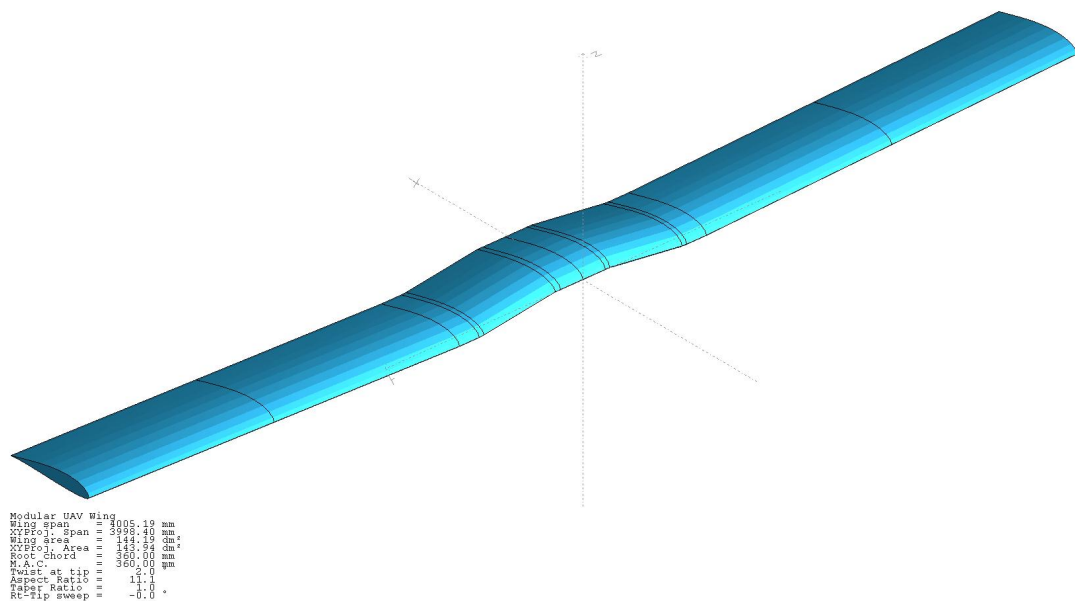


**Figure B.4:** The main wing of the aerial vehicle as designed in XFLR5

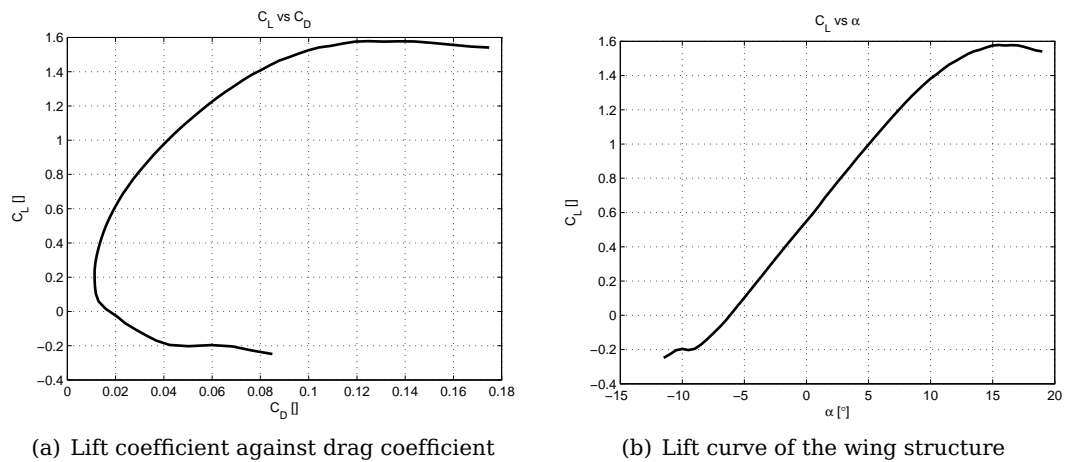


**Figure B.5:** Polar plots for lift and drag coefficients simulated with XFLR5 on wing structure

XFLR5 only allows the linear *vortex lattice method* (VLM) to be used when analysing the entire aircraft assembly. This method does not account for viscous effects and hence for stall at high angles of attack. At the intended air velocities for the aerial vehicle, the viscous drag is not negligible compared to the induced drag. XFLR5 thus attempts to estimate the viscous drag by interpolation of pre-generated XFOIL polar curves. This assumes implicitly that the aerofoil's behaviour on a finite wing is not very different from an infinite XFOIL wing. This however only significantly influences the estimation of the viscous drag, leading to arguably optimistic results in the drag calculation. The lift curve however should be quite similar in the linear region, but the method is expected to breakdown once the lift curve become nonlinear. Consider the results presented in Figure B.7 produced by analysing the aircraft assembly presented



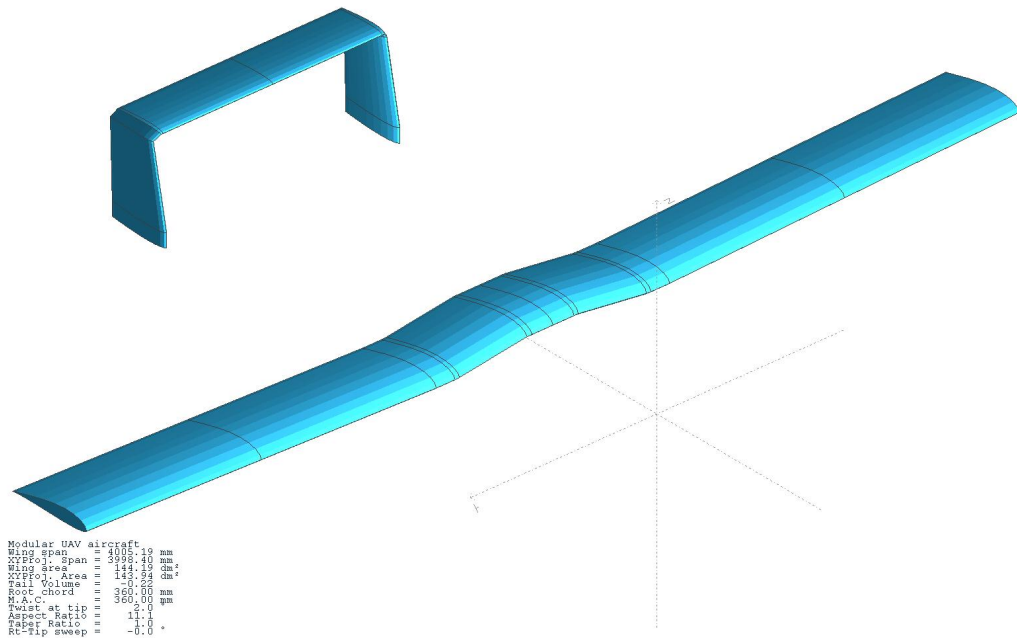


**Figure B.6:** The main wing, tailplane and fin assembly of the aerial vehicle as designed in XFLR5

in Figure B.6 using the VLM.

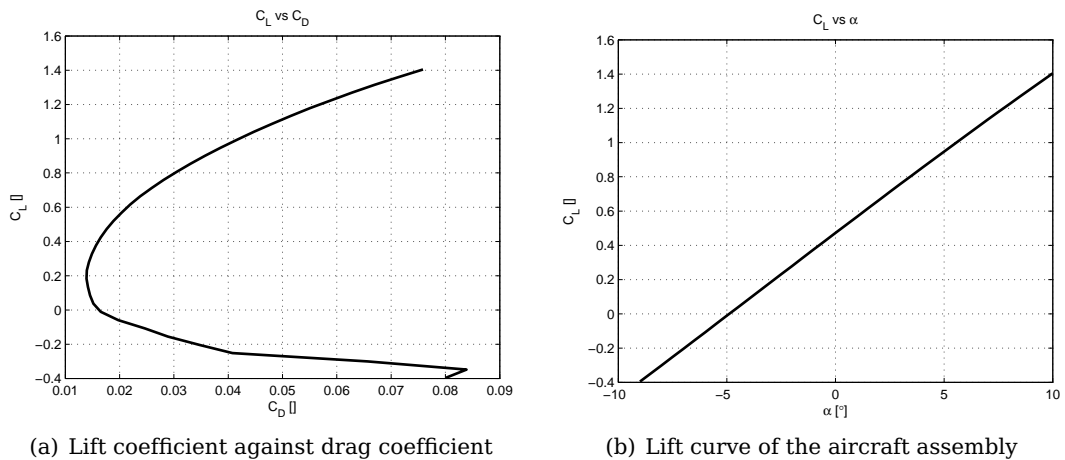


**Figure B.7:** Polar plots for lift and drag coefficients simulated with XFLR5 on aircraft assembly

As expected the method fails to interpolate the viscous effects of the pre-generated XFOIL polars onto the polar calculated by the vortex lattice method at both the positive and negative limits of the lift curve. This is as a result of the lift curve becoming nonlinear at these angles of attack. This analysis thus concludes the angle of attack range of linear lift and yields approximate values for the positive and negative angle of attack limits of this region.

## B.5 Typical AoA Sensors for Practical Implementation

It is imperative to measure the angle of attack directly during flight for the detection algorithm to make accurate forecasts of an approaching stall. Angle of attack sensors are usually mounted ahead of the aircraft, on the nose of the fuselage or leading edge of the wingtip, since it is important that the sensor makes first contact with the oncoming airflow. In fact the sensors could be mounted anywhere on the aircraft body, as long as the proper care is taken to ensure that the sensor do not measure airflow disrupted by the aircraft itself. This disrupted airflow provide input errors to the sensors. The effect of compressibility also becomes significant above Mach 0.3 which affects the static pressure around the aircraft. This makes the location of the sensors vital to reduce errors. At higher speeds, shock-waves are formed which also adds to the disturbances [30].

The reading made by the angle of attack sensor is the measured local airflow angle and not the true angle of attack of the free-stream airflow. This difference is referred to as the *position error* and is influenced by the Mach number and lift produced by the aircraft. Sensors mounted near the leading edge of the wing is greatly affected by upwash, similarly sensors mounted at the wing-tips are affected by upwash as well as sidewash across the wing's surface. Typically air flow sensors are mounted on airdata booms extending forward (usually located at the nose of the fuselage, which provide the smallest and most constant position error throughout the subsonic, transonic and supersonic speed ranges), therefore outside the disturb airflow region.

Through in flight calibration techniques (to account for any additional errors introduced by accelerated manoeuvres), the position error can be determined. Errors involving the sensor itself are generally determined through wind-tunnel tests [31].

There are three main sensor types commonly used to measure the angle of attack (sensors could also be mounted to measure the angle of sideslip) on aircraft namely, fixed differential pressure probes, pivoted vane sensors.

### B.5.1 Fixed Differential Pressure Probes

This type of sensor consists of a simple tube (usually with a hemispherical, conical or pyramidal shaped head) with two holes located on either side of the longitudinal axis at a known angle relative to each other. The angle of attack is then calculated from the difference between the two static pressures measured at the respective holes. For hemispherical and conical shaped nose heads, the greatest sensitivity in measurement is achieved when the two holes are oriented orthogonal with respect to each other as presented in Figure B.8.

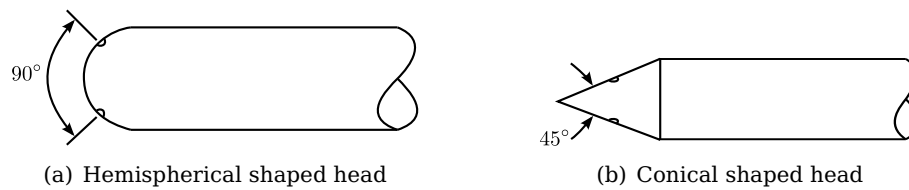


**Figure B.8:** Typical pressure difference based angle of attack sensor

This sensor can be made by modifying a standard pitot-static tube, by simply adding another hole opposite the existing hole. The magnitude of the angle of attack measured by this sensor depends on the shape of the nose of the tube, the angular arrangement of the holes and on the Mach and Reynolds number. Therefore it is important to calibrate each particular sensor in a wind tunnel. The only drawback to this perfectly adequate sensor design, is that two separate transducer devices is required to measure the static-pressure at each hole individually. An alternative would be to implement a pressure ratio device, which will allow for only one transducer device.

### B.5.2 Pivoted Vane Sensors

Pivoted vanes are small mass balanced (to remove biases and improve precision during dynamic manoeuvres) tubes with fins mounted at the rear ends to align the vane with the oncoming airflow in a *weather cock* fashion, thus directly measuring the angle of the airflow. Pivoted vanes are connected to a potentiometer or other angle-measuring transducer devices. As with the pressure difference sensor, pivoted vanes are allowed to be mounted on a variety of locations on the aircraft, typically on the shaft of a airdata boom. They are mounted orthogonal with respect to each other, with the vertical vane being tangent to the aircraft's plane of symmetry. With this configuration, the vertical vane measures the angle of sideslip, while the horizontal vane measures the angle of attack as presented in Figure B.9.

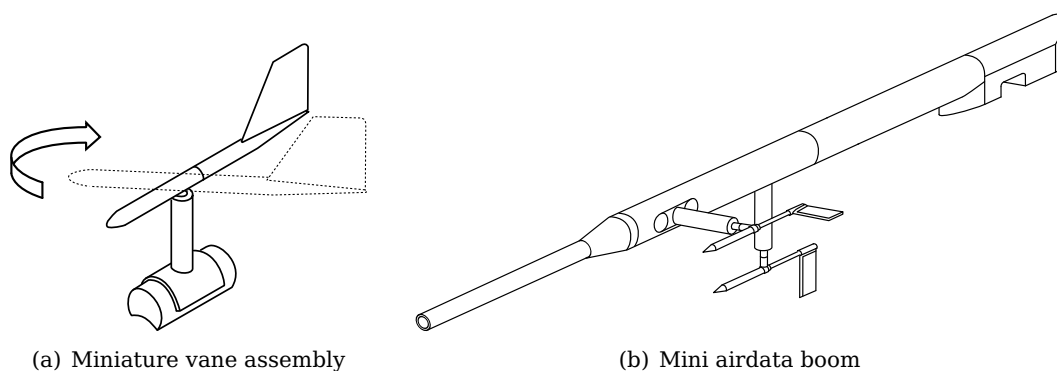


**Figure B.9:** Typical vane type angle of attack and angle of sideslip sensors

Pivoted vanes tend to be more sensitive especially at lower airspeeds. Slight errors in the measurement occur as a result of the location of the vane and the quality of the manufactured vane itself. The bending of the airdata boom shaft and the airflow distorted by the upwash against the shaft, contribute to the error. The vane's proximity to the shaft can reduce the upwash effect by mounting the vane at least two boom diameters from the boom axis. The flight condition also effects the measurement due to the deformations caused by wing loading and pressures exerted on the vane during manoeuvring flight. However, upwash and manufactured imperfection errors can be compensated for by calibration in wind-tunnel tests, while various additional methods exist to correct for the bending of the boom itself.

### B.5.3 Null-Seeking Differential Pressure Probes

These sensors are similar to the fixed differential pressure probes, except that the probe has two orifices spaced at equal angles to the tube axis and it continuously attempts to align itself with the oncoming airflow by rotating using a servo, as presented in Figure B.10. It is guided by the differential pressure measurement and rotates to reduce the measurement to zero. The angle at which the probe rotates to measures the angle of attack relative to the aircraft datum.



(a) Conical shaped probe



(b) Cylindrical shaped probe

**Figure B.10:** Typical null-seeking differential pressure probe type angle of attack sensors

The advantage of this rotating probe, as compared to the fixed probe, is that the measurement is not affected by impact pressure from the oncoming airflow, Mach and Reynolds number. Assuming the servo response is sufficiently rapid, this probe will be comparatively sensitive to the fixed probe.